BRNO UNIVERSITY OF TECHNOLOGY

Faculty of Chemistry

DOCTORAL THESIS

Brno, 2016 Ing. Tomáš Solný

BRNO UNIVERSITY OF TECHNOLOGY
VYSOKÉ UČENÍ TECHNICKÉ V BRNĚ

FACULTY OF CHEMISTRY
FAKULTA CHEMICKÁ

INSTITUTE OF MATERIALS SCIENCE
ÚSTAV CHEMIE MATERIÁLŮ

SYNTHESIS AND PHOTOCATALYTIC APPLICATIONS OF TITANIUM DIOXIDE
PŘÍPRAVA A APLIKACE FOTOKATALYTICKY AKTIVNÍHO OXIDU TITANIČITÉHO

DOCTORAL THESIS
DIZERTAČNÍ PRÁCE

AUTHOR — **Ing. Tomáš Solný**
AUTOR PRÁCE

SUPERVISOR — **doc. Ing. Petr Ptáček, Ph.D.**
ŠKOLITEL

BRNO 2016

ABSTRACT

Hydrolysis conditions for different Ti-alkoxides were examined considering the impact of water to alkoxide ratio and temperature. The prepared hydrolysates and sintered TiO_2 nanoparticles were examined with XRD, DTA – TGA, SEM – EDS, BET and PCCS analysis in order to identify the impact of hydrolysis on properties of prepared anatase particles. Magnetite nanoparticles were synthetized by easy one step precipitation method from Mohr´s salt solution and their crystallinity, size and surface properties were examined investigating the influence of temperature and coating by polycarboxylate ether superplasticizer. For immobilization of TiO_2 on surfaces of magnetite combined method using the selected nanoparticles of TiO_2 and Ti-alkoxides hydrolysis is performed in order to obtain photocatalytically active core–shell powder catalysator with enhanced adsorptive properties. Also the investigation on the applications of TiO_2 on surfaces of Mn-Zn ferrite is done with studying the surface treatment by CVD deposition of C and Au layer. Photocatalytic activity of selected prepared photocatalysators is evaluated upon decomposition of methylene blue and isopropanolic and ethanolic vapors for Mn-Zn ferrite in experimental chemical reactor with magnetically holded powdered photocatalysator beds.

KEYWORDS:

Titanium oxide, anatase, photocatalytic activity, core-shell powder photocatalysator, magnetite, Mn-Zn ferrite, Ti-alkoxides, hydrolysis, sol-gel, nanoparticles.

ABSTRAKT

V práci je zkoumán vliv podmínek na průběh hydrolýzy alkoxidů titanu a vlastností připravovaných nanočástic oxidu titaničitého s důrazem na teplotu a množství vody přítomné v systému. Připravované hydrolyzáty alkoxidů titanu a nanočástice oxidu titaničitého připravené z hydrolyzátů jsou studovány metodami XRD, DTA – TGA, SEM – EDS, BET a PCCS. Nanočástice magnetitu byly syntetizovány pomocí precipitační reakce z roztoku Mohrovy soli a jejich krystalová struktura, velikost a povrchové vlastnosti byly sledovány s vyhodnocením vlivu teploty a při modifikaci povrchu polykarboxyletherovým superplastifikátorem. Pro upevnění TiO_2 na povrch magnetitu byla použita kombinovaná metoda aplikace vybraných nanočástic TiO_2 s hydrolýzou TiO_2 pomocí alkoxidů titanu za účelem přípravy fotokatalyticky aktivního core-shell práškového katalyzátoru s vylepšenými vlastnostmi adsorpce na povrchu. Studovány byly možnosti aplikace TiO_2 na povrch Mn-Zn feritu, kdy byl studován vliv depozice tenkých vrstev C a Au na morfologii povrchu. Fotokatalytická aktivita vybraných připravených materiálů byla studována pomocí dekompozice methylenové modři v roztoku a par isopropanolu a ethanolu rozkládaných pomocí Mn-Zn feritu v experimentálním chemickém reaktoru s magnetickým polem stabilizovaným ložem nosiče katalyzátoru.

KLÍČOVÁ SLOVA:

TiO_2, anatas, fotokatalytická aktivita, core-shell práškové fotokatalyzátory, magnetit, Mn-Zn ferrity, alkoxidy titanu, nanočástice

SOLNÝ, T. Synthesis and photocatalytic applications of titanium dioxide. Brno: Brno University of Technology, Faculty of Chemistry, 2016, 133 pages. Supervisor of Thesis: doc. Ing. Petr Ptáček, Ph.D.

DECLARATION

I declare, that the doctoral thesis has been elaborated by myself and all the quotations from the used literature sources are accurate and complete. The content of the doctoral thesis is the property of the Faculty of Chemistry, Brno University of Technology and all commercial uses are allowed only if approved by the supervisor and the dean of the Faculty of Chemistry, BUT.

.....

Student´s signature

ACKNOWLEDGEMENT

In this place, I would like to sincerely thank to my supervisor Doc. Ing. Petr Ptáček, Ph.D for his helpfull advices and motivation during all my doctoral studies as well as to the supervisor specialist, Ing. Tomáš Opravil, Ph.D, who inspired me in overcoming deals arrised from the studied theme.

Sincere acknowledgement belongs also to Dr. Svava Davíðsdóttir and Prof. Rajan Ambat from Section of Materials and Surface Engineering, Department of Mechanical Engineering, Technical University of Denmark for fruitful cooperation and possibility to elaborate part of the work in their department.

My acknowledgement belongs also to Ing. Eva Bartonickova, Ph.D, Ing. Jiri Masilko, Ph. D, and Ing. Jakub Tkacz, Ph.D, as well as to all colleagues from the laboratories of ceramic materials and inorganic binders which belong to the Centre of Materials Research, Faculty of Chemistry, Brno University of Technology.

This work was financially supported by the project "Materials Research Centre at FCH BUT- Sustainability and Development" REG LO1211, with financial support from National Programme for Sustainability I (Ministry of Education, Youth and Sports)

CONTENTS

1 INTRODUCTION

Titanium dioxide has a wide range of applications. Since its commercial production in the early twentieth century it is used as a pigment in paints, coatings, sunscreeens, ointments and toothpaste.Titanium dioxide is obtained from a variety of ores containing ilmenite, rutile anatase and leucoxene. The first commercial production over the world started in USA, Germany and Norway.

Since the TiO_2 production for the pigments in anatase and rutile form is known for more than 100 years now, the discovery of its photolysis activity, made by Fujishima and co-workers, published in 1969, [1] started research and development of numerous uses of TiO_2 all over the world. Ongoing research nowadays is leading to more and more aplications of TiO_2 properties with emphasizing its photocatalytic activity. The research interest on TiO_2 can be depicted by an exponentional increase in the number of publications during past decades. This is demonstrated in figure 1 considering past four decades of research topics on " Photocatalytic TiO_2 " indexed by Thomas Reuters Web of Science where the logarithmic scale is used on the axis y.

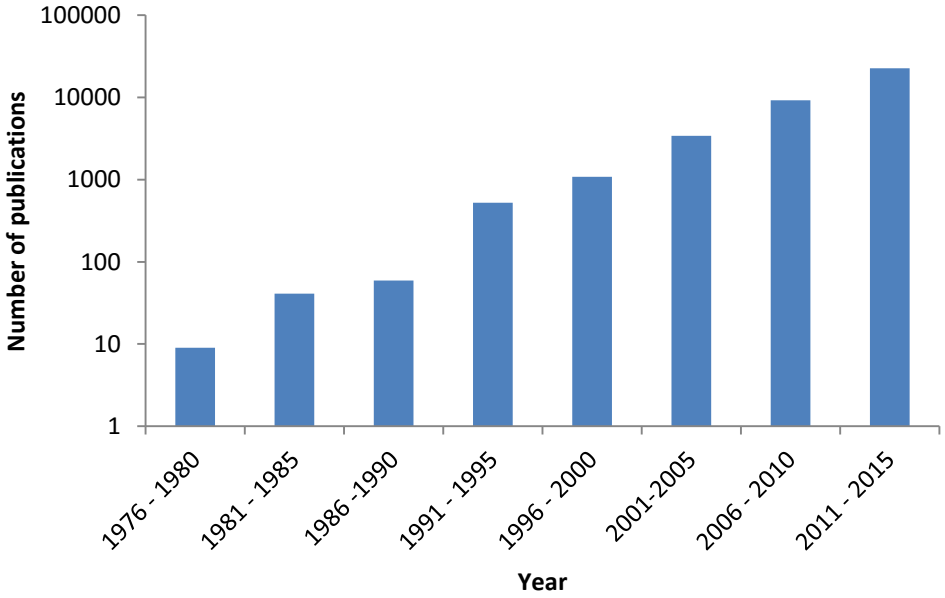

Fig. 1 Number of publications on "Photocatalytic TiO_2" in past four decades on Web of Science

TiO_2 is one of starting materials for further development of sustainable green future technologies among many industrial sectors, and definitely the material mostly used in nanotechnology development and catalysis applications. In the field of nanotechnology, the TiO_2 finds a great deal of applications. This technology is instantly growing and influencing many fields of research and development areas such as biology, chemistry, material science, medicine and physics.

2 AIM OF THE THESIS

Aim of present study is to investigate the methods of preparation of TiO_2 in the photocatalytic active form of anatase and its application in magnetically active powder core-shell photocatalysators and a preparation of powder photocatalysators with evaluation of their photocatalytic activity. The following objectives of work were identified:

- Literature review on preparation of TiO_2 by hydrolysis and its modifications and preparation of inert powdered substrate for photocatalytically active TiO_2.
- Synthesis of TiO_2 in photocatalytical modification of anatase, studying the hydrolysis conditions of used titanium alkoxide mixtures.
- Preparation of inert powder substrates for the TiO_2 deposition processes, characterisation of the prepared materials.
- Deposition of TiO_2 on the surface of the prepared and selected magnetic inert holders.
- Photocatalytic activity studies on the prepared TiO_2 core-shell materials.

3 THEORETICAL PART

3.1 Characteristics of TiO_2

TiO_2 is thermally stable compound, which is inert against acids, bases and insoluble in most solvents. Its most known application since commercial exploitation in beginning of 20th century is its usage as a pigment in industry. The reason for this application is high refractive indice, which result in high reflectivity from the surfaces. Another reason for such applications is also opacifying power and brightness of small TiO_2 particles.TiO_2 naturally occurs in three crystallographic forms: anatase, rutile and brookite.

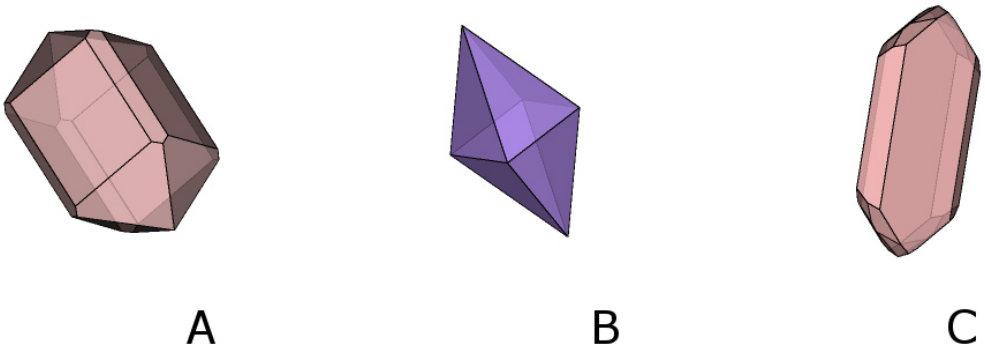

Fig. 1 Crystallographic forms of TiO_2, A – Anatase, B – Rutile and C – Brookite

Brookite has orthorombic crystal structure, anatase and rutile form tetragonal structure. Anatase and brookite are in elevated temperatures exceeding 600°C unstable and undergo transition into the rutile form, which is most stable structure of TiO_2, melting in temperatures above 1 750 °C. Next to these mostly widespread forms, another different forms of TiO_2 were prepared, represented by high pressure forms, such as α-PbO_2-like form (orthorombic) [2], baddeleyite-like form (monoclinic) [3], TiO_2-O (orthorhombic) [4], some high temperature and high pressure forms including cotunnite-like form (orthorhombic) [5] and cubic form [6], and synthetized materials TiO_2 (B) (monoclinic) prepared by hydrolysis of $K_2Ti_4O_9$ [7], hollandite-like form (tetragonal) formed after oxidation of the related potassium titanate bronze [8] and ramsdellite-like form (orthorhombic), prepared by oxidation of the related lithium titanate bronze. [9] Some facts about crystallographic forms of TiO_2 are mentioned in table 1.

Tab. 1 Density, reflective index, space group and band-gap energy (Eg) values of TiO_2

Modification	n_D	Eg (eV)	Space group	ρ [g·cm^{-3}]
Brookite	2.583	3.14	Pbca	4.15
Anatase	2.488	3.3	$I4_1/amd$	3.90
Rutile	2.609	3.1	$P4_2/mnm$	4.25

Most widespread ore with TiO_2 content, used for the preparation of TiO_2 pigments is ilmenite $FeTiO_3$ (trigonal). From this ore, TiO_2 can be obtained by industrialized processes of sulfate bleaching and hydrochloric bleaching.

Since the discovery of photolysis activity of TiO_2 on sunlight, enormous effort have been devoted to the research of TiO_2 materials, leading to many promising applications in areas ranging from photovoltaics, sensors to photocatalysis. From the forms of TiO_2, anatase is performing the best photocatalytic activity due to its higher band gap value.

3.2 Phase diagram of Ti-O

The phase diagram of titanium-oxygen contains many stable phases and variety of structures. Stoichimometric compounds Ti_3O_2(s), α-TiO, low-temperature modification of TiO_x solid solution. Ti_2O_3(s), a high-temperature congruently melting oxide, the incongruently melting oxide Ti_3O_5(s) and stable higher Magnelli phases (Ti_nO_{2n-1}) presented in high concentrations of oxygen where n ≥ 4 and highest n was not found yet. [10]

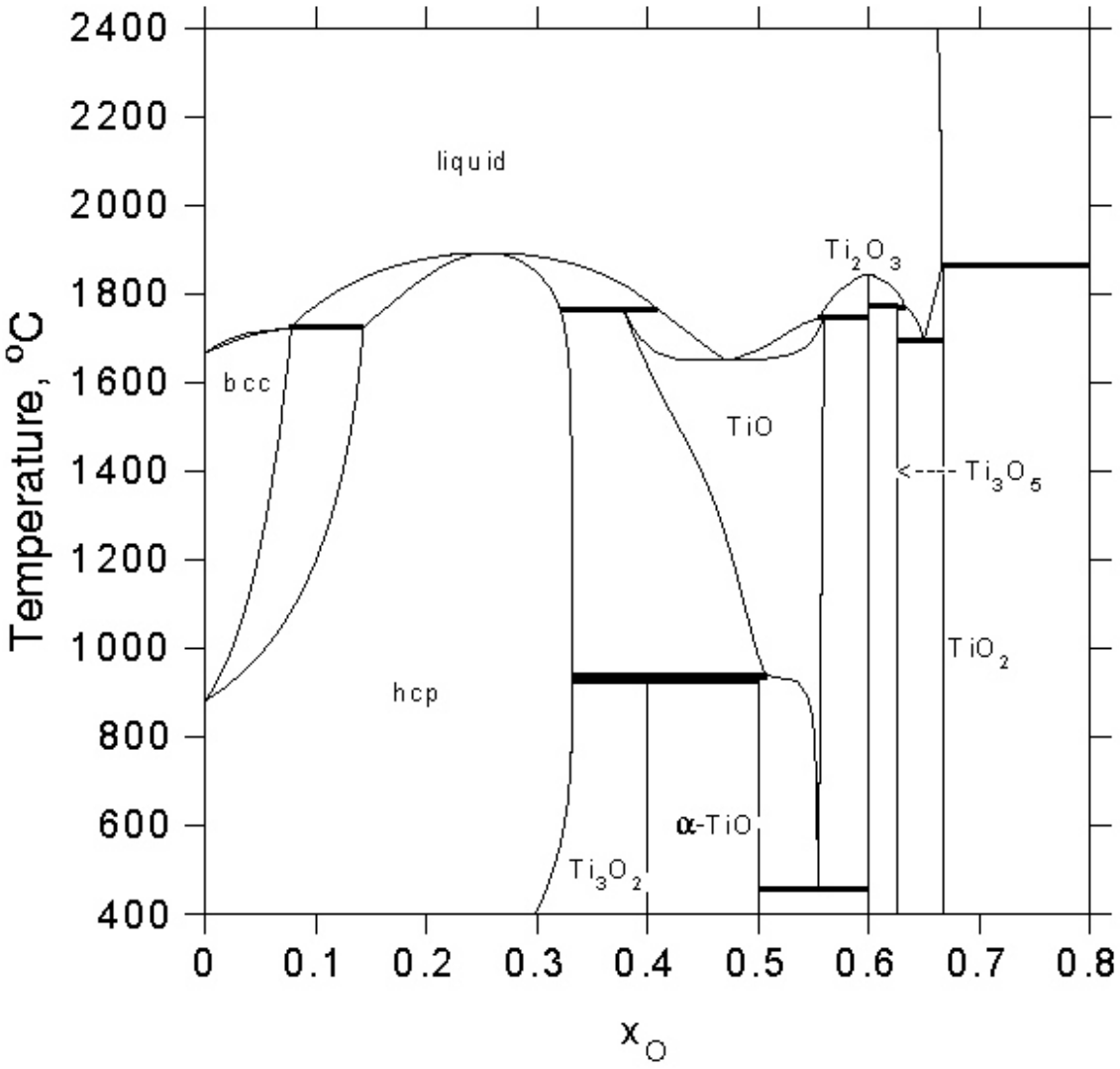

Fig. 2 Phase diagram of Ti-O [11]

According to review made by Waldner and co-workers [10], there are five important condensed mixture phases in Ti-O phase diagram: [10-13]

- Closed packed hexagonal modification (hcp) has high solubility for oxygen up to 30% of atomic content.
- High-temperature body-centered cubic (bcc) modification is only able to solute 8 % atomic oxygen.
- TiO solid solution with a wide homogenity range in high temperatures
- TiO_2 non-stoichiometric rutile.
- Liquid phase, showing transition from purely metallic to highly ionic character.

3.3 Reactions on the surface of TiO_2

3.3.1 Photoelectrochemistry

Photoelectrochemical behavior of solid matter is based on Band theory formulated by Alan Herries Wilson in 1932. [14] In semiconductors band structure of energy states appear instead of having discrete energies as in the case of free atoms. Energy states of electrons in semiconductor can be roughly characterized by a series of energetically closed spaced energy levels associated with covalent bonding of atoms forming the crystallite (valence band) and a series of spatially diffuse, energetically similar levels lying at higher energy associated with conduction in the macromolecular crystallite (conduction band). An important parameter in the band theory is the Fermi level, which determines the top of the available electron energy levels at low temperatures (0 K).

The magnitude of the fixed energy gap between the electronically populated valence band and conduction band governs the behavior of semiconductor. When adding energy to semiconductor, either by heating or irradiating, band gap determines the necessary energy for excitation of electron from valence band to conduction band. [15]

Photoexcitation by radiation with energy greater than the band gap creates electronic vacancy or “hole” at the valence band (Vb) edge (h_{vb}^+) and photogenerated electron (e^-) which usually moves to the conduction band (Cb) forming (e^-_{cb}) upon thermal relaxation. Further relaxation of (e^-_{cb}) is more difficult as the energetic mismatching or the energies of electron and hole.

$$\boldsymbol{TiO_2 \overset{hv}{\rightarrow} e_{cb}^- + h_{vb}^+} \quad (1)$$

Semiconductors lack a continuum of interband states to mediate the recombination process of electron-hole pair therefore their lifetime is sufficient to allow these species to participate in interfacial electron transfer. When components of this activated pair are transferred across the interface, a reduction and oxidizing reactions can be observed on surface-adsorbed substrate, forming semiconductors surface singly oxidized electron donor and singly reduced electron acceptor.

Another effect attributed with the initial phase of photodegradation of adsorbed organic matter on the semiconductors can be observed when the semiconductor is in contact with electrolyte containing a redox couple. In this case, the fermi level of semiconductor moves to equilibrate with the potential of redox couple and contact area of semiconductor and electrolyte creates so called Schotky barrier. Its electric field induces spatial separation of photogenerated electrons and holes. [16] The amount of band-bending in this Schottky Junction depends on the difference of the Fermi levels of semiconductor and electrolyte. Region, where the bending is presented, is called the space charge layer (SCL). Main property of this region is a cumulation of electrons or holes on the surface. [17, 19] Charge carriers are driven to surface trapping sites either by duffusion or by migration induced by the space-charge gradient. Formation of Schotky barrier on the surface of semiconductor and electrolyte containing redox couple is demonstrated on figure 3 and figure 4 represents the band gap energies for various semiconductors.

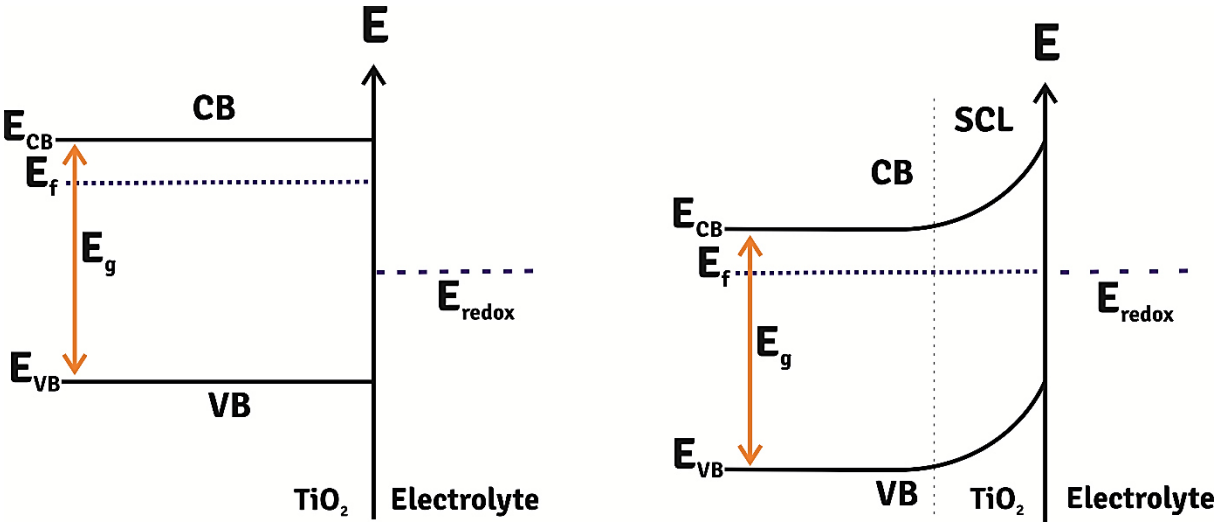

Fig. 3 Formation of Schotky barrier on the surface of irradiated TiO_2 and electrolyte [20]

Photogenerated hole on the surface of semiconductor can react with an adsorbed substrate by interfacial electron transfer, assuming that the adsorbate possesses a redox potential appropriate for a thermodynamically allowed reaction. Thus, an adsorbed electron donor (D) can be oxidized by transferring an electron to a photogenerated hole on the surface, and an adsorbed electron acceptor (A) can be reduced by accepting an electron from the surface. According to reactions 2, 3 hole trapping generates a cation radical, $D^{\cdot+}$ and electron trapping generates an anion radical $A^{\cdot-}$.

$$\mathbf{h_{vb}}^{+} + \mathbf{D} \rightarrow \mathbf{D}^{\cdot+} \tag{2}$$

$$\mathbf{e_{cb}}^{-} + \mathbf{A} \rightarrow \mathbf{A}^{\cdot-} \tag{3}$$

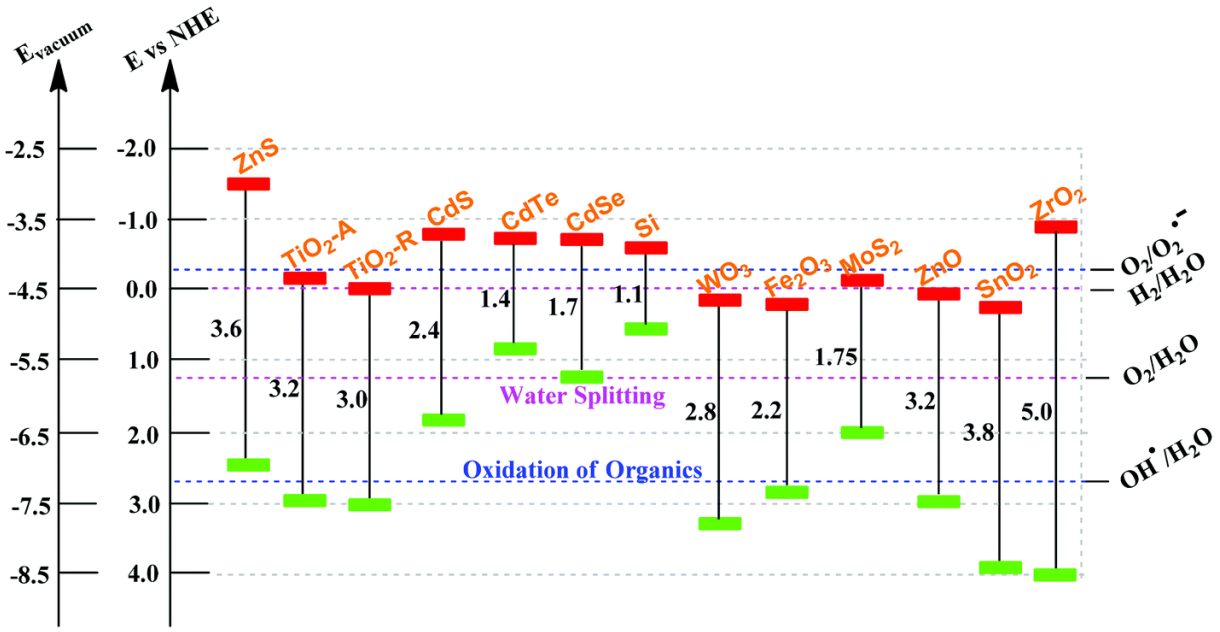

Fig 4. Eg (Ev) for various semiconductors on a potential scale versus normal hydrogen electrode (NHE) [21]

There are several pathways for reactions of created radical ions:

- Chemical reaction with other adsorbates.
- Recombination by back electron transfer forming excited state of one of the reactants, or nonradiative pathway.
- Diffusion from the semiconductor surface and participation in chemical reaction of bulk solution.

When the rate of formation of cation radicals $D^{\cdot+}$ is competitive with the rate of electron back transfer, photoinduced oxidation will occur for adsorbed molecules with oxidation potential less positive than the semiconductor valence band edge. Under these conditions interfacial electron transfer is thermodynamically allowed. Analogically photoinduced reduction will occur when any molecule possessing a reduction potential less negative than the conduction band edge of semiconductor.

3.3.2 Carrier trapping

The efficiency of photocatalytic reaction is often determined by the electron-hole recombination. To suppress this process the trapping either photogenerated electron or photogenerated hole is necessary. The rate of carrier trapping must be rapid if efficient conversion of the absorbed photon to a chemically stored redox equivalent is to be achieved. In TiO_2 for example the electron-hole recombination occurs within nanoseconds. The required rate for carrier traping must be faster than diffusion, so that the species acting as the carrier trap must be preassociated with the photocatalyst surface before the arrival of the activating photon.

Charge carrier trapping occurs at the surface and in the bulk of the semiconductor. It could be advantageous if charge carriers are localized at important electron transfer sites on the TiO_2 surface or if it promotes charge carrier separation. On the other hand, it can also be reducing the photocatalytic activity, when trapping sites are far from electron transfer sites. [22] In semiconductors, lattice imperfections are typically the source of trapping sites. Taking into account energy, two types of trapping can be distinguished.

Shallow trapping sites exist under conduction band minimum or above valence band minimum. Energy, associated with these trapping, is close to the thermal excitation energy. Surface states are typical example of shallow trapping sites, created by dangling of bonds at the surfaces. Typical shallow trapping sites are oxygen vacancies or localized Ti^{3+} sites at the TiO_2 surface when annealed in vacuum. [23,25] Shallow states usually act as dopant if they satisfay the condition of valency one less or one more than the host atom with nearly same atomic size.

Deep trapping exists in the bandgap and the energy which is associated with it is usually higher than thermal excitation at a given temperature. The recombination process for deep level traps is usually non-radiative. Deep trapping is most effective as a recombination center if the hole capture time is nearly the same as the electron capture time.

Hole trapping is usually achieved by the use of degradable adsorbates or sacrificial reagent. For example, trimethylamine and hydroquinone have been used successfully as sacrificial electron donors in CdS-mediated photoreductions, [26] functioning as hole traps so that the conduction band electron is transferred slowly without significant electron-hole recombination. In general, hole trapping occurs with sufficient efficiency that enough charge is built up on a particle resulting in its migration through electrophoretic field. [27]

Electron trapping is often accomplished by oxygen in air, or by adsorbed protons resulting into the oxidative cleavage or complete mineralization of organic substrate adsorbed on the TiO_2 surface. Variation of molecular oxygen adsorption between rutile and anatase leads to the higher rate of electron-hole recombination on rutile, caused by lower capacity to adsorb O_2. [28] Therefore, althought both forms of TiO_2 are thermodynamically able to reduce oxygen, the photocatalytic activity of anatase is significantly higher, compared with rutile.

3.3.3 Active sites

Considering surface reactivity of TiO_2, the number of surface active sites determines the photocatalytic performance. Active sites are sites on surface, where the reactants tend to adsorb and react with photogenerated charge carriers and eventually lead to new products. Obviously, a surface area and surface morphology take a big part in the successful photocatalytic decomposition. Surface structure is responsible for binding strength of photocatalysts with the reactants. [29, 30] For example facets orientation has became a studied theme, because of its influence on transfer pattern of carriers as the photoinduced electrons and holes can be separately driven to different crystal facets, facilitating the charge separation. [31, 32] Two mechanisms of adsorption are presented on active sites.

During physisorption there is no chemical bonding between adsorbed molecules and surface of TiO_2. There are week Van der Waals interactions presented between surface and adsorbates. Due to this fact, binding energy of species involved in physisorption is relatively low (10 – 100 meV).

Chemisorption is prevalent adsorption mechanism among heterogenous photocatalytic systems. It is represented by strong chemical bond in a monolayer on the surface upon transfer (ionic bonds) or sharing (covalent bonds) of electrons between adsorbates and surface. It also modifies the density and position of electronic

states of the surface-adsorbate complex. Binding energy is high (1 – 10 eV).

Kinetics of these proceses is depicted in chapter 3.4.1.

3.3.4 Mechanism of photocatalytic performance

Photocatalysis happens in certain conditions, after irradiation of TiO_2 surface by UV light with higher energy than ʎ = 388 nm for anatase, respectively ʎ = 413 nm for rutile. After irradiation the electrons and holes are created and before their own recombination they are participating in surface reactions. There are many kinds of reactions, which can be accomplished through photocatalysis. These can involve oxidations and oxidative cleavages, reductions, geometric and valence isomerizations, substitutions, condensations, polymerizations, etc. [15, 25]

The valence bond holes are powerful oxidants with potential of +1.0 to +3.5 V against normal hydrogen electrode depending on the semiconductor and pH as can be observed in figure 4. As good reductants the conduction band electrons are used showing measurable potential of +0.5 to -1.5V against normal hydrogen electrode. Simplified mechanism of reactions of electrons and holes on active sites is proposed in following figure:

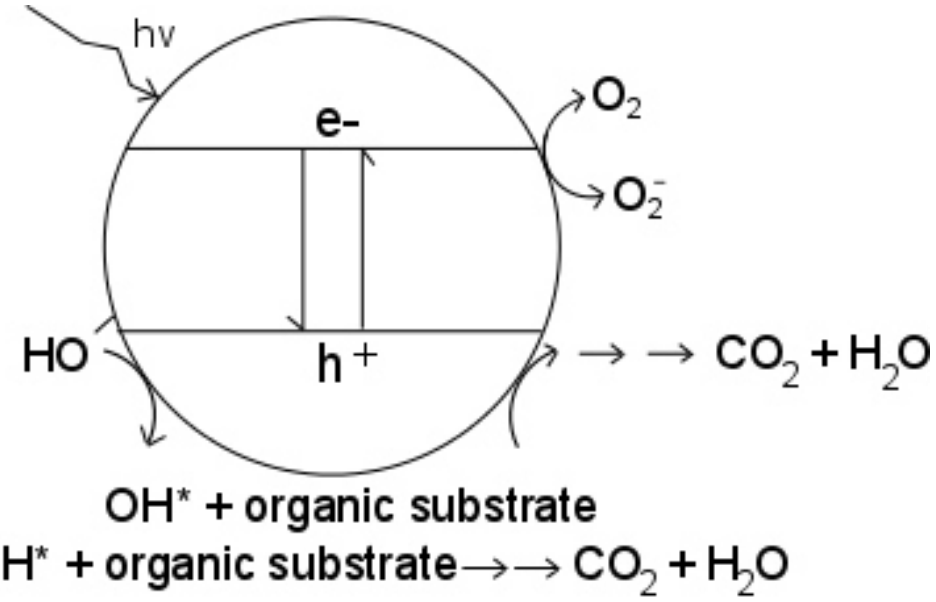

Fig. 5 Mechanism of photocatalytic decomposition

Capability of electrons and holes reducing and oxidizing an adsorbate in active site can be explained by following cascade of reactions: [33]

- $TiO_2\ (h_{vb}^+) + H_2O_{ads} \rightarrow TiO_2 + HO^{\cdot}_{ads} + H^+$ (4)
- $TiO_2\ (h_{vb}^+) + HO^-_{ads} \rightarrow TiO_2 + HO^{\cdot}_{ads}$ (5)
- $HO^{\cdot}_{ads} + D_{ads} \rightarrow D_{oxid}$ (6)
- $TiO_2\ (h_{vb}^+) + D_{ads} \rightarrow TiO_2 + D^+_{ads}$ (7)
- $TiO_2\ (e^-_{cb}) + A_{ads} \rightarrow TiO_2 + A^-_{ads}$ (8)

According to the mentioned equations, formation of singly oxidized electron donor and a singly reduced electron acceptor is achieved during photocatalytic decomposition,

repetition of reactions leads to the complete mineralization of organic addsorbates on the surface of TiO_2.

3.3.4.1 Hydroxyl radical

The most important reactive specie formed during photocatalytic reaction is considered to be $OH^{\cdot}$ radical. Althought there are two major possible ways of its formation, it is generally concluded that the hole capture is proceeding directly through adsorbed OH and not via water first, therefore reaction 6 is more likely to be prevalent than reaction 5. In general, it is believed, that radical-cation of water formed at reaction 5 may be neutralized before decomposing into $OH^{\cdot}$ radical.

It is also mostly assumed, that the irradiated surface is OH covered and therefore the hole is directly transferred to OH. Therefore involvement of the surface-bonded hydroxy radical in heterogeneous photocatalytic conversions conducted in contact with an aqueous solution must be considered in each scheme. [34] Even in acidic conditions, proposing the surface-bonded OH radical creation has significance, during considering of reaction scheme.

The presence of OH radical on the surface of TiO_2 upon irradiation is so obvious, proved and known fact, that it is used as chemically equivalent to surface-trapped hole and these terms are used interchangeably by investigators. It can be concluded, that principal charge trapping event is formation of surface OH group, which is initiating primary oxidation chemistry of adsorbates bonded at the surface, before diffusing into the bulk solution.

Various studies of photocatalytic decomposition confirmed hydroxylated intermediates formation in aquaeous TiO_2 suspensions during decomposition. Such products could be formed by homolytic attack of hydroxyl radical on π system of organics or by hydration of singly oxidized intermediates. [15, 25, 35, 36]

3.3.4.2 Superoxide radical

Another important specie which appeared at earlier mentioned cascade of reactions, is superoxide radical $O_2^{\cdot -}$. Its formation is conducted according to the equation 8, where in general the A stand for the adsorbed O_2. It was observed, that photocatalytic activity is completely suppressed in the absence of an electron scavenger, such as molecular oxygen.

As the conduction band of TiO_2 is almost completely isoenergetic with the reduction potential of oxygen in inert solvents, adsorbed oxygen serves as an efficient trap for photogenerated electrons. Superoxide is highly active and apart of attacking other adsorbed molecules, can be also source for another hydroxyl radical formation, which is described by following reactions. [33]

- $TiO_2\ (e^-_{cb}) + O_{2\ ads} + H^+ \rightarrow TiO_2 + HO^{\cdot}_2 \leftrightarrow O_2^{\cdot -} + H^+$ (9)
- $2\ HO^{\cdot}_2 + H^+ \rightarrow H_2O_2 + O_2$ (10)
- $H_2O_2 + O_2^{\cdot -} \rightarrow HO^{\cdot} + O_2 + HO^-$ (11)
- $H_2O_2 + h\nu \rightarrow 2HO^{\cdot}$ (12)
- $H_2O_2 + TiO_2\ (e^-_{cb}) \rightarrow HO^{\cdot} + HO^-$ (13)

Oxygen concentration dependence has been explained as involving O_2 adsorption and depletion, both in the dark and during illumination, at photocatalyst surface.It is attacking both neutral substrates and adsorbed radicals and ionts. This attack occurs before desorption from the surface since the presence of dissolved superoxide traps

in solution does not inhibit photocatalytic oxidative reactivity. [37] Also, according to reactions of oxygen superoxide radical, a protonation-reduction-protonation sequence is capable to generate hydrogen peroxide H_2O_2. This specie is one of initiate oxidative functional groups for interconversions.

3.3.5 Photoinduced superhydrophilicity of TiO_2 surfaces.

Superhydrophilicity is another very important property of irradiated TiO_2 surfaces and is accompanying the photocatalytic reactions. Very well described possible mechanism of superhydrophilicity behavior under irradiation of TiO_2 surface is described by Hashimoto, Irie and Fujishima. [38]

Thin TiO_2 film exhibits an initial contact angle (CA) of several tens of degrees depending mainly on the surface roughness. After its exposition to the UV light, the CA starts immediately to decrease reaching almost 0°. In this stage surface is completely hydrophilic resulting into the spread of drops of water over it. Even after two days of storage in the dark the CA angle remains so small that the surface is still hydrophilic. After this time CA angle slowly increases and the initial CA of UV unexposed TiO_2 surface recovers. To explain this phenomena, various studies were done. [39 – 42]

It was found out that photo-produced hydrophilic behavior of TiO_2 surface can be broken by external stimuli. For example, ultrasonic treatment has impact on the CA, changing the CA from nearly 0° to 10° during ultrasonication period. [43] Similar behavior was found using mechanochemical “wet rubbing” method for the surface treatment with clean lint-free paper. In this case CA raised from 3° to 80°. [44]

Althought, some works supposed the superhydrophilicity is a result of photocatalytic decomposition mechanism, leaving the surface perfectly clean [45 – 47], Hashimoto [38] claims that the oxidative decomposition can make the surface only moderately hydrophilic with CA of 10 – 20° under ambient conditions. In fact there are always some stains presented on the TiO_2 thin films surface.

The creation of surface metastable state is responsible for its superhydrophilicity behavior. It is concluded, that this state is crated upon increasement of the number of hydroxyl groups on the TiO_2 surface after the UV irradiation [48]. On the surface the chemisorbed OH groups and adsorbed molecular water is presented. After irradiation the amount of OH groups increases with increase of hydrophilicity. Therefore Hashimoto suppose that the pohotogenerated holes, not the electrons, are responsible for the hydrophilic conversion of surface. Althought most of them are consumed for the reaction with adsorbed organics directly or adsorbed water, producing OH radicals, a small portion of the trapped holes may react with TiO_2 itself, breaking the bond between the lattice titanium and oxygen ions by the coordination of water molecules at the titanium site. Coordinated water molecules realease protons for charge compensation and new OH formation, therefore the increasement of OH groups at the surface can be observed.

Increasing amount of chemisorbed OH groups leads to the increase of Van der Waals and hydrogen bridges bonding with adsorbed surface water molecules. Therefore the water can be spread over the surface and superhydrophilic behavior of surface appears. Adsorption is not uniformed over all surface, creating hydrophilic and hydrophobic places with several nanometers scale. Hydrophilic places are spread along with oxygen atoms bonded in structure of TiO_2 with two Ti atoms. Formation of superhydrophilic surface is shown in figure 6.

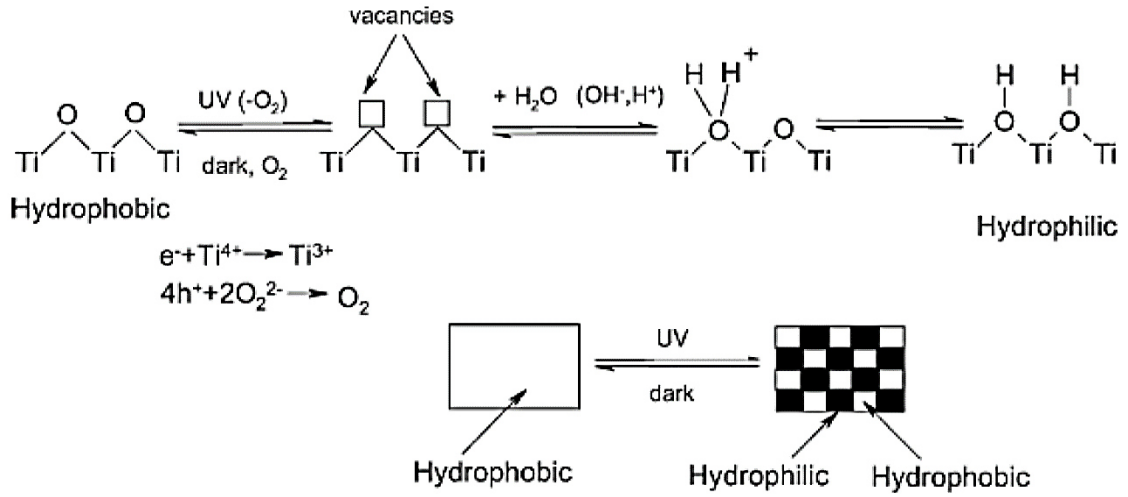

Fig. 6 Formation of superhydrophilic surface of TiO_2 [49]

Superhydrophilic surface formation is responsible for the self-cleaning function of TiO_2 coatings rather than pohotcatalytic decomposition considering outdoors materials. Stains are removed from the hydrophilic surface by rainfall easily. Very important property of superhydrophilic TiO_2 surfaces is antifogging function where thin uniform water film formed over the surface is preventing the formation of droplets.

3.4 Kinetics of heterogenous photocatalytic surface reactions on TiO_2

Heterogenous photocatalytic surface reactions are performed on the surface of irradiated TiO_2 and gaseous or liqiudous reaction mixture. Following steps are involved in photocatalytic reaction:

- Migration of reactants from reaction mixture to the surface of photocatalyst.
- Diffusion of reactants from the outer surface of photocatalyst to the inner surface of photocatalyst.
- Adsorption of reactants on the surface at active sites of photocatalyst.
- Chemical reaction on adsorbates at active sites.
- Dessorption of products from the active sites of photocatalyst.

Kinetics is impacted by the slowest step from the mentioned steps. In majority of reactions, there are mainly two steps strongly affecting the rate of reactions, according to the reactions conditions.

Diffusion of reactants from the outer surface of photocatalyst to the inner surface of photocatalyst, which is driven by Fick laws, where the impact factors are porous structure of photocatalyst and pore diameter along with particles diameter and concentration gradients and with diffusion coeficients.

Another impacting step is adsorption of reactants on the surface at active sites of photocatalyst. For example, the catalytic performance of photocatalyst can be reduced in presence of water molecules, hence without them there wouldn´t be any photocatalytic reaction at all. This is caused by the competitive adsorption of reactants and water presence in active sites of photocatalyst. [15, 50, 51]

Presence of water over photocatalyst surface is therefore with increasing concentration firstly increasing photocatalytic performance at lower concentrations working as catalysator of overall reaction. But further increasement results in reducing the photocatalytic performance while water is acting as inhibitor of reaction.

Reaction kinetics of heterogenous photocatalytic surface reactions on TiO_2 is mostly following the reaction kinetics of reactions of 0 and 1 order, modified with usage of Langmuir-Hinshelwood kinetic mechanism for heterogenous catalysis.

3.4.1 Langmuir-Hinshelwood kinetic mechanism for heterogenous catalysis.

This kinetic model is most important model for heterogenous catalysis. For its application following assumes are done:

- Number of surface adsorption sites during reaction is fixed.
- Only one substrate may bind at each surface site.
- The heat of adsorption by substrate is identical for each site.
- No interaction between adjacent adsorbed molecules.
- Rate of surface adsorption of substrate is greater than the rate of any subsequent chemical reactions.
- There is no irreversible blocking of active sites by formed products.

Mechanism is based on the reaction of adsorbates on the surface of photocatalyst. Following expression of kinetic equation is used:

$$v = -\frac{dc}{dt} = k \cdot \theta_A \cdot \theta_B \tag{14}$$

θ_A, θ_B are the degrees of coverage of photocatalyst by A a B, k stands for the rate constant.

Using Langmuir equation, which is depicting the degree of coverage, kinetic equation can be modified in following steps:

$$\theta_A = \frac{K_A \cdot c_A}{1 + K_A \cdot c_A + K_B \cdot c_B} \tag{15}$$

$$\theta_A = \frac{K_B \cdot c_{AB}}{1 + K_A \cdot c_A + K_B \cdot c_B} \tag{16}$$

$$v = -\frac{dc}{dt} = k \cdot \theta_A \cdot \theta_B = \frac{k \cdot K_A \cdot K_B \cdot c_a \cdot c_b}{(1 + K_A \cdot c_A + K_B \cdot c_B)^2} \tag{17}$$

K_a, K_b are Langmuir´s adsorption constants; c_a, c_b are concentration of A, B; k is true rate constant; v is the reaction rate

Simplyfied description of heterogenous photocatalytic reactions is given by equation of reaction rate:

$$v = \frac{k \cdot K \cdot c}{1 + K \cdot c} \tag{18}$$

At low concentration of reactants, the expression $K \cdot c$ can be withdrawn from the equation resulting in simplified equation 19:

$$v = k \cdot K \cdot c \tag{19}$$

Expresing dependence of concentration of reactant upon time and volume of system, another equations are formed, expressing parameters in equation 19:

$$-V \frac{dc}{dt} = \frac{m \cdot A \cdot k \cdot K \cdot c}{1 + K \cdot c} \tag{20}$$

$$-\frac{m \cdot A}{V} t = \frac{1}{k \cdot K} \ln \frac{c}{c_0} + \frac{c - c_0}{k} \tag{21}$$

V is volume of system; *A* is number of active sites per photocatalyst mass in grams; *m* stands for the mass of photocatalyst.

Half life of decay $\tau_{1/2}$ is described by equation 22:

$$\tau_{1/2} = \frac{\frac{\ln 2}{k \cdot K} + \frac{c_0}{2 \cdot k}}{\frac{m \cdot A}{V}} \tag{22}$$

If the concentration of reactant on the beginning c_0 is significantly lower than $1/K$, half-time of decomposition is independent on reactant concentration, but on concentration of photocatalyst (m/V) and its reactiveness ($k \cdot K$). [51, 52]

Main advantage of proposed Langmuir-Hinshelwood mechanism is avoiding of the necessity for a complex mathematical formulation of surface binding. However there is a need for several experimentally underterminable parameters and it still possesses inherent limitations. [15, 53].

Because a basic assumption of the Langmuir-Hishelwood kinetic mechanism is the surface preadsorption requirement, a broad range of reaction rates might reasonably be expected from differences in adsorptive affinity of different substrates on a given irradiated TiO_2 surface. However the observed rates ($k \cdot K$) are surprisingly similar in different reactions that have been studied. [15, 54]

3.5 Preparation and deposition of TiO_2 by sol-gel processes

Nowadays, there is possible to distinguish two deposition pathways of TiO_2 for usage in photocatalytic decomposition. TiO_2 is either used in powder form, taking advantage of powder usage (higher surface area than when applied on the surface of holder) or as immobilized media on the porous inert holder. First pathway of application is slightly economically disadvantageous due to the requirement on the withdrawal from the cleaned photocatalytic system. [55]

Althought usage of TiO_2 on immobilized media with the porous inert holder shows lower photocatalytic rate, due to the economical impacts, its usage is broader than in powder form. Another advantage is a possibility to apply very thin layer of TiO_2, which leads to the short diffusion length for pollutants and formed electron holes and electrons. It is advantageous to improve the specific surface by pore introduction into the surface of such materials. [55, 56]

3.5.1 Sol-gel method

One of the most common and very effective way, how to obtain TiO_2 photocatalyst, is sol-gel method. It can be used for preparation of powders with narrow distribution and thin coatings with homogenous crystallite structure. In a typical sol-gel process, a colloidal suspension or sol, is formed by controlled hydrolysis and polycondensation reaction of inorganic metal salts or organometallic precursors. During the process, liquid sol is transformed into a solid gel phase during polymerization and loss of solvent. Mechanism of hydrolysis and polycondensation reactions is described in chapter 3.6.

Advantages of sol-gel method are homogenous, transparent and porous crystallic structures preparation accompanied with easibility, purity and low-cost of prepared materials.

Hence some disadvanges are limiting the use of substrate in surface coating, as such produced coating needs to be thermal treated at several houndreds of °C to prepare crystalline structure. Therefore the substrate must be able to withstand high temperature treatment. High temperature also means, that the inertness of substrate toward reaction with surface treatment at high temperatures needs to be examined in order to prevent the drop in surface properties. [57]

3.5.1.1 Mechanism of sol-gel

Starting compounds in sol-gel are metal alkoxides, or metal acetylacetates. These precursors are hydrolysed and produced sol undergoes polycondensation and polymerization.

In general, the overall process can be devided into several steps:

- Preparation of sol by controlled hydrolysis of alkoxides.
- Formation of gel throught polycondensations of sol and crosslinkings of oxides and alcohols leading to the increase of viscosity.
- Syneresion of gel which is characterized by ongoing polycondensation reaction and aging of the gel.
- Drying of gel when molecules of water and solvents are removed by heating.
- Calcination of the dryed gel for removing the rests of organic compounds and hydroxyl groups from xerogel.

During calcination, heating at temperature 200 – 300 °C, removes remained traces of organic compounds, whereas heating at temperature 300 – 400 °C removes hydroxyl traces in structure and initiate the formation of crystallite structures of surface coatings. This microstructure can be also affected by usage of varous aditives during sol-gel process, for example polyethylenglycols are responsible for porosity, or varying molar rates of sol components and used solvent mixture. [58, 59]

3.5.2 Sol – gel thin film TiO_2 deposition processes

There was developed many different pathways of deposition of thin TiO_2 surfaces on various substrates. Brief information about thickness of coating and characteristics of methods are given below. [57]

- Spin coating – method based on circulating of substrate with coating dispersion. Speed of rotation, concentration of sol, type of solvent and surface tension have impact on the thickness of layer. Possible range of thickness is varying between 1 – 200 μm.
- Dip coating – substrate is put into the coating dispersion and withdrawn with controlled rate. Thickness of surface layer is driven by rate of withdrawing, viscosity of sol and angle of withdrawing. Highly optical quality is obtained with thickness of coating between 20 nm – 50 μm.
- Cappilary coating – in this method, under the surface of substrate, coating cylindric roller partially dipped into the coating dispersion is rotating creating menisc and laminar coating conditions are created. Homogenous, highly optical quality thin film with thickness around 15 μm is created.
- Cell coating – the coating dispersion is poured into the cell created by two planes of substrates. Thickness of coating depends on the thickness of cell created between planes of substrate.
- Flow coating – the coating dispersion is poured on the substrate. Thickness depends on the angle between substrate and poured dispersion, viscosity and rate of evaporation of solvent. Advantage is easy smoothing of surface defects of substrate.
- Print coating – this method is done by printing of liquidous coating dispersion on various substrates surfaces. It is a quick process with possibility of regulation of surface thickness during printing and with good reproducibility and reduced waste production. Printing is possible to introduce on the ceramic, metallic, organic semiconductor and biopolymeric substrates. [55, 57]

3.6 Hydrolysis of transition metals

In sol-gel processes, the formation and growth of nanoparticles of TiO_2 are accomplished by hydrolysis and condensations of alkoxides precursors. Main disadavantage of this process is the fact, that Ti^4 ions are highly electropositive and easily undergo nucleophilic attack by water, which leads to the fast and uncontrollable hydrolysis resulting into various specious of precipitates. [60, 61] Due to the fast kinetics of hydrolysis and condensation reactions of TiO_2 alkoxides, relatively little information is available concerning progressive structural evolution in transition metal oxide systems.

3.6.1 Mechanism of hydrolysis

In general, hydrolysis is process when interactions of atoms lead to the exchange of charge between filled $3a_1$ bonding orbital of water molecule and empty *d* orbitals of the transition metals (M). When dissolved in pure water, metal cations M^{z+} are solvated by water molecules, establishing following equilibria, defined as hydrolysis: [62]

$$[M(OH_2)]^{z+} \leftrightarrow [M\text{-}OH]^{(z-1)+} + H^+ \leftrightarrow [M{=}O]\ ]^{(z-1)+} + 2H^+ \quad (23)$$

There are three types of ligands presented in noncomplexing aqueous media:

- $M(OH_2)$ – Aquo
- M-OH – Hydroxo
- M=O – Oxo

Then the rough formula for inorganic precursor can be written as $[MO_NH_{2N-R}]^{(z-R)+}$. *N* is the coordination number of water molecules around M, *Z* is the charge and R is molar ratio of hydrolysis. If R = 0, the precursor is aquo-ion, when *R* = 2*N* precursor is an oxy-ion and similarly, another oxo-hydroxo complex $[MO_x\,(OH)_{N-x}]^{(N+x-z)-}$ (*R* > *N*), hydroxo-aquo complex $[M(OH)_x(OH_2)_{N-x}]^{(z-x)+}$ (*R* < *N*) and finaly hydroxo complex $[M(OH)_N]^{(N-z)-}$ (*R* = *N*) can be formed.

Charge density on the metal, number of metal ions bridged by hydroxo or oxo ligand and number of hydrogen atomes contained in the ligand are facilitating the hydrolysis whereas increasing number of hydroxo ligands coordinating M is inhibiting it. Precise nature of formed complex during hydrolysis is dependent on charge, coordination number and electrongativity of metal and pH of aqueous solution. Figure 7 shows diagram for the presence of aquo, hydroxo and oxo ligands upon charge of metal cations and pH.

As can be concluded from the diagram in figure 7, the hydrolysis of low-valent cations with *Z* < 4 yields aquo, hydroxo or aquo-hydroxo complexes with decreasing pH, while oxo or oxo-hydroxo complexes are formed at high valent cations with *z* higher than 5. Tetravalent metals are on the border therefore they have ability to form all kind of complexes depending on the pH. [64]

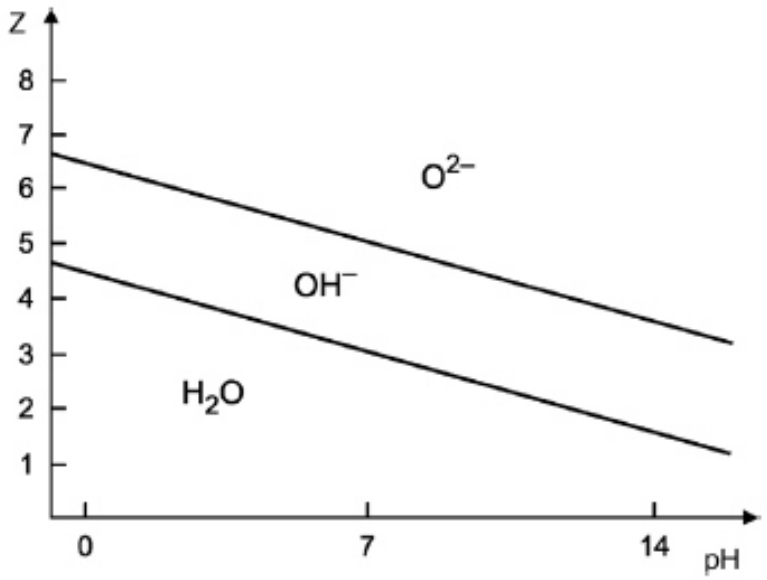

Fig. 7 The effect of pH of solution and charge of M [63]

Partial-charge model was derived from the diagram in figure 7 expressing the quantification of pH relation with the valence of M. When interaction of atoms proceeds, each participating atom has positive or negative partial charge. Transfer of electrons will stop as soon as the electrongativity of all partners in system is equal to the average value of electronegativity. [62]

3.6.2 Condensation of precursors

3.6.2.1 Nucleophilic mechanism

Depending on the coordination of metal precursor, there could be two nucleophilic mechanisms of condensation.

Nucleophilic substitution (S_N) takes place if the preffered coordination is satisfied:

$$M_1{-}OX \;+\; M_2{-}OY \longrightarrow M_1{-}\overset{\overset{X}{|}}{O}{-}M_2 \;+\; OY \qquad (24)$$

Nucleophilic addition is creating attendant increase in the coordination number of M_2 and proceeds when the preferred coordination is not satisfied.

$$M_1{-}OX \;+\; M_2{-}OY \longrightarrow M_1{-}\overset{\overset{X}{|}}{O}{-}M_2{-}OY \qquad (25)$$

3.6.2.2 Olation

During olation condensation process, hydroxy bridge is formed between two metal centers. For coordinatively saturated hydroxo-aquo precursors, olation take place through nucleophilic substitution where hydroxyl group is the nucleophile and water ir the leaving group. According to some studies, olation occurs via a reaction intermediate involving H_3O_2 bridging ligands. Also different types of OH bridges can be formed as demonstrated at following reactions. [63, 64]

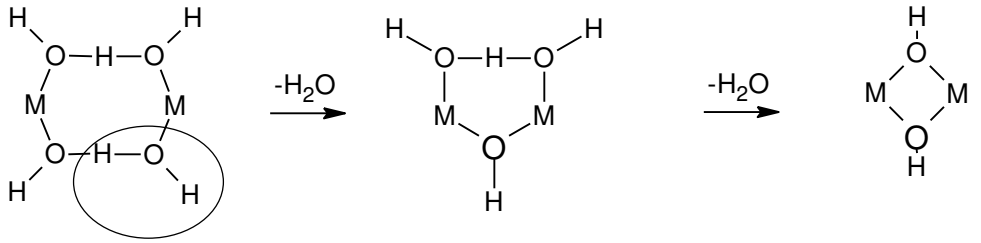

(26)

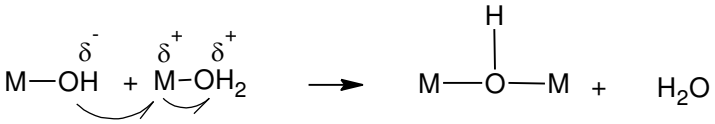

(27)

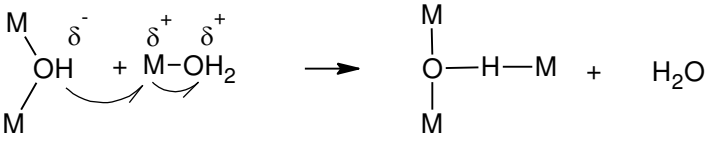

(28)

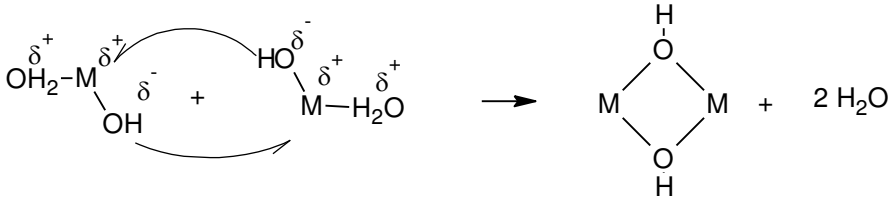

(29)

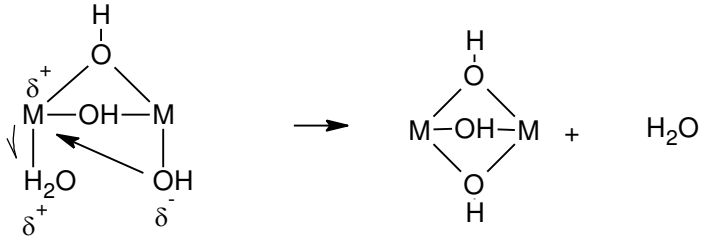

(30)

Kinetics of olation is related to the lability of the aquo ligand, because H_2O is the leaving group. Size, electronegativity and electronic configuration of M are influencing the lability of aquo ligand. In general, the rate of olation is grater with smaller charge and larger size. As the electron-donating aquo ligands are removed during olation, the S_N mechanism of olation is limited. The reaction stops when partial charge (δ) of (OH) ≥ 0. Condensation in certain pH regimes is limited to dimers (Cu^{2+}, Ti^{3+}, Fe^{3+}, Mn^{2+}) or tetramers (Zr^{4+}, Hf^{4+}, Co^{3+}). These oligomers (polymers containing a few repeat units) are the final products of hydrolysis and condensation in a narrow range of pH.

3.6.2.3 Oxolation

This type of condensation reaction is producing oxo bridges in between two metal centers. If metal is coordinately unsaturated, oxolation occurs by nucleophilic addition with rapid kinetics leading to edge or face-shared polyhedral, as shown in following reactions pathways.

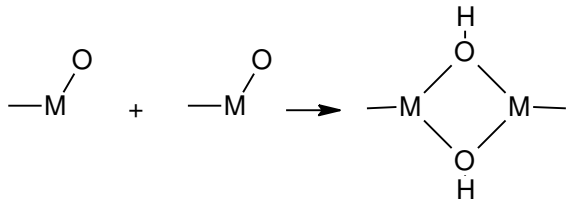

(31)

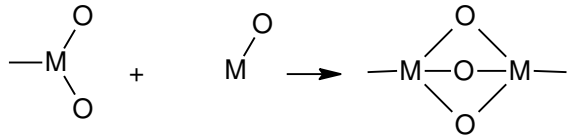

(32)

When coordinatively saturated metals are participationg in this reaction, oxolation proceeds by a two-step reaction with nucleophilic substitution between oxyhydroxy precursors involving nucleophilic addition followed by water elimination.

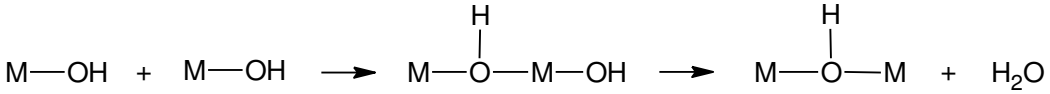

(33)

First step is catalyzed by bases deprotonationg the hydroxo ligands creating stronger nucleophiles as seen on reactions.

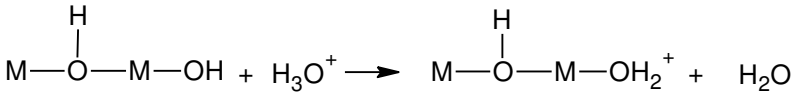

(34)

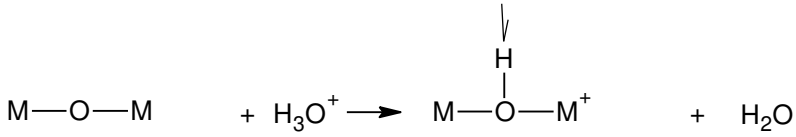

(35)

Second step is catalyzed by acids protonating hydroxo ligands creating better leaving groups.

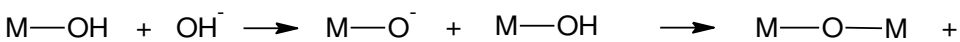

(36)

Oxolation occurs over a wide range of pH. However due to the two-step process, kinetics are slower and also the diffusion is not the controlling mechanism. Oxolation kinetics are minimized at the isoelectric point where species $[MO_{z-N}(OH)_{2N-z}]^{(0)}$ are predominant.

3.6.3 Hydrolysis and condensation of transition metal alkoxides.

For coordinatively saturated metals in the absence of catalyst, the result of hydrolysis and condensation occur by nucleophilic substitution involving nucleophilic addition where at the and the proton is transferred from the attacking molecule of water to alkoxide or hydroxo-ligand within the transition state and removal of protonated species as either alcohol (alcoxolation) or water (oxolation). When $N - z > 0$, also olation can occur as condensation reaction. Products of hydrolysis and condensation of Ti-alkoxides are below.

- Hydrolysis → M-OH + ROH
- Acoxolation → M-O-M +ROH
- Oxolation → M-O-M + H_2O
- Olation →M-OH-M + ROH ; M-OH-M + H_2O

Overall reactions happening during the condensation of Ti alkoxides can be written as follows: [62, 64]

≡Ti-OR + H_2O → ≡Ti-OH + R(OH) (37)

≡Ti-OH + RO-Ti≡ → Ti-O-Ti≡ + R(OH) (38)

Thermodynamics of hydrolysis, alcoxolation and oxolation are governed by the strength of entering nucleophile, electrophilicity of M and partial charge and stability of leaving group. These reactions are favoured when δ(O) « 0, δ(M) » 0, and δ(H_2O) or δ(ROH) >0.

Thermodynamics of olation depend on the strength of the entering nucleophile and electrophilicity of the metal. The kinetics of olation are fast because $N - Z > 0$ and no proton transfer occurs in the transition state.

3.7 Reactivness of Ti alkoxides

The most common usage of alkoxides of Titania include ethoxy, isopropoxy and butoxy alkoxides. These compounds have smooth reaction with water resulting in variety of Ti hydroxides and hydrated oxides. Structure of condensed products depends on the relative rates of earlier mentioned four reactions: hydrolysis, oxolation, alcoxolation and olation. Their contribution to final product depend in internal parameters, such as the nature of the alkyl groups and the molecular complexity as well as external parameters, such as concentration, solvent, temperature and *R*.

In general, hydrolysis rate decreases with the growing alkyl chain length. This is according also to the steric effect, which could be expected for an associative Sn reaction mechanism. In addition, partial charge of Ti and partial charge of H are decreasing with length of alkyl chain in Ti alkoxides. Another explanation of this fact could be that the initial condensation of products is producing oligomeric species that subsequently aggregate to form gels or precipitates. These oligomers are -R dependent, with increasing -R the size of oligomers decreases. -R groups also exerts and influence on the morphology (particle size and surface area) and crystallization behavior of resulting formed gel influencing perhaps the structure of primary oligomeric building blocks.

When the size of oligomers decreases, the equivalent oxide products content in hydrolysis products decrease as well. This can be observed at fig. 10 showing decrease of oxide content in hydrolysis products of Ti-butoxide upon hydrolysis *R*. [61]

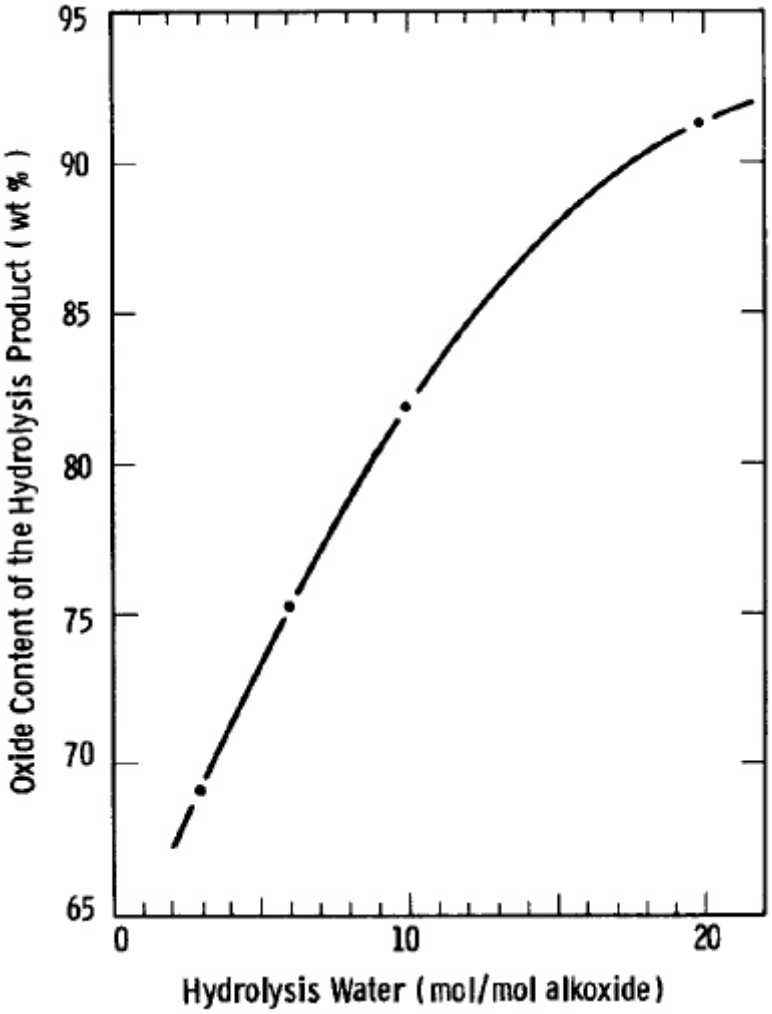

Fig. 8 Content of TiO_2 oxide in hydrolysed Titanium butoxide after drying with varying *R* [61]

If the hydrolysis is done in ethanol or when higher titanium alkoxides are hydrolysed in lower alcohols, the observed curve in figure 8 flattens considerably as the limiting factor of polymerization is diffusion. The role of water / alkoxide ratio during hydrolytic condensation is one of the parameters that determine the molecular size and polymer morphology.

Bullent and co-workers [61] suggests a hydrolytic polycondensation equation which would take into account this variability of oxide content and the polymeric nature of the condensates:

$$n\mathrm{Ti(OR)_4} + (4n + x - y)\mathrm{H_2O} \rightarrow \mathrm{TiO_{[2n-(x-y)/2]}(OH)_x(OR)_y} + (4n - y)\mathrm{R(OH)} \quad (39)$$

- n – number of titanium ions polymerized in a condensation
- y – number of OH groups in the molecule
- x – number of OR groups in the molecule

Polymer size *n* and nature of terminal bonds *y*, *x* determine the oxide content of compound as shown in reaction 40.

$$TiO_{[2n-(x-y)/2]}(OH)_x(OR)_y \rightarrow {}_nTiO_2 + {}_xH_2O + {}_yR(OH) \quad (40)$$

With increasing of the polymer size the equivalent oxide content increase from the beginning rapidly, then it levels off. The concentration of (OR) groups decreases when increasing the water content in hydrolysis medium. Certain concentration of OR groups remains in structure independently to the amount of water present. The evidence of these group can be observed, when heating the hydrolysed condensates. It can be sought that these groups burns upon heating, depositing regularly carbon in the powder around 185 – 190°C, when the polycondensate is produced from Titanium ethoxide. During heating, also liberation of hydroxyl groups can be observed. In contrary to OR burning, this effect takes place more gradually, resulting in complete weight loss due to the OH liberation around 300°C. [65]

Another effect to morphology of condensate is the usage of solvent medium. When hydrolytic condensation of Ti-alkoxides is carried out in lower alcohols, then used alkoxide, the higher equivalent oxide content is observed. This is reflecting a greater degree of polymerization as well as ester-exchange of heavier alkyls with lighter alkyls in Ti-alkoxides. As example the hydrolytic condensate of titanium ethoxide formed in ethanol has an equivalent oxide content around 83%, the same conditions of reaction with butanol as a solvent yields only 73% of equivalent oxide content.

3.7.1.1 Role of catalysts

Acid or base catalysts can influence hydrolysis and condensation rates and the structure of condensed products. Acids are protonating negatively charged alkoxide groups, enhancing the reaction kinetics by producing good leaving groups thus eliminating the requirement for proton transfer within the transition state. Equation 41 shows the reaction of alkoxide with hydroxo cation.

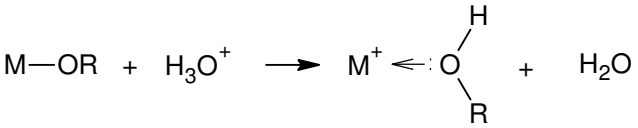

(41)

Hydrolysis is completed when sufficient water is added. The relative ease of protonation of different alkoxide ligands can influence the condensation pathway. If we consider partially hydrolyzed polymer species of Ti alkoxides.

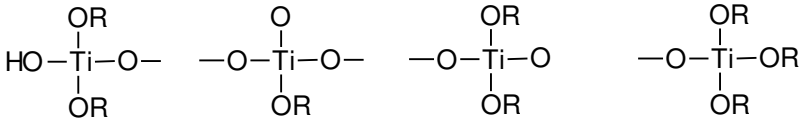

(A) (B) (C) (D)

Fig.9. Polymeric species during hydrolysis of Ti alkoxides

Partial charges of OR and Ti for species are calculated according the partial charge model in table 5.

Tab. 5 Calculated partial charges of polymeric species

specie	δ (OR)	δ (Ti)
A	-0.01	+0.70
B	+0.22	+0.76
C	+0.04	+0.71
D	-0.08	+0.68

The ease of protonation decreases as D » A > C » B reflecting electron-providing power of the ligands. This power decreases as alkoxy, hydroxo, oxo species are formed. The tendency of acid-catalyzed condensation is to react with the ends rather than the middles of chains, resulting in more extended, less branched polymers. To support this effect the observation that acid catalysts combined with low *r* values (water / metal ratio in alkoxide) often gives monolithic gels or spinnable sols. [61, 66 – 68] High concentrations of acidic catalysator severly retard the condensation kinetics.

Alkaline condition catalysis produce strong nucleophile by deprotonation of hydroxo ligands:

$$L\text{-}OH + :B \rightarrow L\text{-}O^- + BH^+ \quad (42)$$

Where L stands for M or H, B stands for OH^- or NH_3. Condensation kinetics are systematically enhanced under basic conditions. Based on the partial charge values of Ti from the table 5, the reactivity of species toward nucleophilic attack decrease in following order: B » C ≈ A > D. Therefore the more compact, highly branched species are obtained in base-catalyzed hydrolysis condensations.

Another effect is caused by introducing H_2O_2 into the system. It reacts vigorously with the condensation product even when hydrolysis was completed earlier with water. Created gels formed from clear solutions are shrinking rapidly from their mother liquor, but without loosing their shape. The reaction is independent on the amount of hydrogen peroxide and it is thought to be caused by removal of terminal alkyl groups with a coordination change. Conversion of alkyl bonds to hydroxyl bonds apparently initates reactions between dangling bonds, creating bridging oxygens and causing the collapse of the previously open polymer network. Also moderate heating is supporting the shrinkage of gels. [61]

3.7.2 Study of kinetics of Ti-alkoxides hydrolysis.

As the determining step of hydrolysis and polycondensation reactions is the addition of water into the mixture of Titanium alkoxide, study of hydrolysis kinetics is essential part of preparation gels and powders of TiO_2. Also the clear and complete picture for the formation of transition metal oxide particles has not still been obtained. Understanding the phenomena which is occurring during the initial stages of particle growth seems to be especially important, because this part of hydrolysis and condensation reactions can determine the properties of final products.

It is generally assumed, that the first stage of the sol-gel process in neutral conditions is formation of hydrolyzed monomers and their accumulation. The induction time corresponds to the moment when the concentration of these monomers reach the level of critical supersaturation. As a result of nucleation, primary particles are formed. They grow by monomer addition and aggregation. [70]

3.7.2.1 Mechanism of particles formation

Every precipitation reaction consist from two step process, nucleation of very fine particles from solution and their growth. In solution one of possible mechanisms for the formation of particles is preparing super-saturated solution. The change of Gibbs energy than can be explained as demonstrated below.

$$\Delta\hat{G} = (\mu_l - \mu_s) \tag{43}$$

Where the phases are expressed by their chemical potentials (μ_l, μ_s) and the change of Gibbs energy ($\Delta\hat{G}$) indicates, if the phase transformation between liquid to solid state is spontaneous ($\Delta\hat{G} < 0$), or thermodynamically not favoured ($\Delta\hat{G} > 0$).

The change of free Gibbs energy can be also expressed with use of saturation coefficient (S) which is deviding the actual concentration of ionts in solution (C) with the value of solvatation (C_{eq}) corresponding to the temperature and pressure of system) [71]

$$\boldsymbol{S = \frac{C}{C_{eq}}} \tag{44}$$

The $\Delta C = (C - C_{eq})$ is often used in literature as the driving force of the precipitation process.

Homogenous nucleation from supersaturated solution can be expressed as the thermodynamically favoured process happening upon the fluctuation of atoms concentration and local fluctuation of free energy of whole system. The nuclei formation and condensation into clusters happens, where the size of clusters (a) is given by Kelvin equation

$$\ln\frac{\boldsymbol{p}}{\boldsymbol{p_0}} = \frac{\boldsymbol{2\gamma v_1}}{\boldsymbol{kTa}} \tag{45}$$

Where p is the actual vapor pressure, p_0 is the saturated vapor pressure, γ is the specific surface tension energy, ν_l is the volume of molecule, formed by condensation, k is the Boltzman constant, T is absolute temperature of system and a is the radii of formed nuclei. For further reaction, the definition of critical size of nuclei (a_c) is formulated. If, upon the mentioned fluctuation, nuclei with size (a) appear, when ($a < a_c$), the nuclei can´t growth and they are transformed into the liquidous phase again. When ($a > a_c$), nuclei can exist in the solution and start to growth.

Energetic barrier must be overcome, if the nuclei are formed. This barrier corresponds to the change of the Free Gibbs Energy upon formation of nuclei (ΔG_n). In system, where round-shaped particles are formed with diameter a can be described by equation 46.

$$\Delta G_n = 4\pi a^2 \gamma - \left(\frac{4}{3}\right)\pi a^3 \Delta G_v \tag{46}$$

Total change of Free Gibbs energy upon defined volume of liquid (ΔG_v) is described in following equation:

$$\Delta G_v = \left(\frac{kT}{v_l}\right)\ln\left(\frac{p}{p_0}\right) \tag{47}$$

Activation energy of stable nuclei (ΔG_c) is dependent on the critical diameter of nuclei. If $d(\Delta G_c)/da = 0$, then the critical size of nuclei is described by equation 48 and the (ΔG_c) can be written as in equation 48.

$$a_c = \frac{2\gamma v_l}{kT\ln\frac{p}{p_0}} \tag{48}$$

$$\ln\frac{p}{p_0}\Delta G_c = \frac{16\pi\gamma^3 {v_l}^2}{3\left[kT\ln\frac{p}{p_0}\right]^2} = \frac{4}{3}\pi {a_c}^2 \gamma \tag{49}$$

Degree of nucleation (*I*) describes the further nucleation considering the ability of nuclei to condensate.

When considering also the hydration of M ionts, which are necessary for the nucleation and could be polymerized and create polynuclear ionts, using the mentioned equations and universal frequency expression from the equation 50, *I* can be expressed as shown in equation 51. [71, 72]

$$\nu = \frac{kT}{h} \tag{50}$$

$$\mathrm{I} = \frac{2N v_s (kT\gamma)^{1/2}{}_s}{h}\exp\left(\frac{-\Delta G_a}{kT}\right)\exp\left(\frac{-16\pi\gamma^3 {v_s}^2}{3k^3T^3\left[\ln\frac{C_{ss}}{C_s}\right]^2}\right) \tag{51}$$

N is the number of atoms at selected volume of solution, v_s the volume of formed molecule of solid phase, γ is specific surface energy of liquidus-solidus bondedary, $-\Delta G_a$ is activation energy, needed for the migration of ions, C_{ss} is the concentration of supersaturation and C_s is concentration of ionts in saturated solution. The rate of the nucleation process is dependent mainly on the coefficient of supersaturation *S*.

The rate of growth can be described in several levels considering the size of particles

- molecular
- microscopic
- macroscopic

The macroscopic point of view says the control of growth can be accomplished by control of mass transport in a system which is possible to exchange by the heat transfer, when the crystallization heat is high.

On the microscopic level, the particle agglomeration is presented always due to the decreasing rate of diffusion on the surface.

On the molecular point of view, the diffusion of growth particles into the crystal structure appears attacking themselves and becoming the part of crystal or leaving the crystal and coming back to the solution. Rate of growth is dependent by diffusion of reactants toward particle and continuous transfer of new molecules from surface reactions.

Narrow distribution of formed particles can be explained according to Lamer [69] diagram demonstrated at figure 9.

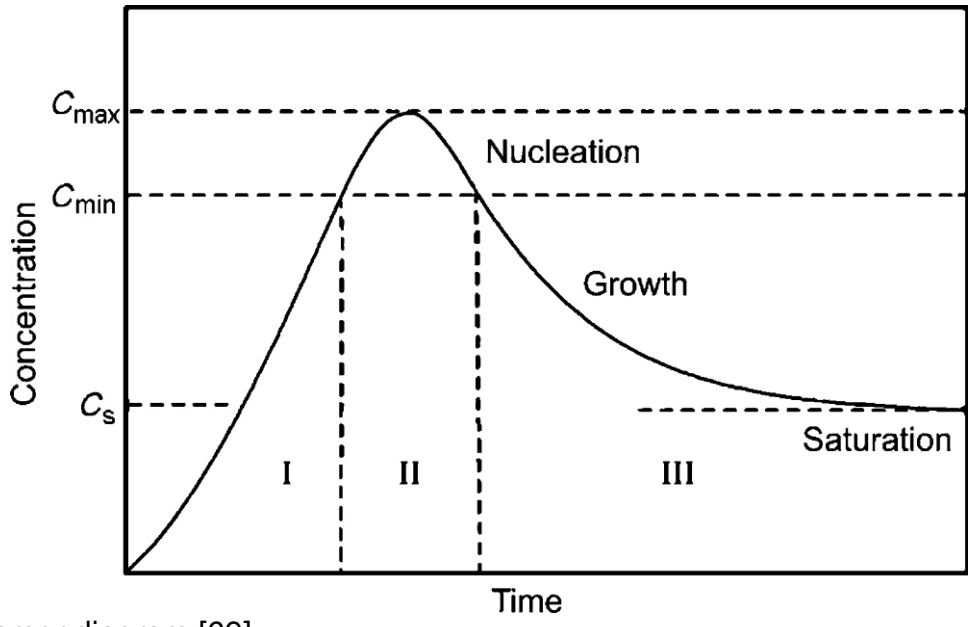

Fig. 9 Lamer diagram [69]

As the reaction proceeds, the concentration of the solute to be precipitated (C_x) increases to or above the saturation value (C_s). If the solution is free of foreign inclusions and the container walls are clean and smooth, then it is possible for C_x to exceed C_s by a large amount to give a supersaturated solution. Eventually a critical supersaturation concentration (C_{ss}=C_{max}) will be reached after some time t_1 and homogeneous nucleation and growth of solute particles will occur, leading to a decrease in C_x to a value below C_{ss} after a time t_2. Further growth of the particles occurs by diffusion of solute through the liquid and precipitation on to the particle surfaces. Finally, particle growth stops after a time t_3 when $C_x = C_s$. In general, the axis x can be replaced by the diameter of particle (a), where the critical nuclei size (a_c) lays in the supersaturated concentration maxima reached (c_{max}). Until this point the process of formation of nuclei is reversible, when crossing this boarderline, the process is irreversible.

This mechanism is used for the primary particles growth and it is not appropriate to be used when aggregates formation appers. Growth of particles by aggregation is connected with basic principles of colloidal chemistry. [69]

During precipitation freshly formed nuclei are migrating through the solution and grow very quickly due to the aggregation mechanism until they form stable colloidal dispersion. Particles with narrow distribution are formed when the nucleation rate is high, proceed on the beginning of the precipitation and the rate of nuclei growth is controlled.

3.7.2.2 Turbidimetry studies of precipitation kinetics

It is oftenly said, that the beginning of reaction starts when the significant turbidity of solution of reactants in sol-gel processes is observed. Time after addition of water with solvent mixture into the solution of Ti-alkoxide is marked as an induction period or induction time. This time is explained by LaMer´s model as accumulation and supersaturation of alkoxyhydroxytitanium molecules (partially or completely hydrolysed molecules of titanium alkoxide).

In figure 10 a typical turbidity measurement curve of hydrolysis of Ti-isopropoxide is presented with observed stages of precipitation development in the time scale.

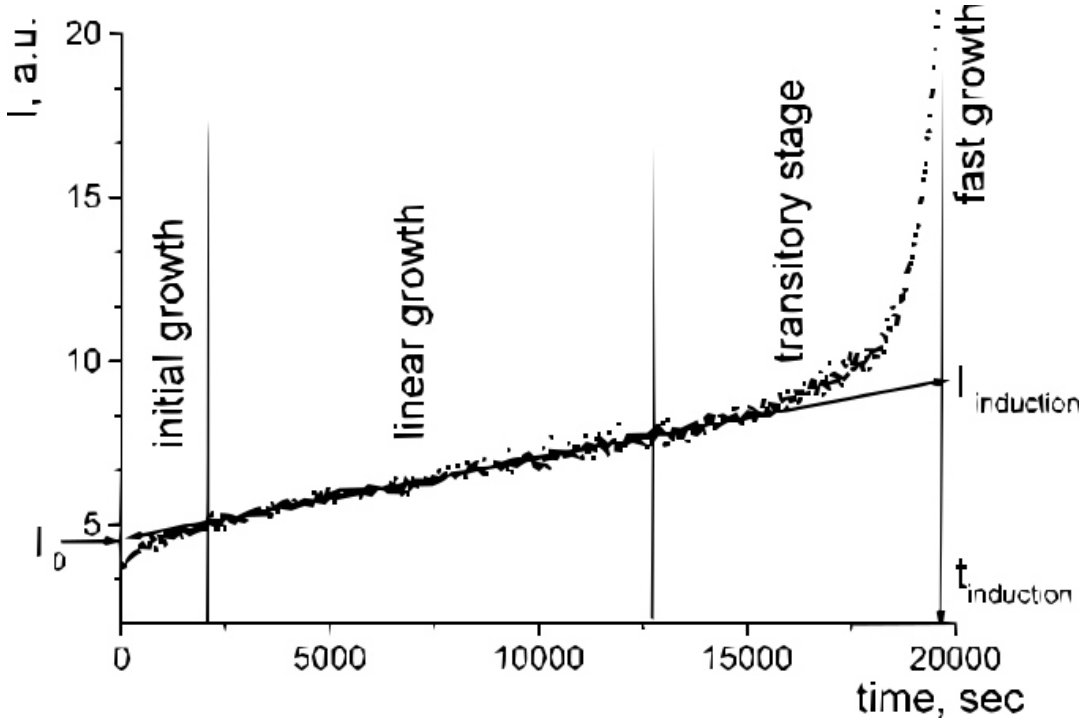

Fig. 10 Typical turbidity measurement of Ti-Isopropoxide hydrolysis curve [73]

According to fig. 10 during the precipitation of particles from the Ti-isopropoxide (TIPP), there could be 4 stages distinguished

- Initial growth
- Linear growth
- Transitory growth
- Fast growth stage

In Lamer´s model a hydrolyzed monomers accumulation is denoted as an explanation of induction time. However it has been proved by several studies, that initial hydrolysis is very fast, compared to the induction period. In favor of this contratory data, the presence of nanoparticles of radious 2-4 nm was observed during whole induction period of sol-gel process of TIPP, evaluated by direct light scattering (DLS). [74, 75]

Quite interesting turbidimetric study with introducing new idea about kinetics of formation of Ti-isopropoxide hydrolyzed products was given by A Soloviev and colleagues. [73] Their findings are revalidating the known Lamer diagram for Ti-alkoxides where exchanging the induction period explanation is given.

During initial growth phase, the very first nuclei are formed with high rate, as was revealed for example in the case of zirconium alkoxids hydrolysis and condensation study, using FTIR and small angle X-ray scattering (SAXS). [76] In that case the fast hydrolysis and condensation reaction proceeded in less than 1 second and primary particles were formed with a radius of 3 – 4 nm. Initial growth stage may be shorter, depending on the rate of micromixing during the addition of solution of water and solvent into the Ti-isopropoxide solution. Initial intensity (I_0) is appearing due to nuclei formation.

Linear growth of turbidity is corresponding to the aggregation growth of particles which turns through linear growth into the short transitory growth finished with fast growth. As suggested by A. Soloviev and coleagues observed change in kinetics can be attributed to the mechanism of aggregative stability. [73]

Aggregative stability depends on the surface charge and properties of electrical double layer near the surface. It was also observed, that this charge can exist even in neutral conditions, because of protonation of alkoxy and hydroxyl surface groups of particles by protons originating from dissociated water molecules.

When particles are growing, the aggregative stability is decreasing with their size and at some critical size is lost. This size could be corresponding to the radius of 4 nm as at this time the particle growth increases sharply, with formation of big particles with radius of several houndred nanometers accompanied with the progressive increase of turbidity in reaction mixture.

Corresponding to the critical particle radius for loosing the aggregative stability behavior, during their development, the rate limited aggregation process (RLA) which proceeds linearly may change into the diffusion-limited aggregation process (DLA) responsible for the very fast aggregation being the final process of Ti-alkoxides hydrolysis and condensation reactions. [77]

3.8 Magnetic particles for core-shell catalysts preparation

With increasing surface area of TiO_2 particles, the rate of photocatalytical degradation increases. As showed earlier, nanoparticles of TiO_2 have potential in various large scale photocatalytic applications. Nanoparticles are easy to prepare, are stable against degradation, possess high photocatalytical efficiency and are non-toxic. Hence, the use in catalytic and photocatalytic industry systems has limitations, given by easy loss of powder catalysator and its difficult and economically challenging regeneration. Mitigation of this disadvantage of TiO_2 powder use can be obtained by usage of suitable holder for crystalline TiO_2 particles forming core-shell catalyst.

Use of various solid substrates for the TiO_2 in photocatalytic applications was examined. Those included various materials prepared from glasses, silicagel, active carbon, clays and zeolites. To enhance the surface area, also porous materials were used. [78 – 80] Hence the photocatalytic activity in these materials decreases as the limited radiation distribution in photocatalytic systems and lower specific surface can be observed.

In order to gain advantage of high specific surface area of powders, the core-shell powder catalyst can be used with using magnetic nanoparticles as holders for photocatalytic active coatings of Ti-alkoxides. Such powders have competitive surface area and their main advantage is the easy and economical withdrawal from cleaning systems with use of external magnetic field. Therefore, the core-shell structure magnetic photocatalytic powders preparation is extensively studied among photocatalyst specialists

Significant number of magnetic powder materials with different elemental compositions have been used as the core, such as Fe_3O_4, γ-Fe_2O_3, black sand, $NiFe_2O_4$, $CoFe_2O_4$, FeCo, and Co_3O_4. [81 – 85]. Among them, nanoparticles of Fe_3O_4 and γ-Fe_2O_3 has drawn a lot of attention due to their mesoscopic effect, small object effect, quantumsize effect and high surface, remarkable magnetic properties, low toxicity, and biocompatibility [86, 87].

3.8.1 Magnetic iron oxide particles

Among known magnetic iron oxide particles, Magnetite (Fe_3O_4) and maghemite γ-Fe_2O_3 draw biggest attention due to their unique biochemical, catalytic and other properties combined with high magnetic saturation of 92 $emu \cdot g^{-1}$. [88]

Magnetite is a black, ferromagnetic mineral representing naturally-occurring oxides of iron. It is containing among divalent and trivalent Fe, both kinds of oxidized atoms of Fe, Fe^{2+} and Fe^{3+}. In stoichiometric magnetite, the rate Fe^{2+} / Fe^{3+} = 0.5. However magnetite is often non-stoichiometric resulting in a cation deficient Fe^{3+} layer. The crystal structure of magnetite is inverse spinel with a unit cell consisting of 32 oxygen atoms in a face-centered cubic structure and a unit cell length of 0.839 nm. In its crystal structure Fe^{2+} ions together with Fe^{3+} ions occupy tetrahedral sites, whereas divalent iron atoms prefer to occupy octahedral sites in order to have higher Crystal Field Stabilization Energy (CFSE), whilst the trivalent iron atoms have CFSE = 0 in both octahedral and tetrahedral sites. [89, 90]

Maghemite can be considered as Fe $^{2+}$ deficient magnetite which can be formed by weathering or oxidation of spinels containing iron, such as magnetite or titanomagnetite.

3.8.2 Preparation of magnetic iron oxide nano-particles

As the field of preparation of magnetic nanoparticles of Iron oxides is extensively studied, numerous methods for the preparation of such nanoparticles were developed.

- Electrochemical deposition
- Micro-emulsion
- Sol-gel processes
- Hydrothermal method
- Solvothermal synthesis
- Theromolysis
- Wet chemical processes
- Precipitation processes

Co-precipitation is very popular method for ultrafine nanoparticle preparation due to its ease, large volume capability and low economical demands in industrial use. Nanoparticles are precipitated form the mix of ferrous and ferric salts with initial ratio of 0.5 by adding solution of base, usually NaOH or NH_4OH as a precipitation agent. The used salts are usually chlorides and sulfates. [88]

In typicall coprecipitation process, solution of base is added into the solution of ferrous and ferric salt dropwise (titration). Solutions of Fe salts are acidic and with increasing pH the precipitation occurs, reaching pH close to 12 at the end of the reaction. At the end of the reaction, black magnetite precipitate is formed which indicates that the reaction is completed. Overall reaction which takes place during magnetite formation from the divalent and trivalent Fe salts solution by increasing pH is given in following reactions. [91-93]

$$2Fe^{3+} + Fe^{2+} + 8OH^- \rightarrow FeO.Fe_2O_3 + 4H_2O \quad (52)$$

Solubility of trivalent iron oxides is smaller than divalent iron oxides. Trivalent iron hydrolyzes and forms hydroxide species. This reaction can be induced by heating the reaction mixture and complete reaction of hydrolysis is represented by following chemical reaction:

$$(Fe(H_2O)_6)^{3+} \rightarrow FeOOH + 3H^+ + 4H_2O \quad (53)$$

Divalent iron cation of Fe reacts to form the divalent iron oxide in basic conditions according to following reaction:

$$Fe^{2+} + 2OH^- \rightarrow Fe(OH)_2 \quad (54)$$

As can be seen from reactions, divalent iron hydroxide and trivalent iron oxide-hydroxide are likely to be formed. This effect is suggesting that the following mechanism of reaction occurs when Fe_3O_4 is precipitated from such solution reaction mixtures: Firstly the trivalent iron oxide-hydroxide is formed in acidic solution. After that when adding base and increasing the concentration of hydroxide anions the divalent ferrous hydroxide is formed and this specie is reacting with the ferric oxide-hydroxide cation resulting in formation of magnetite at pH range 10 - 11 according to reaction:

$$Fe(OH)_2 + 2FeOOH \rightarrow Fe_3O_4 + 2H_2O \quad (55)$$

Beeing highly suspectible to oxidation, magnetite is transformed into the maghemite in the presence of oxygen according to the reaction:

$$4Fe_3O_4 + O_2 \rightarrow 6\ \gamma\text{-}Fe_2O_3 \quad (56)$$

Magnetite is ferromagnetic at room temperature and has a Curie temperature of 850 K. At room temperature, maghemite is ferromagnetic but unstable at high temperatures with loss of its susceptibility with time. Therefore its Curie temperature is hard to determine. [94]

Magnetic properties are dependent on size of prepared magnetic nanometric iron oxides particles. In general, magnetic Fe_3O_4 and γ-Fe_2O_3 nanoparticles with diameter less than 10 nm can exhibit super-paramagnetic properties acting as single magnetic domains without having any hysteresis loop. This superparamagnetic behavior can be explained by thermal fluctuation in material able to change the magnetization direction

of entire single crystals. Material with such crystals behaves like a paramagnete, except that the moments of entire crystals are fluctuating instead of individual atoms. [94]

In paramagnetic state, the individual atomic magnetic moments are randomly orientated having together zero net magnetic moment without presence of magnetic field. This is also possible to observe at ferromagnetic materials, when their temperature is reaching Curie point. With increasing particles size, the ferromagnetic properties of nanoparticles are dominating.

In ferromagnetic state two different types of atoms with opposite magnetic moments are presented. Therefore the material has a magnetic moment when the opposite moments are not equal. When an external magnetic field is applied to ferromagnetic material, magnetization increases with the strength of it until saturation. Hysterisis can be observed as over some range of magnetic fields, there is more than one stable magnetic field. This leads to the observation of remanent magnetization presented in such material even after removing the external magnetic field.

3.8.3 Modification of Iron oxide nano-particles surfaces

In photocatalytic uses, the direct coating of magnetic iron oxide nanoparticels suffer with some dissadvatages. When applying TiO_2 layer over magnetic iron oxide nanoparticles, after irradiation of photocatalyst, photogenerated charge carriers in the excited titania can be transferred to Fe_3O_4 or γ-Fe_2O_3 phase because of their lower lying conduction band and upper lying valence band.

The narrower band gap of Fe_3O_4 is also thought to lead to an increase in the incidence of electron–hole recombination and subsequently lower the photoactivity of magnetite/titania composite photocatalyst.

Moreover, the formation of preffered anatase phase of TiO_2 on the surface of magnetite is challenging as the high temperature treatment is needed. Such high temperatures can induce change in magnetic holder resulting in formation of antiferromagnetic α-Fe_2O_3 with very small saturation magnetization of 1 $emu \cdot g^{-1}$.

Direct interaction of TiO_2 with surface of magnetic iron oxide nanoparticles can also induce the transformation of TiO_2 and surface of nanoparticle into the different phase called titanomagnetite. The observations were done revealing that the significant reduction of photocatalytic activity appears when no treatment of magnetic surface of iron oxide nanoparticles is done. This is attributed to the increasing rate of recombination of electron – hole pairs. [95, 96] In general, development of low temperature processes for the formation of thin smooth layers of TiO_2 over easy magnetically separable iron oxides with no impact on the photocatalytic performance is needed.

The most common pretreatment of surface is applying SiO_2 layer on the surface of iron oxide nanoparticles. SiO_2 coating acts as an introduction of wide-bandgap electronic barrier and inhibits the iron oxide surface becoming a recombination center for electrons and holes. The most common application is coating of magnetic iron oxide particles prior to further TiO_2 coating

An example of this usage can be observed for example in Hongfei Liu and co-workers study [97]. In their work the powder photocatalyst preparation the magnetic particles of Fe_3O_4 are used as seeds for the SiO_2 sol-gel coating with resulting 75 – 85 nm particles diameter. After coating by Ti-butoxide the diameter increased to 100 nm. High efficiency of degradation in solution against rhodamine B colouring dye was observed. Particles had high specific surface area reaching almost 500 $m^2 \cdot g^{-1}$ and regeneration testing circle revealed consistent efficiency after eight regenerating circles.

SiO_2 serves also as adsorbent of dye molecules [98] which is confirmed in work of Xiaoxia Yu and co-workers dealing with structures of surfaces under chemical vapor deposition (CVD) TiO_2 aplication. [99] They prepared composite γ-$Fe_2O_3 \cdot SiO_2 \cdot TiO_2$ powder photocatalyst with sandwich structure by three grade synthesis of particles. CVD process of TiO_2 application was used where the Fe_3O_4 particles were transformed into the porous γ-$Fe_2O_3 \cdot TiO_2$ particles. When applying SiO_2 interlayer on the γ-Fe_2O_3 surface before TiO_2, significantly higher adsorption properties of material were observed. Prepared particles sizes were houndreds of nm. The photocatalytic activity of particles was higher when applying the SiO_2 interlayer.

Thanks to the adsorption behavior and wide-bandgap barrier introduction, the SiO_2 is also used as interlayer in work of Jingjing Xu and co-workers. [100] In their study principles for the preparation of anatase layer with low-temperature process, using only 75°C heat treatment are discussed in this work. Anatase layers were prepared by Ti-butoxide as a precursor and photocatalytic decomposition was tested on the phenol solution decomposition. Enhanced photocatalytic activity was obtained due to the low temperature process and SiO_2 interlayer coating.

Not only SiO_2 layer is beneficial when preparing core-shell powder photocatalysts. As indicated in work of Wang at all in their work, the carbon shell of Fe_3O_4 particles was more compact than other shells usually preferred. Then the direct contact of interacting phases is more effectively avoided. This benefit can enhance the photocatalytic activity and extend the lifetime of magnetic photocatalyst. [101]

Introducing the carbon layer is examined in work of A. Hasanpour and co-workers. [102] Modified sol-gel process is discussed in this work. As modificating agent, the sodium citrate was used to cover the surface of Fe_3O_4. Due to the good adhesion forces, the TiO_2 layer formed using Ti-butioxide could be easily formed from earlier calcinated TiO_2 nanoparticles and no further temperature treatment was assessed when using the TiO_2 particles to be bondeded by modified Fe_3O_4 layer. No interaction or interdifussion was observed at the interlayer of TiO_2 and Fe_3O_4. Prepared particles had diameter of 10 nm and thickness of TiO_2 layer was 5 nm.

Novel $Fe_3O_4/C/TiO_2$ multicore shell powder photocatalyst is prepared via vapor phase hydrolysis (VPH) process in work of Fuzhi Shi and co-workers. [103] Carbon layer is formed as described by Wang and co-workers. [101]. The dissolution of glucose in aquaeous solution containinc oleic-acid-stabilized Fe_3O_4 particles with diameter range of 150 – 200 nm is followed by autoclaving at 170°C for 3 hours. Sol-gel process using Ti-butoxide with ethanol was used to produce vapor phase and drying at 60°C followed. The photocatalyst content of TiO_2 was only 37% weight but exhibited relatively higher

activity than commercial anatase TiO_2. Formed interlayer of carbon avoided the photodissolution of Fe_3O_4 effectively.

In work of Tarek and co-workers powder photocatalysts preparation and photocatalytic activity is tested. [104] Catalysts are $Fe_3O_4/SiO_2/TiO_2$ and $C/Fe_3O_4/SiO_2/TiO_2$ multicore shell particles prepared by sol-gel method and final carbon layer in $C/Fe_3O_4/SiO_2/TiO_2$ catalyst is deposited by heating of $Fe_3O_4/SiO_2/TiO_2$ in presence of PVA as a source of carbon. For $C/Fe_3O_4/SiO_2/TiO_2$ photocatalyst the significant reduction of photocatalytic properties is observed. Rate of metyl orange degradation drops significantly when carbon layer was formed, containing only 0.2 % weight of carbon and there was no photocatalytic activity recorded, when content of carbon increased to 1% weight.

However, some studies report the photocatalytic activity can increase when applying the TiO_2 directly to be in a contact with oxides. A novel powder photocatalyst preparation is discussed in work of Tina Harifi and Majid Montazer. [105] Photocatalyst was formed upon reaction of salts of Fe in the solution of nanoparticles of TiO_2. TiO_2 nanoparticles were dispersed in the solution of Fe salts and the co-precipitation started with adition of base. Optimum $Fe^{2+}/TiO_2 = 2$ was selected.

As the previous studies dealt with core-shell in this case it is evident that in core-shell structures the charge carriers are transmitted to the conduction and valence band of magnetite and it is difficult for reducing and oxidizing species to access them through the layer of uniform TiO_2.

In prepared powder core shell catalyst structure, the existence of Fe_3O_4 particles on the surface of TiO_2 can be observed and the transferred carriers are easy to acces by reducing and oxidizing species. Morover, the Fe_3O_4 particles can retard the electron-hole recombination. Photocatalytic performance was higher than that of Deggusa P-25 and still enough saturation magnetization 22 $emu \cdot g^{-1}$ of particles was measured.

3.9 Photocatalytic measurement

Decomposition of efluents of contaminants into environment is of a big attention nowadays. Chemical, industrial and agricultural waste is composed of large spectrum of organic pollutants, which are frequently toxic to environment, especially organic compounds conaining aromatical rings which are mostly toxic to aquatic system. Althought decomposition of toxic waste compounds in environment can be observed, its rate is usually too small or incomplete and many of them are able to persist and accumulate in environment, which has negative impact on the environmental processes.

Over past decades, the physical techniques for the removal of organic pollutants from wastewaters and gass efluents were developed, including the adsorption, biological treatment, coagulation, ion exchange, ultrafiltration and other separative methods. Still these methods are in several cases ineffective and economically dependent. For example adsorption technology does not decompose pollutants and it is necessary to regenerate adsorbent for reuse, which leads to incrase of costs of treatment. Traditional biological treatments are often ineffective as the molecules, being mostly aromatic, are chemically and physically stable and also. It is known fact, that some of these compounds have big influence on the environment creating demage to

environment even in very low concentrations. These are for example hormones, various medicine drugs, etc. [15]

Heterogenous photocatalysis has been successfully used in the oxidation, decontamination or mineralization of organic and inorganic pollutants. By far, irradiated TiO_2 in photocatalytical phase of anatase, suspended in aerated water, has proved to be the most active photocatalyst for this purpose.

Large amount of chemical substances have been already subjected to succesfull photodegradation in liquidous systems over various modified or unmodified anatase surfaces. These include a group of phenol and its derivatives, fluoro alkanes or fluorarmotacis, organochlorine compounds, halogenated acids, dioxins, surfactants as dodecylbenzensulfonate, benzyldodeclydimethylammonium chloride, various phosphorous componds including organophosphates insecticides, and organophosphonic acids. Even dichlorodiphenyltrichloroethane, known as DDT can be successfully decomposed by photocatalytical decomposition. Most of these pollutants have cancerogenetic properties, are highly toxic to various kinds of organisms including human being and have high solubility in water. [15, 106 – 111]

3.9.1 Photocatalytical decomposition of dyes

Many dyes are decolorized and ultimately mineralized by photocatalysis. Organic dyes are presenting a large photoabsorption coefficients and therefore measurements of their concentrations in solutions are easy done by UV-VIS spectrometers even if the concentrations are very low.

In general, dyes are optimal compounds of studying the photocatalytic activity, as the typical loss of 10 – 15% of dyes are observed into the sewage discharge in textile industry, and moreover low biodegradability often accompanied with carcinogenetic properties is predicting them to pose great threat to human health and environmental ecosystems. Nowadays, for their decomposition, only ozone method is widely used for treating the printing and dyeing waste water. However, this oxidative reaction has selective degradation to organic matter and organic compounds and dosage and amount of azo groups have a great impact on treatment results.

Dissadvantage of measuring the photocatalytical decomposition of these dyes is that a photoreaction might be induced by visible-light photoabsorption (dye sensitization) as well as by photoabsorption of dyes. If dyes are used as model for the photocatalytical decomposition, a special care over the photocatalytic instrumentation must be taken for interpretation of experimental results as followed properties have impact on measurement:

- Dyes are absorbing photons in the visible range and are thus photoexcited before the measurement
- Absolute molar amount of dye contained in the reaction is much smaller than that of solid photocatalyst
- Degradation of dye mechanism is so difficult, that the quantum yieald efficiency can´t be estimated.
- They are innapropriate for testing the visible photocatalytic decomposition

Advantage of using dye in photocatalytic system is the fact, that only spectrometer is necessary for the measurement of the consumption of dye during photocatalytic degradation test.

3.9.2 Azo dyes

Azo dyes are most dangerous compounds, as their ability is to realease aromatic amine structures which are cancerous. Even though, they are occupying the major part of textile dyeing industry, due to their cheap preparation, coloring properties and good stability. When decomposed, the degradation rate decreases in the order monoazo-diazo-triazo. Three processes are happening simultaneously, when degrading dye by photocatalysis: [112]

- Photocatalytic degradation
- Spectral sensitization
- Suppresing recombination of electron-hole pair. (One moiety of dye molecule is serving in this process)

3.9.3 Methylene Blue Decomposition

In proposed thesis, the photocatalytical decomposition of methylene blue using the prepared magnetically separable powder photocatalysts. Its structure is shown at figure 19.

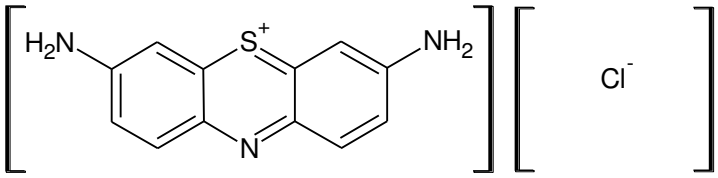

Fig. 19. Methylene Blue

As many studies were evaluating the photocatalytical decomposition of Methylene blue, the processes happening during photocatalytical decomposition of this dye is quite known. [112, 113]

In typical UV-Vis absorbtion spectra of Methylene blue, two major absorbance peaks blue can be observed, located at 292 and 664 nm. These are corresponding to the benzene ring and heteropolyaromatic linkage. In photocatalytic degradation, the double-peak feature at 615 and 664 nm representing dimers and monomers of MB is important. As the rate of the decomposition of dimers of MB is higher than monomers decomposition, the significant increase of absorption peak at 615 nm upon photocatalytic decomposition is observed. Due to this behavior, it is also easier to distinguish between adsorption of methylene blue on the powder photocatalyst and the photocatalytically active decomposition of the MB. When MB is irradiated, the blue shift of absorbtion peak at 664 nm can be observed due to the hypsochromic effect. [113]

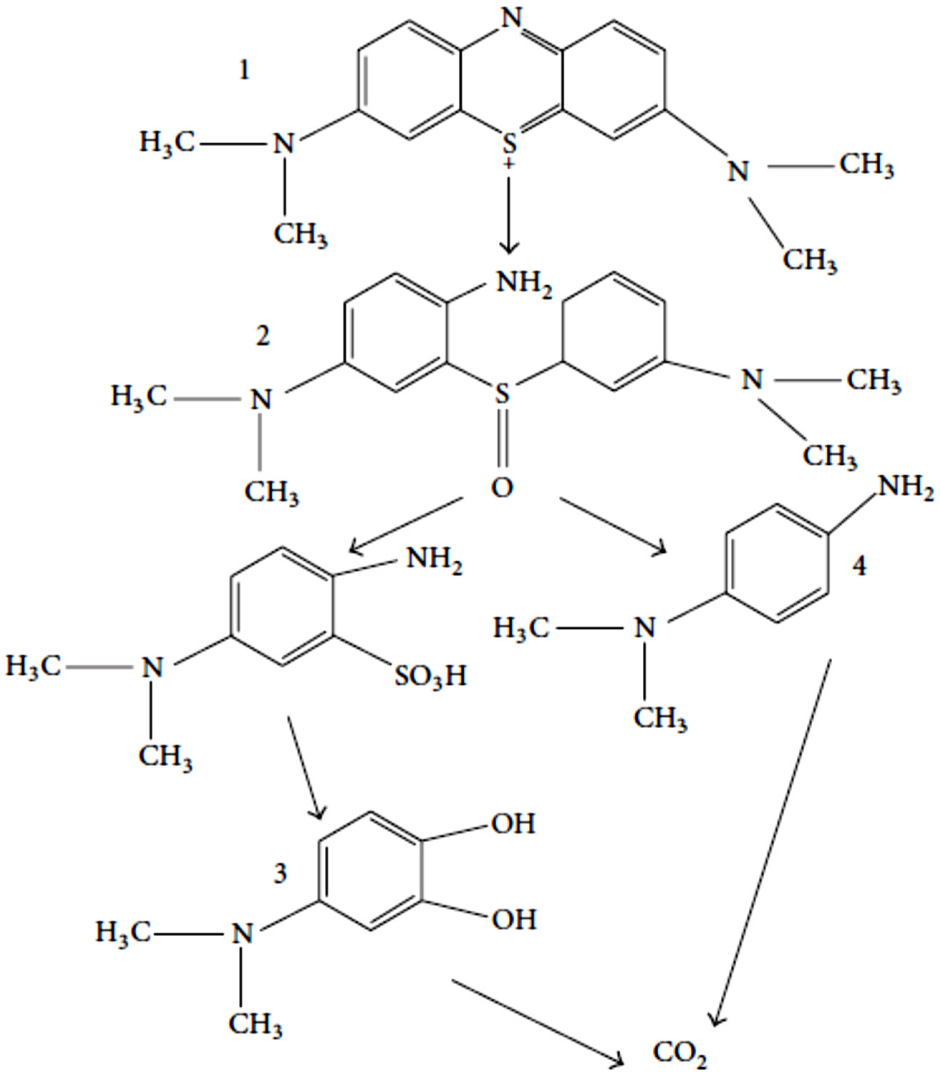

Fig. 20. Decomposition scheme of MB in photocatalytic reactor [113]

As shown on figure 20 the initial step in photocatalytic decomposition of MB is the cleavage of the bonds of the C-S^+=C in the midle central aromatic ring, containing both heteroatoms N and S. During this step double bond conjugation system is preserved. Further photocatalytic decomposition leads to the cleavage of both remaining aromatic rings connected through S and final mineralization of MB is observed forming CO_2, NH_3, sulfate and nitrate ions. [112, 113]

3.9.4 Photocatalytic decomposition of solvent vapors

Althought numerous studies dealed with the photocatalytic degradation of various organic substances in aquaeous environment, the literature on photocatalytic reactions involving gaseous reactants decomposed with TiO_2 is sparse. Widely used solvents such as methanol, ethanol and isopropanol, etc. are huge sources of anthropogenic emmisions of volatile organic compounds (VOCs). For example, 6% of them are accounted to ethanol in France and this number is even much bigger in case of using the vehicles fuelled by ethanol as for example in Sao Paulo or Rio de Janeiro. It is known fact, that vapors of these solvents are mostly considered toxic for the organism,

when inhaled. Therefore photocatalyzed oxidative removal of trace contaminants from air is a growing research area. Gas-solid heterogeneous photocatalytic oxidation of such contaminants shows potential to be used as air treatment and purification technology because of its broad applicability to common, oxidizable air contaminants. [114, 115]

The estimation of photocatalytic decomposition rate in case of degradation of gaseous phases is sometimes very challenging. For example in case of ethanol usually only acetaldehyde is determined as an intermediate at concentration that practically coincides with the reduced ethanolic flow, considering its adsorption on surface of photocatalyslyst since both molecules occupy the sam active centers. Some studies suggests that formed acetaldehyde reacts only when all ethanol is eliminated from the surface as the both molecules occupy the same active centers. [114, 116]

Better results of photocatalytic decomposition are obtained in case of 1-propanol and 2-propanol as the surface of photocatalyst is not deactivated and propanal, propanoic acid and acetaldehyde as degradation products can be observed. However the formation of CO_2 is usually not consistent with the photocatalytic efficiency for gaseous solvents degradation and it is generally observed that much higher photocatalytic degradation rate are measured for the decomposition of solvents in aqueous states. [116]

4 EXPERIMENTAL PART

4.1 Definition of Characterization Techniques

4.1.1 X-ray diffraction analysis

X-ray diffraction (XRD) is an analytical technique used for phase identification of crystalline material. Crystals are regular arrays of atoms and X-rays can be considered as waves of electromagnetic radiation. Atomic electrons scatter X-ray waves by a phenomenom known as elastic scattering, producing secondary spherical waves emanating from electrons. Regular array of atoms produces a regular array of spherical waves. These waves are cancelling each through destructive interference, they add constructively in a few specific directions which are determined by Bragg´s law in equation following reaction:

$$2d \cdot sin\ \theta = n\lambda \tag{57}$$

d is spacing between diffracting planes of atoms, θ is the incident angle, n is any integer and λ is wavelength of the beam. This law relates the wavelength of electromagnetic radiation to the diffraction angle and the lattice spacing in a crystalline sample. These diffracted X-rays are then detected, processed and counted.

X-rays are generated by a cathode ray tube and filtered to produce monochromatic radiation. They are used as their wavelength is typically the same order of magnitude (1 – 100 angstroms) as the spacing between planes in the crystals. Collimation is used to concentrate the direction of rays toward the sample.

By scanning the sample through a range of 2θ angles, all possible diffraction directions of the lattice should be attained due to the random orientation of powdered materials. Conversion of the diffraction peaks to d-spacing allows identification of the mineral because each mineral has a set of unique d-spacing. Typically, this is achieved by comparison of d-spacing with standard reference patterns obtained from databases. [117]

XRD can be used for:

- Identification of unknown crystalline materials. (e.g. minerals, inorganic compounds)
- Characterization of crystalline materials.
- Determination of unit cell dimensions.
- Measurement of sample purity.

Dissadvantage of XRD is the fact, that if an amorphous particles are measured as sample, there is no signal detected. Content must be then determined as a rest of crystalline part and therefore precise determination of crystalline contents is necessary.

With increasing crystallinity, sharper peaks are obtained. The width of XRD peak gives information about the size of crystallic domains (crystallites), which could be attributed to the size of particles. With increase of defects in crystal structure, the broader peaks are obtained.

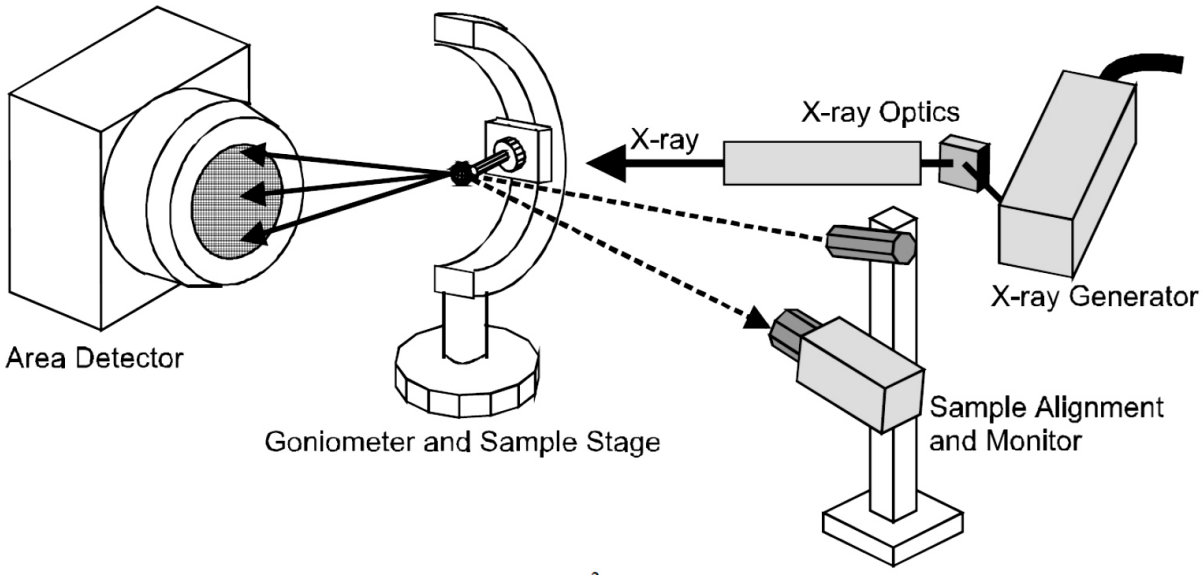

Fig. 11 XRD instrumentation [117]

Particle size of a photocatalyst is often evaluated using Scherrer's equation [118] using data of powder X-ray diffraction patterns. Disadvantage of using this equation is that it neglects the effect of crystal lattice distortion. For samples that are expected to have a large degree of distortion, use of Scherrer´s analyses is inappropriate.

$$\mathbf{d} = \frac{B\lambda}{\beta cos\theta} \tag{58}$$

In Sherrer´s equation *d* is size of the particles in direction vertical to the corresponding lattice plane, B is constant, and β is corrected full width at half maximum (FWHM) intensity of the XRD peak.

4.1.2 Ultraviolet-visible spectroscopy

Ultraviolet-visible spectroscopy (UV-VIS) is a method based on the absorption of certain portion of light from ultraviolet or visible range (from 200 to 800 nm) by transmissive samples. These samples are containing molecules with π-electrons or non-bonding electrons (n-electrons). These types of electrons are able to absorb the energy in the form of ultraviolet or visible light to be excited to higher anti-bonding molecular orbitals. The more easily excited the electrons, the longer the wavelength of light which is absorbed. [119]

UV-VIS is used in analytical chemistry for the quantitative determination of different analytes, such as transition metal ions, highly conjugated organic compounds or biological macromolecules. Mostly the measurement of solutions is done, althought Determination is usually performed in solutions, but measurement of solid samples is also possible.

In spectrophotometer, the produced light beam passes through a group of slits and mirrors, after that it slits into two beams. One of the beams is allowed to pass through a reference cuvette with solvent and the other passes through the sample cuvette, containing solvent and analyzed compound. The intensity of the light beams is then measured at a detector. Spectrophotometer equipped with an integration sphere is usually used for transmission and reflection. Instrumentation of UV-VIS measurement is given in figure 12.

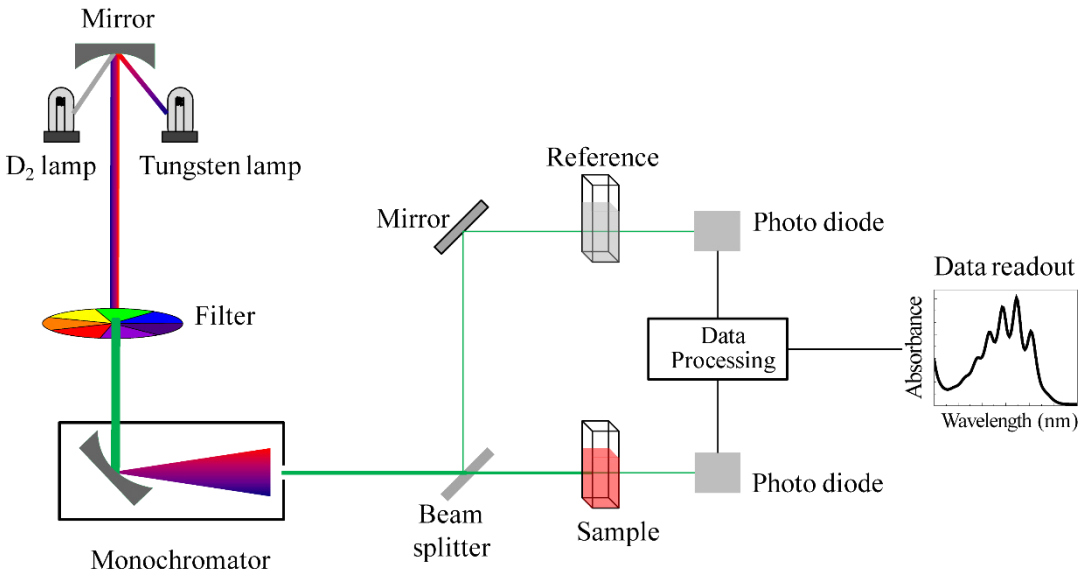

Fig 12 Instrumentation of UV-Vis spectrometry [120]

As the absorbance of light is very sensitive to plenty of compounds and in low concentration the response of absorbance is linear with increasing concentrations the degradation rate of different compounds in consequence of presence of TiO_2 can be studied by absorbance measurement and subsequently the photocatalytic activity of photocatalytic materials can be easily evaluated. Moreover, the band gap energy of prepared novel materials can be investigated by reflectance measurement.

4.1.3 Turbidimetry

This method is used for measuring the loss of intensity of transmitted light due to the scattering effect of particles suspended in solvent. Light is passed through a filter creating a light of known wavelength which is then passed through a cuvette containing a solution. A photoelectric cell collects the light which passes through the cuvette.

The decrease of light intensity is corresponding to the elastic scattering of radiation beam by suspension of colloidal particles. In Turbidimetry, the detector is placed in line with source of light beam. Very similar method is nephelometry, where the detector is placed in 90°angle towards the source of light and the scattered light intensity is measured. It is possible to measure turbidity with UV- Vis spectrophotometer. Instrumentation of Turbidimetry can be observed in figure 13.

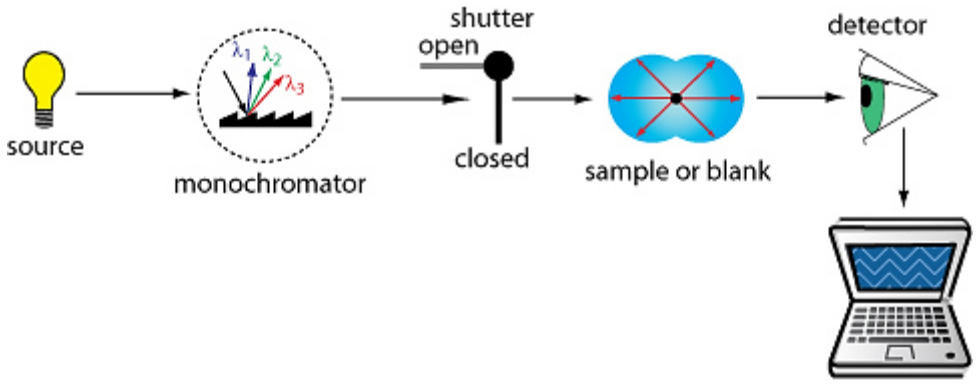

Fig. 13 Turbidimetry and nephelometry instrumentation [121]

Measurement of turbidity is not directly related to a specific number of particles and their shape. As the turbidity is defined as qualitative measurement, for the quantitative measurement, the standards and standardization methods must be used.

Interferences have impact on turbidity measurements, depending on the measured turbidimetry range. In low-turbidity ranges below 5 NTU, the interferences are caused by stray light, bubbles, ambient light and contamination. When performing high-level turbidity measurement, where the overall turbidity of solutions is greater than 5 NTU a greater impact of color, particle absorption and particle density can be observed. Upon their impact on measurement of turbidity, Interferences can be devided into two groups:

- Negative bias – these interferences cause that reported measurement is lower than actual turbidity, color of matrix, absorbing colored particles and particle density are presented by this behavior
- Positive bias – these interferences cause higher measured turbidity than the actual turbidity of solution is. Stray ligh and contamination are affecting the measurement in this way

Quite ambivalent interferences can be observed due to the measured particle size were the bias is wavelength dependent. Large particles scatter long wavelengths of light more readily than small particles, whereas small particles scatter short wavelengths of light more efficiently than long wavelengths. [122]

In order to deal with interferences, several turbidity measurements methods were developed. According to them, the standardized units of turbidity appear according to the table 6.

Tab. 6 Variation of turbidity units with used instrumentation [122]

Unit	Name	Description of Compliant Technology
NTU	Nephelometric Turbidity Unit	White light, 90 degree detection only
NTU_R	Ratio Nephelometric Turbidity Unit	White Light, 90 degree detection with additional correction detectors
FNU	Formazin Nephelometric Unit	860-nm Light (near IR) with 90 degree detection
FNU_R	Ratio Formazin Nephelometric Unit	860-nm Light (near IR) with 90 degree detection and additional interference correction detectors
FNU_{2B}	Formazine Nephelometric Unit with Dual Beam Detection Technology	4 beam IR Detection utilizing 2 light sources and two detectors.
FNU_{BS}	Formazin Nephelometric Unit using Backscatter Detection	860-nm detection angle with backscatter detector (270 – 285) degrees angle relative to the incident beam
$FAU_{XXX\text{-}nm}$	Formazin Attenuation Unit using a defined wavelength	Detection angle of 180 degrees of the incident light beam

The correct assignment of turbidity units to the recorded turbidity result is critical in understanding if interferences were addressed to same level. However, currently in most of the researchers work, the NTU unit is used for different methods of turbidity measurement. This misunderstanding impacts the traceability of the instrument technology used, thus comparison of turbidimetry measurements in different scientifical works, is of low reproducibility and requires tracking of method used for the turbidimetric evaluations.

4.1.4 Scanning electron microscopy

The scanning electron microscopy (SEM) is a method which uses a focused beam of high energy electrons to generate a variety of signals on the surface of solid specimens. These signals carry information about the sample´s surface and topography together with composition. Also the samples can be observed in various conditions: vaccum, wet conditions and wide range of cryogenic or elevated temperature.

Most common SEM mode is a detection of secondary electrons emitted by atoms excited with electron beam. Number of electrons detected is varying with specimen topography. Image of sample topography is created by collection of secondary electrons that are emitted using special detector. In general, higher the conductivity of

sample is, then better resolution can be obtained. Samples with low conductivity are either measured with lower voltage, or can be coated with carbon or metals to become more conductive. [123]

Another types of signals carried by electrons are carrying back-scattered electrons (BSE), and diffracted back scattered electrons (EBSD). BSE electrons are the most valuable for illustrating the contrast in composition of multiphase samples, EBSD electrons are valued as they can be used to form an electron backscatter diffraction image of samples, giving the information about crystallographic structures of samples. There is also X-ray generation produced by inelastic collision of the incident electrons with electrons in discrete orbitals of atoms in the sample, therefore the crystalline composition of samples can be evaluated. Instrumentation is on following figure:

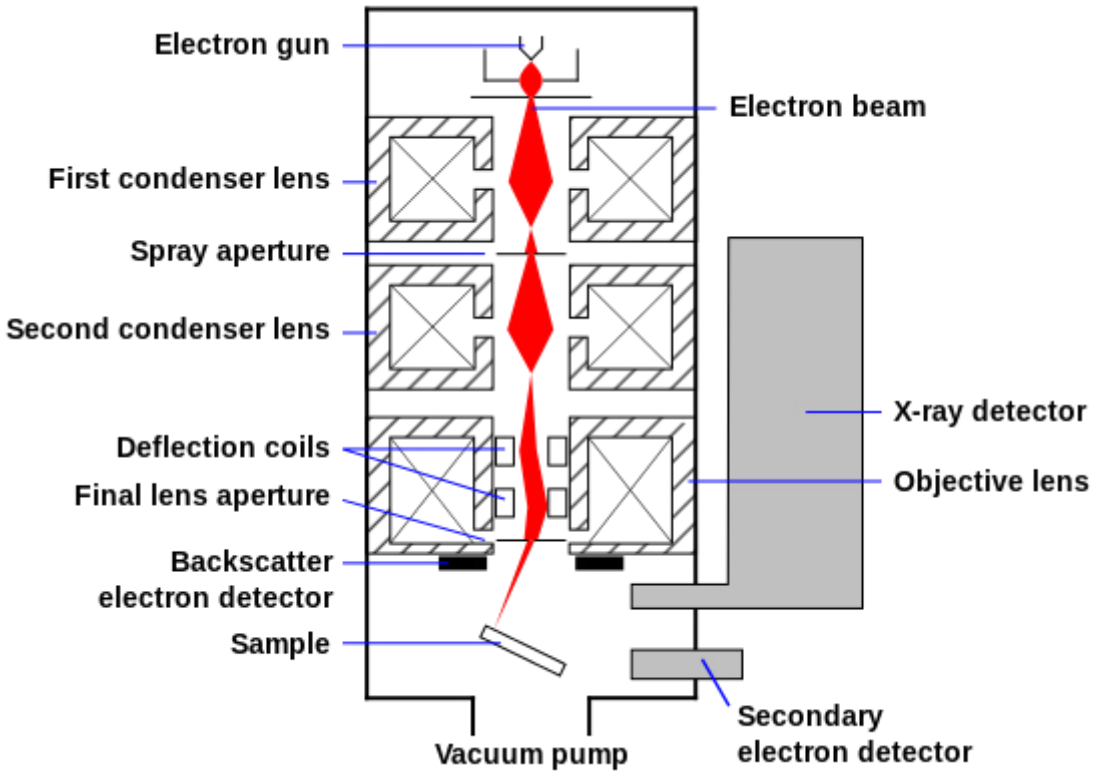

Fig. 14 Instrumentation of SEM [124]

The advantages of this method are:

- It is a non-destructive method
- X-rays generated by electron interactions do not lead to volume loss of sample
- It is possible to repeat analysis of the same materials as many times as necessary without a need for another sample preparation

Scanning electron microscopy gives the information about the surface morphology, chemical composition, crystalline structure and orientation of materials making up the sample. With a good resolution and focusation it is one of the most popular techniques for characterization of prepared novel materials. Particle size or thickness of TiO_2 layers can be studied by this method.

4.1.5 Photon correlation spectroscopy

Photon correlation spectroscopy (PCS) or dynamic light scattering (DLS) is a light scattering technique for studying the properties of suspensions and colloidal solutions. It is absolute, non-invasive and nondestructive method.

When light hits sufficiently small particles (from nanometer up to few μm scale) it scatters in all directions according to the principle of Rayleigh scattering. The light source is laser with wavelength below 250 nm. When its monochromatic and coherent light beam hits particles in solution, the scattering intensity fluctuates over the time. Fluctuation is consistent with the theory of Brownian motion as the particles measured are so small, that they are undergoing these diffusive movements. [125, 126]

The distance between the scatterers (particles) in solution is constantly changing with time. Constructive and destructive interference of scattered light by impact of surrounding particles is observed. These fine fluctuations can be analysed in the time domain by a correlation function analysis or in the frequency domain by frequency analysis. Both methods are linked by Fourier transformation.

In this forementioned fluctuation description of intensity of light measured, informations about the time scale of movement of particles is presented and diffusion coefficient of particles can be estimated. In the Stokes-Einstein theory the Brownian motion is depending on the viscosity of the suspending fluid, the temperature and the size of the particles. The particle size (its hydrodynamic diameter) can be evaluated from a measurement of the particle motion, if viscosity and temperature are known. The Stokes-Einstein equation for the determination of hydrodynamic particle diameter is presented at equation (59)

$$\boldsymbol{d_h = \frac{k_B \cdot T}{3 \cdot \pi \cdot \eta \cdot D}} \tag{59}$$

Where d_h is the hydrodynamic diameter, D is the translational diffusion coefficient obtained by correlation function analysis or frequency analysis, k_B is Boltzmann´s constant, T is absolute temperature and η is viscosity. In general, the light scattering decreases with increasing particles size.

The main disadvantage of the ordinary dynamic light scattering devices is the fact, that it is necessary that each detected photon has been scattered by the sample exactly once. Contribution of multiple scattered light leads to erroneous PCS results and misinterpretations. As a consequence, PCS requires highly diluted suspensions in order to avoid multiple scattering. The low concentration of particles makes this method sensitive to impurities in the liquid. So usually very pure liquids and a clean room environment have to be used for the preparation and the operation.

Multiple scattering interferences are causing the interpretation of measured values exceedingly difficult especially for particles with high refractive index contrasts and larger particles. Scientific research in this field leaded to the formation of cross-correlation spectroscopy. In Photon cross-correlation spectroscopy (PCCS) the idea of isolation of singly scattered light and suppression of undesired contribution of multiple scaterring is applied. As a result, high turbidity solutions can be measured. [127]

In figure 15 the instrumentation of used photon cross-correlation spectroscopy is shown. There are two laser beams with specific angle between them and it is also possible to avoid multiple scattering by moving the measurement place in cuvette in order to get less multiple scattering interference.

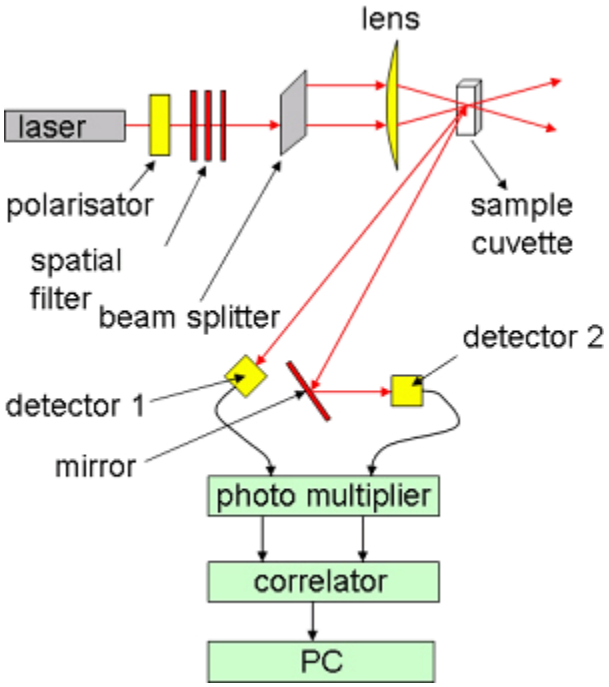

Fig. 15 The Photon cross-correlation Spectroscopy instrumentation [128]

4.1.6 TGA – DTA Analysis

Thermal gravimetric analysis (TGA) with Differential thermal analysis (DTA) belong to Thermal Analysis group of techniques.

In TGA analysis, changes in physical and chemical properties of materials are measured as a function of weight change with increasing temperature or time at constant temperature. For this technique a precission balance and programmable furnace is needed. Only characteristics of material connected with the mass loss or gain can be examined by this method. These are:

- Determination of organic content in sample
- Studies of degradation mechanisms and reaction kinetics
- Material characterization by analysis of decomposition patterns
- Inorganic content (ash) determination

TGA curve provides data about physical phenomena such as second-order phase transitions, including vaporization, absorption, adsorption, desorption, sublimation. Also chemical phenomena can be traced by TGA. These include dehydration, decomposition, oxidation/reduction reactions and chemisorptions. [129]

DTA may be defined formally as a technique for recording the difference in temperature between a substance and a reference against either time or temperature as the two specimens are subjected to identical temperature regimes in an environment heated or cooled at a controlled rate. Sampled differential temperature is then plotted against

time or temperature (DTA curve or thermogram) and endothermic and exothermic changes are detected by relation to the inert reference. [130]

DTA curve provides data on the transformations that have occurred, such as glass transitions, crystallization, melting and sublimation. The area under a DTA peak is the enthalpy change and is not affected by the heat capacity of the sample. Area under DTA peaks are corresponding to the enthalpy change and are not affected by the heat capacity of samples.

4.1.7 Infrared spectroscopy

Infrared spectroscopy (IR spectroscopy or Vibrational Spectroscopy) is kind of absorption spectroscopy. Absorption of light with wavelengths in IR range (λ = 0.7 – 350μm) is observed by this method. Samples can be presented in solid, liquid or gaseus form. The result of the measurement is the infrared spectrum recording the variation of absorption or transmittance within sampled IR wavelength range. [131]

Recorded IR spectrum is essentially a graph of infrared light absorbance/transmittance on axis *y* and frequency or wavelength on axis *x*. Frequency units used are reciprocal centimeters (cm^{-1}). Units of IR wavelength are commonly given in micrometers (μm).

Photon energies in IR spectra are not able to excite electrons, but induce vibrational excitation of covalently bonded atoms and groups. When these bonds are induced they start to stretch and bend. Energy of molecular vibration is quantized rather than continuous, this means that molecule can only stretch and ben at certain wavelength of infrared radiation. Difference in energy between the two vibrational states is equal to the energy associated with the wavelength of radiation absorbed. [131]

There are differences in absorbtion of infrared light among different molecules. This is attributed to the infrared active and inactive vibration. In general, infrared active vibrations are increasing with the polarity of the bond, for example carbonyl bond exhibits strong absorbtion due to the periodic change in dipole moment and greater polarity. Inactive infrared vibration can be sought in completely symmetrical double and triple bonds which do not result into the change of dipole moment.

Characteristical stretching and bending of structural groups of molecules can be recorded in IR spectra and permit to obtaine unique reflection of their molecular structure. Functional groups are characterized upon their vibrational absorption in IR spectra and the further deconvolution helps in revealing of the structure of organic molecules. Moreover in infrared range of 400 – 1400 cm-1, the unique pattern of absorbance peaks are revealed for every molecule. This so called fingerprint region can be compared with fingerprints of known molecules to make positive identification.

Reference measurement is always needed for estimation of IR spectra of sample. The easiest way is to put sample ambient into the one beam IR spectrometer and measure the background prior to put the analyzed sample. More effective is the use of two-beam absorbtion spectrometer. Here the beam of produced monochromatic light pass through interferometer and is split into two beams. One is passing through sample and another through reference. More accurate spectra can be collected, as the impact of fluctuation of light intensity from source in time needed for measurement is diminished. Instrumentation of two beam IR spectrometer is shown in figure 16.

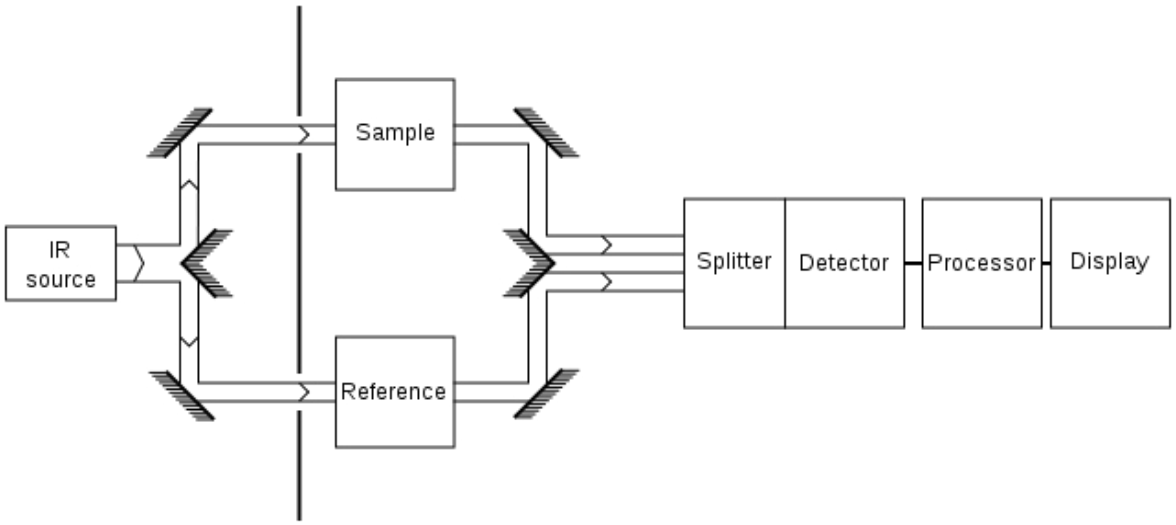

Fig. 16 Instrumentation of 2 beam IR spectrometer [132]

Special type of IR spectroscopy is Fourier transform infrared spectroscopy (FTIR spectroscopy). Michaels interferometer is used in this method. Infrared light is guided through this interferometer and then through the sample (or vice versa). A moving mirror inside the apparatus alters the distribution of infrared light that passes through the interferometer resulting in a shift of incoming IR radiation to the detector. The so called interferogram is collected and analyzed by Fourier transformation to obtain the IR spectrum of sample.

FTIR spectroscopy provides better resolution of IR spectra recorded, better wavelength calibration, higher signal to noise ratio and Fellgett´s advantage resulting from simultaneously collected wavelengths information leading to further reduction of noise ratio. [131]

4.1.8 BET analysis

Based on Brunauer–Emmett–Teller (BET) theory [133] which aims to explain the physical adsorption of gas molecules on a solid surface, this analysis is used for the estimation of surface area and pore size distribution of solid materials using gas adsorption. The BET theory refers to multi layer adsorption, and usually works with non-corrosive gases (nitrogen, argon, carbon dioxide) as adsorbates. BET adsorption isotherm equation is presented in equation 60. [134]

$$\frac{1}{\left[V_a\left(\frac{P_0}{P}-1\right)\right]} = \frac{C-1}{V_m C}\cdot\frac{P}{P_0}+\frac{1}{V_m C} \tag{60}$$

Where *P* is partial vapor pressure of adsorbate gas in equilibrium with the surface at 77.4 K in pascals, P_0 is saturated pressure of adsorbate gas, V_a is volume of gas adsorbed at standart temperature and pressure in millilitres, V_m is volume of gas adsorbed at standart temperature and pressure to produce apparent monolayer on the sample surface, C is constant related to the enthalpy of adsorption of adsorbate gas on the powder sample.

V_a is measured in multipoint assessment for not less than 3 values of P/P_0 and this value is plotted against the P/Po in BET measurement. The units in BET analysis are $m^2 \cdot g^{-1}$. Instrumentation of BET analysis is demonstrated in figure 17.

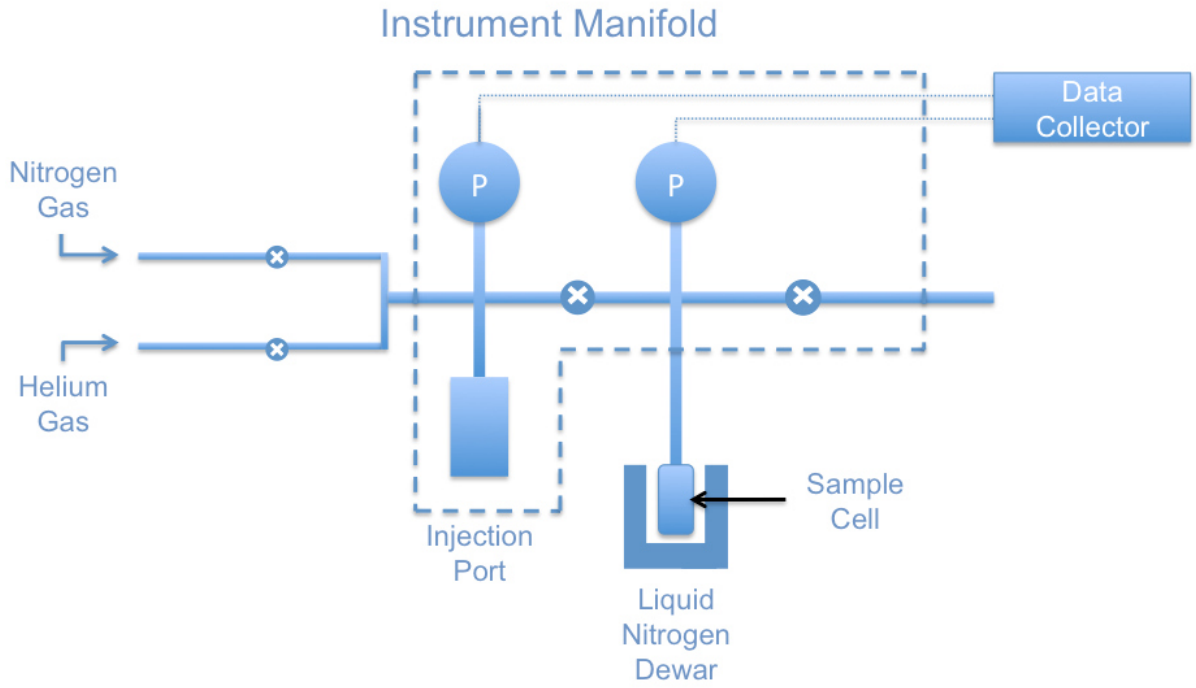

Fig. 17 Instrumentation of BET measurement [134]

When using BET analysis for estimation of the surface area of solid material, the following criteria must be considered:

- Adsorption occur only on well-deifined sites of sample surface (one per molecule)
- Molecule acts as single adsorption siter for a molecule of the upper layer
- The final presented molecule layer of adsorbed gass is in equilibrium with the gass phase having similar molecule adsorption and desorption rates
- Desorption is kinetically-limited process, therefore same heat of adsorption must be provided for desorption
- At the saturation pressure, the molecule layer number tends to infinity and is equivalent to the sample surrounded by liquid phase

Prior to the measurement of BET specific surface area, outgassing pretreatment procedure is necessary for sample in order to remove vapors that may be physically adsorbed onto the surface of material after manufacture, handling or storage. This part of sample pretreatment is crucial for valid BET measurement.

Outgassing conditions must be selected with sufficient accuration that the original surface of material is reproduced as closely as possible. Outgassing procedure include applying vacuum, temperature and time variation, purging of sample in inert dry gas (helium), or desorption-adsorption cycling method.

Usually dead volume is measured on deggased sample by inert non-adsorbed gas, such as helium before the saturation pressure measurement with nitrogen at temperature of 77.4 K is carried out to get lowest desired relative pressure. For multipoint analysis measurement of nitrogen volume adsorbed is done at different P/P_0 values. Using nitrogen, commonly saturation adsorption values are measured, with rate of P/P_0 = 0.10, 0. 20, 0.30. [134]

4.1.9 Magnetization measurement

Most common system for measurement of magnetic properties is Vibrating Sample Magnetometer (VSM) used for measure of magnetic properties of materials as a function of magnetic field, temperature and time. Powders, solids or liquids can be measured by this system. [135, 136]

Principle of measurement is the interaction of material placed in uniform magnetic field (H), which leads to the formation of magnetic moment (M) in studied magnetically sensitive sample. Typically, sample is place into the sensing coil, and undergoes sinusoidal motion as mechanical vibration. Magnetic flux changes induce a voltage in sensing coil proportional to the magnetic moment of the sample. Variable temperatures are applied to the sample as well. [135, 136]

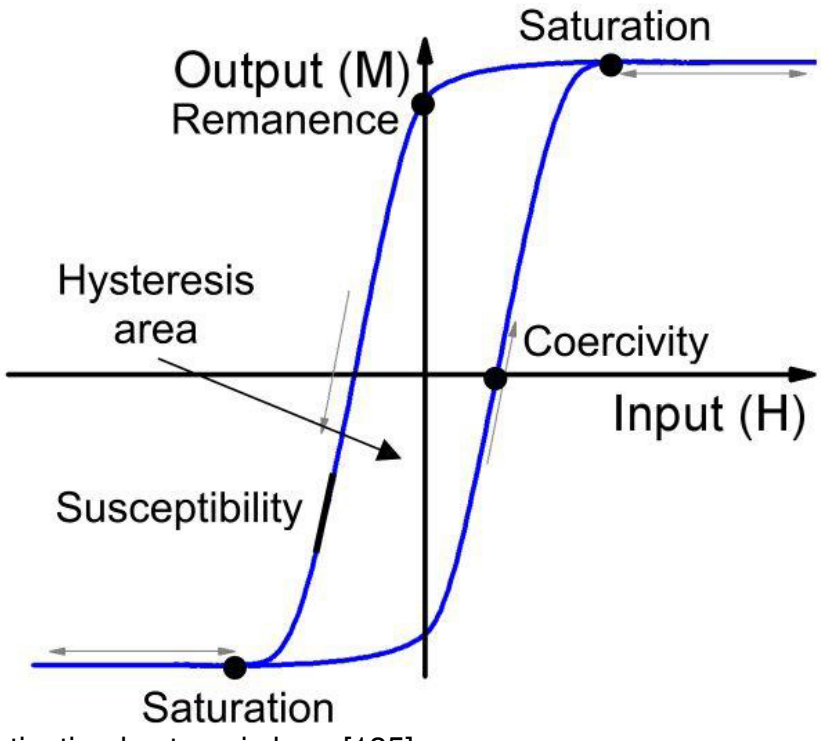

Fig. 18 Magnetization hysteresis loop [135]

From magnetization hysteresis loop the following magnetic properties are obtained:

- M_s – saturation magnetization
- M_r – magnetization remanence
- H_c – coercivity
- SQR – squareness ratio (slope of Hc)
- μ – magnetic permeability (M/H)

Saturation magnetization is defined as a point in hysteresis loop, where H cannot increase the magnetization of material any further and it is corresponding to the maximal magnetic permeability. Coercivity is very formaly considered as the field required to reduce the magnetization to zero after saturation, though in physical meaning it is very complicated parameter. Depending on the magnetization process, H_c may be the nucleation field, domain wall coercive field, etc. Unit of magnetization is emu·cm^{-3} corresponding to A·m^{-1} (ampere-turn per meter). [135, 136]

4.1.10 Conductivity and pH measurement

Conductivity and pH measurements techniques belongs to the electroanalytical methods. These techniques study an analyte by measuring the potential and current in electrochemical cell containing analyte. [137]

4.1.10.1 Conductivity measurement

Conductivity or specific conductance is a measure of how well a solution conducts electricity. Absolutely pure water conduction is very poor and increases with the dissoluted salts and impurities in water. Therefore the conductivity is sometimes directly linked to the total dissolved solids (TDS).

In measurement of conductivity, the resistance between two flat or cylindrical electrodes separated by fixed distance is determined. In order to avoid electrolysis, the alternating voltage mode is used. Calibration of method is done by solutions of known specific resistance. Conductivity is likewise pH measurement temperature-dependent analysis.The unit of conductivity is Siemens per meter (S·m^{-1}). [137]

4.1.10.2 Measurement of pH

Measurement of pH belongs to the group of electroanalytical potentiometric techniques, where a potential of a solution between electrodes is measured. There are two electrodes presented in pH measurement. Reference electrode has constant potential, while indicator electrode´s potential changes with the composition of sample. As reference electrodes in pH measurement silver chloride electrode and calomel electrode are commonly used. For indicator electrode, the hydrogen standard or standard glass electrode is used. Both electrodes are regularly combined together presenting one device.

Definiton of pH can be explained as the hydrogen ion activity in liquidous environment formed by dissociation of water. Activity is corresponding to the hydrogen ion concentration which can be written as equilibrium concentration of oxonium ions H_3O^+ in solution at given temperature. The value of pH is evaluated according to the equation 61.

$$pH = -\log [H_3O^+] \quad (61)$$

As the electrodes do not give same signal over their service life, it is necessary to calibrate them with pH buffer solutions (usually borate buffers). Standard pH value of pure water at temperature of 25°C is 7. Measurement of pH is temperature dependent, with increasing temperature the pH decreases. This phenomena is caused by the increasing concentration of H_3O^+ ions as the dissociative reaction of water is endothermic process.

Another possibility of measurement of pH is the evaluation of dye change absorbances in the visible range of wavelength spectra. For example, methyl orange and phenolphthalein are capable to slightly shift their conformation with increasing or decreasing concentrations of hydrogen ions in liquidous media. [137]

4.1.11 XPS measurement

X-Ray photoelectron spectroscopy (XPS) known also as Electron Spectroscopy for Chemical Analysis (ESCA) is a method used for quantitative and qualitative measurement of surfaces. Principle is measuring the photoemission of the solid samples after the the interaction of X-Rays with energy range 300 – 1000 eV with the surface depth of 0 – 12 nm. Kinetic energy of photoemitted electrons is plotted against the number of detected electrons. To obtain minimum error, UHV vacuum is needed in this method as the detectors of photoemitted electrons are typically placed in one meter distance from the analyzed sample. [138]

Because the wavelength and energy of X-ray hitting surface is known, the binding energy of emmited electrons can be estimated using the Ernest Rutherford based equation.

$$E_{binding} = E_{photon} - (E_{kinetic} + \phi) \quad (62)$$

Where $E_{binding}$ is binding energy of electron, E_{photon} stands for the energy of X-ray radiation, $E_{kinetic}$ is kinetic energy of electron measured by by XPS instrument and ϕ is called work function. It is constant adjustable instrumental correction factor that accounts for the few eV of kinetic energy fiven up by the photoelectron when absorbed by the instrument detector.

Each element produces a characteristic set of XPS peaks at characteristic binding energy values that directly identify each element that exists in or on the surface of analyzed sample. Spectral peaks are reflecting the electron configuration of the electrons within atoms. Ammount of element in sampled area is corresponding to the number of detected electrons. In practice, all elements expect hydrogen and helium ($Z<3$) can be detected with sufficient detection limit range from 1 ppt to 1 ppm. XPS is used for the analysis of:

- Element composition of the surface.
- Empirical formula of pure materials.
- Chemical or electronic state of elements on the surface.
- Uniformity in surface profile of sample.
- Uniformity in depth profile of sample.
- Thickness of layered materials and composition detection measurement.

XPS is non-destructive technique for surface chemistry of almost any material, however, non-dry, outgassing, radioactive or highly magnetic materials are challenging for this analysis. [138]

4.2 Hydrolysis of Titanium alkoxides

For measurement of kinetics of Ti-alkoxide hydrolysis in neutral conditions, three kinds of Ti alkoxides were used titanium tetraethoxide (TIETH), titanium tetreaisopropoxide (TIPP) and Titanium tetreabutoxide (TIBUT), with increasing molar ratio of Ti-alkoxide / water (*R*) in order to observe the change in kinetics rates. *R* was set to 0.5; 1; 2; 4; 8; 16. Same amount of Ti-alkoxides was used in each hydrolysis measurements.

For hydrolysis the approximately 2.000 g of alkoxide was used dispersed in 2.000 g of solvent (ethanol, isopropanol, 1-butanol). Calculated amount of water was mixed with the 5.000 g of solvent and upon vigorous stirring accomplished by test tube mixer was added through syringe to the previously prepared alkoxide solution placed in turbidimeter cuvette. After adding all solvent solution with water into the solution of Ti-alkoxide with solvent, formed solutions were mixed for further ten seconds and then were placed directly to the turbidimeter and measurement of turbidity started. Hydrolysis was done in turbidimetric cuvette with septa and solvents and other chemicals were carefully added with syringe to prevent any possible impact of air humidity on the alkoxides samples.

4.2.1 Kinetic study

Kinetics of hydrolysis were estimated with turbidimetry measurement with 2100Q HACH´s portable turbidimeter as rate of development of white turbid solution which is corresponding to the information mentioned in chapter 3.7.2. The induction time was estimated for selected mixtures of Ti-alkoxides with increasing temperatures of 25, 35, and 45 °C. For heating of the mixtures, the heater with oil bath was used.

4.2.2 DTA – TGA analysis

Prepared samples of Ti-alkoxide hydrolysates were analysed with SDT Q 600 (TA Instruments) DTA – TGA analysis in order to observe changes of appearance of crystallization peak with different *R* values and to check the observed changes in remainance of rests of solvents in hydrolysates. Typically, after preparation of Ti hydrolysates, the evaporation of solvent was done using the laboratory heater at 60 °C for 60 min. After that, samples were left to cool down to ambient temperature and DTA – TGA analysis was performed.

For selected *R* in each Ti-alkoxide hydrolysis synthesis also the evolved gas analysis (EGA) was performed on the samples in order to observe infrared (IR) absorbance spectra of background when the crystalisation begun and during the DTA – TGA analysis. The overall intensity of IR absorbance spectra in range 4000 – 400 cm^{-1} with increasing time was plotted in Gram-Schmidt analysis. This analysis was used to project the major changes during the EGA measurement of DTA – TGA analysis. Further 2D IR EGA projection of development of IR spectra of EGA sampled gass evolution during DTA – TGA analysis was done.

4.2.3 BET analysis

BET analysis was done on prepared samples by NOVA e 2000 specific surface analyser to obtain the specific surface comparison for lowest and highest *R* of each Ti-alkoxide hydrolysate analysed. The hydrolysates of Ti-alkoxides were sintered at atmospheric conditions in crucible with temperature ramp 5°C·min-1 until reaching 450 °C and threshold of 120 min at this temperature was applied. After this treatment, samples were left to cool down in crucible and were analysed. Outgassing of samples was done at 150 °C for 5 – 15 hours and the adsorption of nitrogen was evaluated at temperature of 77.350 K. Multipoint analysis of nitrogen adsorbed was done for at least five P/P_0 values for each measured sample and specific surface S_{BET} was obtained from the plot of the BET equation as mentioned in chapter 4. 1. 8.

4.2.4 XRD analysis

In order to verify the formation of anatase during DTA – TGA measurement, the XRD analysis was performed on DTA – TGA treated samples. XRD of prepared samples was done using PAN ANALYTICAL X-Ray Difractometer with PIXcel3d detector. Cu anode was used with 40 kV voltage. Also the high temperature cell for measurement of XRD was used in order to observe the development of crystallites and identify them for selected *R* of Ti-alkoxides hydrolysates. XRD spectra was recorded every 10 minutes in temperature chamber with increasing temperature from 250 to 490 °C with increasing temperature steps of 20°C. Results of Scherer´s equation calculated crystallite size of anatase phase for selected *R* of Ti-alkoxides with increasing temperature were calculated.

4.2.5 SEM – EDS analysis

To verify, if any change of surface morphology or composition of sample was presented between hydrolysed and sintered samples during DTA – TGA analysis of Ti-alkoxides the measurement of surface by SEM with EDS analysis was performed. Selected hydrolysed samples of Ti-alkoxides surface were captured with SEM and EDS analysis was performed on them. For EDS measurement, the scanning mode of surface was administrated to sample as large area as possible in order to mitigate impurities. After scanning of the surface of hydrolyzed samples, the heat treatment was administered in order to obtain crystallic phases. Samples were put into the crucible with atmospheric conditions and heat treated for 120 minutes at 450 °C with temperature ramp of 5 $°C \cdot min^{-1}$.

4.2.6 PCCS analysis

For estimation of size of particles, the photon cross correlation spectroscopy was used, using spectrometer NANOPHOX. In PCCS analysis run on the SYMPATEC NANOPHOX equipement selected samples of Ti-alkoxides hydrolysed and sintered at 450°C for 120 min were analysed with varying *R*.

AUTO NNLS function of SYMPATEC NANOPHOX was applied for the measurement with fully automatic adjusting of sample for analysis. Samples were dispergated in destilled water supporting the dispergation by ultrasonic bath for 5 minutes, each sample. After that, samples were put in measurement cuvvettes and were analysed.

Size distribution spectra was collected for 180 s and for each sample, 5 measurements were done and average value of size was estimated. The median diameter (D_{50}) which is a quantile, dividing the size distribution by number of particles expressed as intensity of scattering, into the two same areas under the quantitative distribution of particle size is reported for all measurements of particle size by PCCS.

4.3 Synthesis of magnetic nanoparticles

In powder catalysis, magnetic iron oxide particles play important role as suitable holder for coatings and preparation of core-shell structured novel materials. With high magnetization, the Fe_3O_4 nanoparticles of magnetite are among maghemite γ-Fe_2O_3 and hematite α-Fe_2O_3 one of desired particles for further work up. There are plenty of ways, how to prepare magnetic iron oxide particles including wet chemical process, hydrolysis, solvothermal synthesis and others as mentioned earlier in theoretical part of thesis.

Herein we discuss simple one-step precipitation method for pure magnetite production from solution of Mohr´s salt $(NH_4)_2Fe(SO_4)_2{\cdot}6H_2O$. As bases NaOH and Na_2CO_3 were used for the precipitation with no further adjustement of ratios of Fe^{2+} and Fe^{3+} salts. As it was concluded in few studies, the possible formation of magnetite can be accomplished using only ferrous salts as the starting compound for precipitation. Moreover control over the particles morphology can be observed varying the temperature of reaction. [138 - 141]

The polycarboxylic superplasticizer Glenium ACE 40 is used during synthesis in order to treat surface of nanoparticles with carbon layer in further coating process by TiO_2 nanoparticles and for the reduction of agglomeration of particles during the precipitation. Polycarboxylic superplasticizers (PCE) are used in the concrete mixtures preparation for the advantage of reducing the needed water – cement ratio for enhaneced manipulation with cement mixtures. Althought the intensive research explaining their function is recently carried out, their working principles lack of a full understanding. It can be assumed that in general their ability is to interact with the surfaces of hydrating particles and reducing the viscosity of such solutions.

Used type of polycarboxylic plasticizers is composed from side chain represented by methoxy-polyethylene glycol copolymer grafted with the main chaing composed of methacrylic acid copolymer. Carboxylate group in water dissociates whereas providing negative charge to the backbone of superplasticizer. This leads to the interaction of backbone with positively charged colloidal particles. Surface of particles remains its reactivity for further hydrolysis reaction and the stabilization and better dispergation of particles is observed when using PCE. Another conclusions of several works include the idea that the PCE has a lubricating effect between adjacent particles and PCE increases surface wettability.

In present thesis, the application of PCE is done by applying certain amount of PCE into the precipitated solution in order to get more dispergated particles by repulsive forces of adsorbed PCE´s backbones and therefore to reduce their size of agglomerates. Also the formation of carbon layer on surface of magnetite would be

beneficial as decreasing the electron – hole recombination rate due to the mitigation of the back electron transfer. [140, 141]

4.3.1 Synthetic procedure

Precipitation of nanoparticles was done according to method, developed in earlier work of Author of thesis. [142] Stock solution of Mohric salt was prepared with concentration of 0.030 mol·dm^{-3}. The yellow to orange colored solution was stabilized adding droplets of sulfuric acid to reach pH ≤ 3 resulting in transparent colorless solution. Stock solutions of bases were prepared with concentration of 0.1 mol·dm^{-3}.

Furthermore the apparatus consisting of three necked flask with thermometer, heater and bubble cooler has been used as shown in figure 30 for measurements of pH and conductivity upon increasing amount of base added and the temperature impact on the rate of precipitation and appearance of magnetic particles was evaluated while varying the temperature of precipitation reaction. For measurement at 0°C the Dewar container with ice water was used. The glass stirrer was used for all temperatures except when performing the reaction in boiling solution. In this case, the benefit of self mixing of boiling solution was used. Also the cooler was not used when performing the reaction in Dewar container at 0°C and laboratory temperature 22 °C.

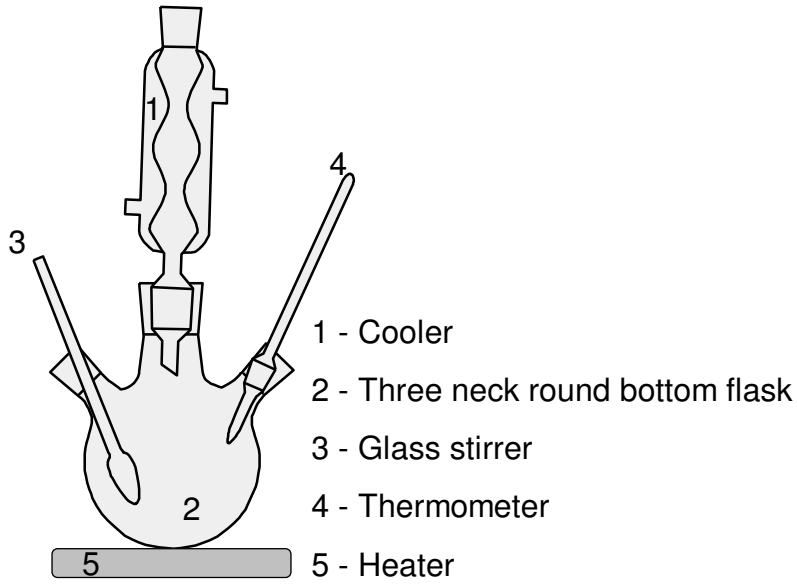

Fig. 30 Apparatus for the magnetic nanoparticles preparation

4.3.1.1 Reaction Mechanism

Reaction of precipitation of ferrous and ferric salts in optimal ratio for Fe_3O_4 was explained earlier in chapter 3.8.1. When precipitating only ferrous salts, different mechanisms of formation of Fe_3O_4 can be observed. It is supposing the reaction of oxygen with previously formed $Fe(OH)_2$ leading to the formation of FeOOH as shown in equation 63.

This specie is then undergoing the same reaction as in coprecipitation reactions and final formation of Fe_3O_4 is accomplished as mentioned in equation 55 earlier in chapter 3.8.1. [139,143]

$$4\ Fe(OH)_2 + O_2 \rightarrow 4\ FeOOH + 2\ H_2O \quad (63)$$

In fact, the reaction and formation of solid phases is extremely different and ferrous polycationic species are poorly documented. It is known fact that condensation of ferrous species occurs in pH > 6 – 7. Formation of solid phase is explained as the absence of strongly complexing ligands at certain range of pH leads to the formation of the aquo, hydroxo zero-charge complex, which is the precursor of solid. Hydroxylation of such complex leads to the precipitation of hydroxide $Fe(OH)_2$. In solid state or aqueous suspension, the ferrous phases are very sensitive to oxidation. Various phases (green rusts, magnetite, goethite, lepidocrocite) can be formed depending on the conditions. Although ferric hydroxide $Fe(OH)_3$ is reported as intermediate during precipitation of ferrous salts in work of Šutka and co-workers [139] its presence or formation was never proved nor identified as concluded in work of Jolivet and co-workers. [143]

4.3.1.2 Temperature impact on precipitation of magnetite particles

In typical procedure for measurement, 100 ml of stock solution of Mohr´s salt with concentration of 0.030 $mol \cdot dm^{-3}$ and 150 ml of base (NaOH) solution with concentration of 0.1 $mol \cdot dm^{-3}$ were used so that the pH mixed solution was in range of 9 - 11. Solutions were preheated and tempered at given temperature for 20 minutes and after that were mixed together vigorously in apparatus and sampling for measurement of XRD begun. Samples were withdrawn and placed on the evaporating disc just before the start of measurement with XRD at dried air temperature.

For evaluation of temperature impact on precipitation the measurement on the XRD PAN ANALYTICAL X-Ray Difractometer with PIXcel3d detector. Cu anode was used with 40 kV voltage. The samples were withdrawn from apparatus and with magnet the magnetically active particles were attracted. Measurement of XRD was performed in 10 minutes scans every 20 minutes.

Analysis of prepared particles at different temperatures was also done using SEM measurement by JEOL JSM-7600F microscope. Preparation of samples was done by washing the particles few times with distilled water and leaving them to dry on air at laboratory conditions. After that, particles were put on the sticking carbon foil for analysis to prevent any damage to microscope by revealing the particles from surface by magnetic forces presented in microscope during analysis.

4.3.2 Measurement of pH and conductivity

For characterizing the formation of magnetite, the procedure with 100°C boiling solution of Mohr´s salt was used as described in Author´s paper Preparation and TiO_2 coating of Nanosized magnetic particles [144]. In each experiment, approximately 150 ml of stock solution of Mohr´s salt were added to three necked flask. After that, the flask was closed and heater and cooler were turned on. When heated solution started to boil, solution of base with increasing volume range of 2.5 – 10 ml were added step-wisely.

After each step, the solution in flask was left to boil for approximately 7 minutes and then 15 ml sample was collected and immediately, cooled down to 25°C. Conductivity

and pH were measured and sample was returned back into the reaction mixture. Gradient volume of base addition was selected after several initial measurements to obtain better resolution of experimental data. The starting volume was 2.5 ml until total of 25 ml of base were added, continuing with adding 50 ml of base in 5 ml steps and finishing with adding 10 ml of base at final steps. Base were added untill the conductivity started to raise as the influence of the increasing concentration of OH^- ions.

The high temperature was selected to drive the kinetics of ongoing precipitation processes in solution into the steady state after the addition of base as soon as possible. In fact, for each addition of base, the time of 14 minutes was left to get the precipitates and other reactions happening in solution into the equal state. When applying the ACE 40 for coating the 2.00 g of it were introduced into the Mohr´s salt solution at the beginning of the precipitation.

With neodymium magnet, each sample withdrawn for the conductivity and pH measurement was tested if precipitates were performing any magnetic properties. If so, the preconcentration of such magnetically active precipitates was done with magnetic force and samples were collected for later SEM and XRD measurements and were washed several times with water and placed on the carbon tape. Very first appeared magnetically active precipitates were collected and after that, the samples of magnetic particles formed when the pH > 9 and conductivity measurement was showing lowest conductivity of reacting solution.

4.3.3 Characterisation of prepared nanoparticles and impact of superplasticizer

XRD and SEM - EDS measurements were performed for collected magnetic particles as mentioned in conductivity and pH measurement. Preparation of samples for these analysis included washing of particles in distilled water for several times and then drying in the air atmosphere. In order to verify the presence of superplasticizer on surface of magnetic particles, the DTA – TGA analysis was performed in dried air atmosphere for samples of NaOH base and NaOH base with ACE 40 content. Heat ramp was 10 °C·min^{-1} until reaching 800 °C. The PCCS analysis was performed on samples of nanoparticles collected at lowest conductivity reported. Also the magnetization measurement was done using the LAKE SHORE 74707 VSM (Vibrating Sample Magnetometer) on prepared samples precipitated without and with presence of superplasticizer.

4.4 TiO_2 application on magnetic particles and photocatalytic studies

4.4.1 Deposition of TiO_2 on the surface of magnetite nanoparticles

Recently, the methods for the deposition of TiO_2 on the surfaces of various particles were developed concerning the application of nanosized TiO_2 particles directly to the surface of nanomagnetic particles even during the precipitation synthesis. [105] Taking into account the possible loss of magnetic properties when heat – treating the surface coating done by particles and in order to obtain high surface area of particles, the

deposition technique consisted from the applying of previously crystallized TiO_2 particles of anatase with and without treatment by TIPP hydrolysis coating was done.

In typical procedure, the 0.200 g of magnetic nanoparticles as prepared in chapter 5.2 using 100°C boiling solution for quick precipitation with final pH range of 9 – 10 were used. These were dispersed in 10.00 g of isopropanol by using ultrasonification bath for 10 minutes. Then the particles of selected TiO_2 in amount of 0.4 g was put into this solution and ultrasonified for further 10 minutes. Then the evaporation of solvent was done at 50 °C for 60 min and particles were heat-treated at 150°C in crucible with heat ramp 10 °C ·min^{-1} and threshold of 120 min. After that particles were dispergated in distilled water and separated by magnetic forces for several times in order to get rid of the TiO_2 particles alone.

The method using TIPP hydrolysis with low $R = 2$ was used for treatment of the surface of TiO_2 nanoparticles applied to the surface of nanomagnetite as the appearance of turbidity could be observed when dispergating the core-shell particles done just by agglomeration and low temperature treatment at 150 °C. In this case, the particles were prepared with same procedure as mentioned earlier with a difference, that 0.200g of adjusted TIPP R = 2 was used to be dispergated in the isopropanol as a first step of core-shell coating. Also the heat treatment was done at elevated temperature with ramp 5 °C ·min-1 reaching 370°C with threshold of 120 min in Nitrogen atmosphere in order to crystallize the anatase particles as reported in chapter 5. 1.

4.4.1.1 Characterization of TiO_2 application on the surface of magnetite nanoparticles

Analysis of prepared particles were done with XRD PAN ANALYTICAL X-Ray Difractometer. JEOL JSM-7600F SEM – EDS and magnetization of particles was measured and also the remaining turbidity measurement with 2100Q HACH´s portable turbidimeter after their dispergation in ultrasonic bath for 30 min and magnetic collection to observe proportional releasement of TiO_2 nanoparticles into the aquatic environment. In typical remanence turbidimetry measurement, the 0.2 g of particles was dissolved in 50 ml by ultrasonification for 30 minutes and then the turbid solution was put into the beaker and magnet was placed on the side of the beaker. After 60 s the solution for turbidity measurement was withdrawn from the opposite side of beaker.

For selected particles, band gap measurement was done with UV – 2600 SHIMADZU UV-Vis-NIR Spectroscopy spectrometer with diffuse reflectance measurement mode. Reflectance ($R_{\%}$) was recorded in range of 200 – 1200 nm and was transformed according to the Kubelka – Munk Theory. [145] The Kubelka´s constant (K) was received as demonstrated in following equation:

$$\boldsymbol{K = \frac{(1-R_{\%})^2}{2 \cdot R_{\%}}} \tag{64}$$

and was plotted as $(K^*hv)^{1/2}$ $(eV)^{1/2}$ against hv (eV). Also XPS measurement was done using the AXIS ULTRA X-ray Photoelectron Spectroscopy system in order to verify the chemical surface states of Ti, C and Fe.

4.4.2 Deposition of TiO_2 on the surface of the Mn-Zn ferrite

Mn-Zn ferrite was used as supplied from industry as interesting compound for core-shell microscopic particles synthetized in large scale production. Benefits of using this material as starting are narrow size distribution with D_{50} = 126 μm, no change of magnetization upon heat treatment of applied TiO_2 surfaces and also sometimes reported synergistic photocatalytic effect that produces enhanced photocatalytic activity as the ferrites have photocatalytic activity under visible light. [146]

The deposition of the TiO_2 particles on surface of ferrite was done using the procedure as done in Author´s paper TiO_2 surface coating of Mn-Zn dopped ferrites study. [147]

In each procedure, the amount of TIPP was set to be equivalent to 1.0 g of pure T_IO_2 content and was mixed with 10 ml of Isopropanol together with 5.0 g of Mn-Zn ferrite particles. The mixture was left mixing with glass stirrer for 60 minutes at room temperature, then the temperature was increased to 80°C to dry the solvent and after that formed particles were put into the crucible with temperature set to increment of 2 °C per minute up to 350 °C and threshold of 4.5 hours.

Also the intent to prepare the mesoporous surface was done, using the PK 20 PRETIOX anatase nanoparticles from large scale industry producer PRECHEZA, with average size diameter D_{50} = 15 – 35 nm and surface area S_{BET} = 70 – 110 $m^2 \cdot g^{-1}$. For procedure to produce the mesoporous surface with high specific surface area the 0.5 g of PK 20 particles were used and introduced into the TIPP solution with isopropanol followed by 10 min ultrasonification before the ferrite introduction.

The impact of Au and C coating of surface of ferrite was also studied. For applying the C and Au coating onto the surface of ferrite, the Polaron SC7640 Sputter Coater was used with Au/Pd cathode when applying Au coating and Tesla BS349 Carbon Sputter coater was used for applying of C layer. SEM-EDS measurements and XRD analysis were used for characterization of prepared products. Layers of C and Au were introduced on the ferrite surface by repeating at least 10 sputter coater sequences on 5.0 g of ferrite material and after that the surface was analyzed with scanning electron microscopy using ZEISS EVO LS 10 and JEOL JSM-7600F microscopes. After that, the prepared material was used in the procedure as described above.

4.4.3 Photocatalytic decomposition of methylene blue

For decomposition of methylene blue in solution, TiO_2 coated core-shell magnetic nanoparticles were identified in chapter 4.4.1 after the analysis. The decomposition of methylene blue was done using mixing photocatalytic decomposition method adapted for the powder photocatalytic activity estimation as defined in doctoral thesis of Svava Daviðsdóttir. [148]

The photocatalytic activity was measured with decomposition of methylene blue, where standard DIN 52980 [149] was adapted from measuring photocatalytic activity of films to powders. 2 beakers with 50 mL aqueous suspension of 10 μM of methylene blue and 1 mg photocatalyst were stirred in dark for 2 hours to get desorption-adsorption equilibrium. When the equilibrium was achieved one of the beaker was exposed to UV-light of 365 nm with intensity of 3.47 $W \cdot m^{-2}$ and another was kept in dark as controller. A stirrer was used in the suspension for continuously

mixing. The temperature of the suspension was 23°C. Every 20 minutes 2-3 ml was collected and centrifuge at 5 000 rpm for 3 minutes for removing the particles and obtain clear solution for the UV-VIS analysis. The upper clear solutions was analysed recording spectra 750 – 550 nm with UV- 2600 SHIMADZU UV-VIS-NIR Spectrometer. Both the sample particles and the solutions were added back to the beakers after measurement in each step and measurement continued.

4.4.4 Photocatalytic activity of Mn-Zn ferrite determination

Photocatalytic activity of selected prepared TiO_2 coated Mn-Zn Ferrite is evaluated upon decomposition of methylene blue and isopropanolic and ethanolic vapors for Mn-Zn ferrite in experimental chemical reactor with magnetically holded powdered photocatalysator beds. The device was constructed by Ptacek and co-workers [150] as a device intended for the processes of heterogeneous catalysis, for the disposal of hazardous and toxic substances and cleaning of effluent gas before discharge to atmosphere, for example in afterburner technology. This device was connected with the Thermo Nicolet IS 10 FTIR spectrometer in a closed loop with ethanolic or isopropanolic vapors. Basic scheme is shown in figure 31.

In reactor the ferrite was magnetically holded inside of the silica tube. In typical procedure, the pump was turned on and FTIR baseline was recorded, after that, valve to the flask with ethanol or isopropanol was opened and system was left for 5 minutes to equilibrate the signal, then the valve was closed and the UV lamp was turned on. For typical measurement of photocatalytic activity, the 20 g of prepared powder photocatalysater was used.

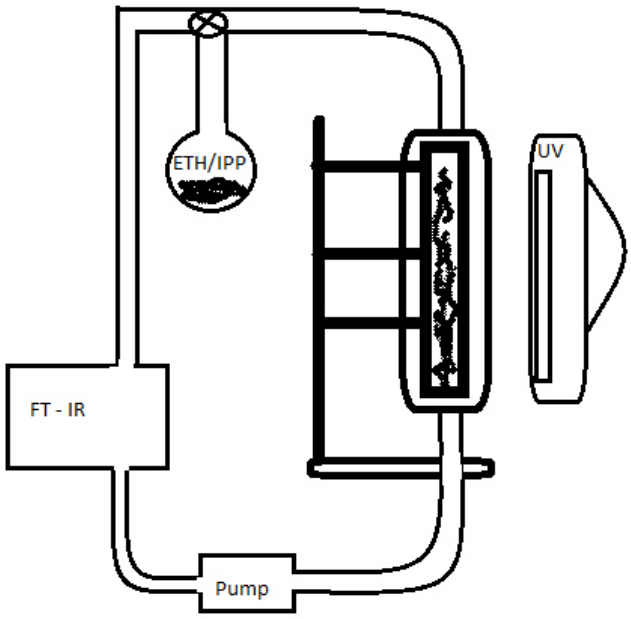

Fig. 31 Apparatus for the Mn- Zn ferrite photocatalytic decomposition of solvent vapors

4.5 Used Chemicals and equipments

4.5.1 Used Chemicals

Reactants for Ti – alkoxides hydrolysis:

- Titanium ethoxide, 97.5% purity, Sigma Aldrich, CAS: 3087-36-3
- Titanium isopropoxide 97.5% purity, Sigma Aldrich, CAS: 546-68-9
- Titanium butoxide 97.5% purity, Sigma Aldrich, CAS: 5593-70-4
- Ethanol p.a. Sigma Aldrich, CAS: 64-17-5
- Isopropanol p.a., CAS: 67-63-0
- Butan-1ol, p.a. CAS: 71-36-3

Reactants for magnetite preparation:

- Mohr´s salt p.a. CAS: 7783-85-9
- Sulphuric acid (p.a.), Lachema, CAS: 7664-93-9
- Sodium Hydroxide p. a. Lachema, CAS: 1310-73-2
- Sodium Carbonate p. a. Lachema, CAS: 497-19-8
- Master Glenium ACE 40, BASF

Photocatalytic testing:

- Isopropanol p. a., CAS: 67-63-0
- Ethanol p. a., CAS: 64-17-5
- Methylene blue p. a, CAS: 61-73-4
- Mn-Zn Ferrite microparticles as supplied by industry
- PK 20 TiO_2 anatase nanoparticles
- KRONOS TiO_2 anatase nanoparticles
- TiO_2 hydrolysates of TIPP, as prepared in work of Cihlar and co-workers [151]

4.5.2 Used Equipments

- SYMPATEC NANOPHOX PCCS analysis
- SYMPATEC HELOS KR Laser diffraction analysis
- TA INSTRUMENTS Q600 + THERMO NICOLET IS10 DTA – TGA analysis
- JEOL JSM-7600F Scanning Electrone Microscopy
- ZEISS EVO LS 10 Scanning Electrone microscopy
- FEG SEM QUANTA 200 F Scanning Electrone Microscopy
- XRD D8 DISCOVER System
- XRD PAN ANALYTICAL System
- UV – 2600 SHIMADZU UV-VIS-NIR Spectrometer
- LAKE SHORE 74707 VSM Magnetometer
- NOVA E 2200 BET Surface area analysis
- Ultrasonic bath 113 T, sonication frequency 40 KHZ
- UV 240 KRÜSS UV lamp with 2 possible UV wavelength : 254, 366 nm
- AXIS ULTRA X-ray Photoelectron Spectroscopy system
- THERMO NICOLET IS10 FT-IR Spectrometer
- POLARON SC7640 Au sputter coater
- TESLA BS349 C sputter coater
- 2100Q HACH´s portable turbidimeter

5 RESULTS AND DISCUSSION

5.1 Hydrolysis of Titanium alkoxides

Analyzing the turbidimetry for estimation of kinetic rate of hydrolysis, the measured data for different *R* during hydrolysis are shown in table 7. The X stands for no recorded turbidity after twelve hours of measurement, T_{max} represents the crossing of the measurement range of turbidimeter, reaching value over 1000 NTU.

Tab. 7 Prepared samples of hydrolysates of Ti-alkoxides with varying *R*

Alkoxide	Molar ratio (*R*)					
	0,5	1	2	4	8	16
TIETH	T_{max}<60s	T_{max}<15s	T_{max}<5s	T_{max}<2s	T_{max}<2s	T_{max}<2s
TIPP	X*	T_{max}<800s	T_{max}<60s	T_{max}<5s	T_{max}<2s	T_{max}<2s
TIBUT	X	X	T_{max}<1500s	T_{max}<60s	T_{max}<5s	T_{max}<5s

* Althought, no measured turbidity was observed after 12 hours, the growth of transparent crystals was observed, which were analyzed in further measurements in this chapter.

5.1.1 Kinetic study

Turbidity of solution of alkoxide was measured upon rapid addition of water in solvent with the turbidimeter. For isopropoxide and butoxide, two molar ratios were selected for the estimation of impact of temperature on the hydrolysis. Titanium isopropoxide was measured with $R = 1$ with used solvent isopropanol, butoxide was measured at $R = 2$ with used solvent n-butanol.

To get the value of induction time ($t_{induction}$) the linear slope in range of high development of turbidity was analysed by applying linear function on the end of steep increasement of turbidity, typically for the last five values of turbidity recorded before the exceeding of the measuring range of turbidity to reveal value of time on axis x. The induction times with projected linear regresions equations from last five values of turbidity are presented in table 8.

As can be seen on figures 21 and 22 with increasing temperature, the induction time was reduced and furthermore however for TIBUT sample the reduction of induction time is not as big as for the TIPP sample. With higher temperature, higher rate of hydrolysis is observed for both samples.

Tab. 8 Induction time evaluation from kinetic measurements with linear regression equations

Temperature (°C)	25	35	45
TIPP $R = 1$ t_i (s)	625	492	257
Linear regression equation	y = 13.06x - 3352.9	y = 12.36x - 6081.3	y = 7.392x - 4619
TIBUT $R = 2$ t_i (s)	1 057	969	846
Linear regression equation	y = 2.1893x - 2315	y = 13.85x -13428	Y = 11.728x - 9921

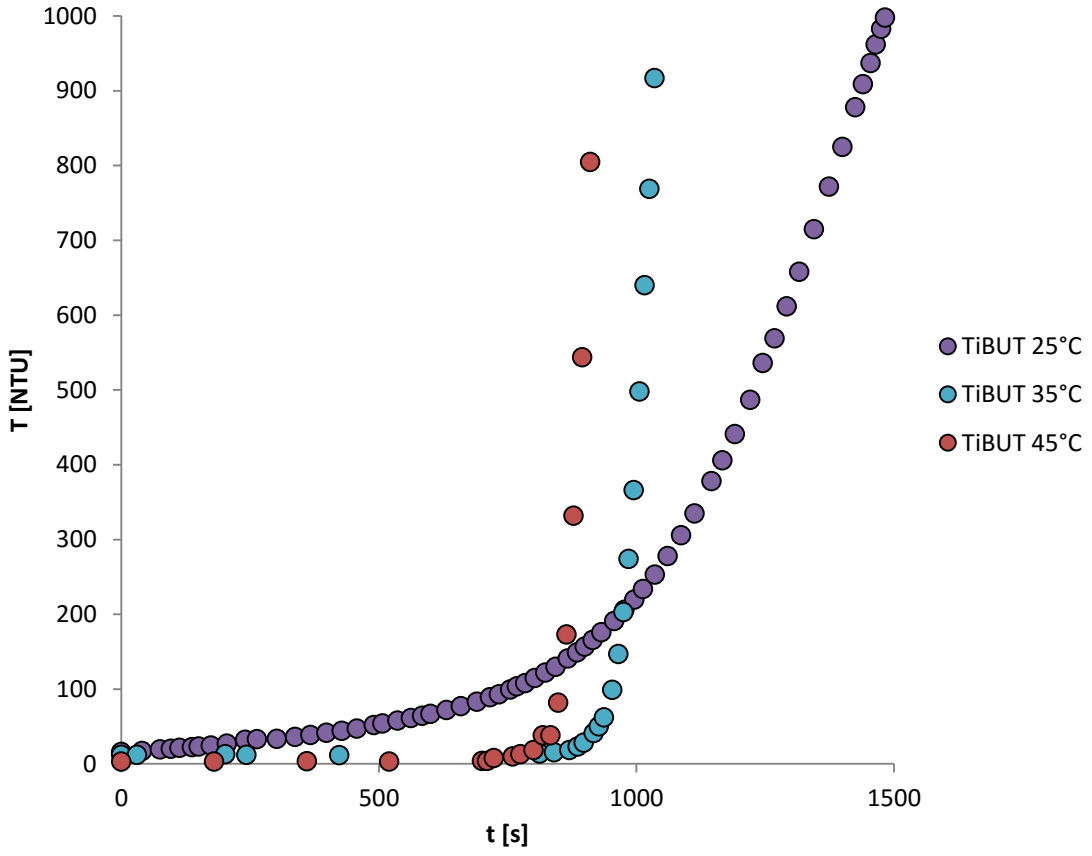

Fig. 21 Hydrolysis at different temperatures turbidity increasement for TIBUT $R = 1$

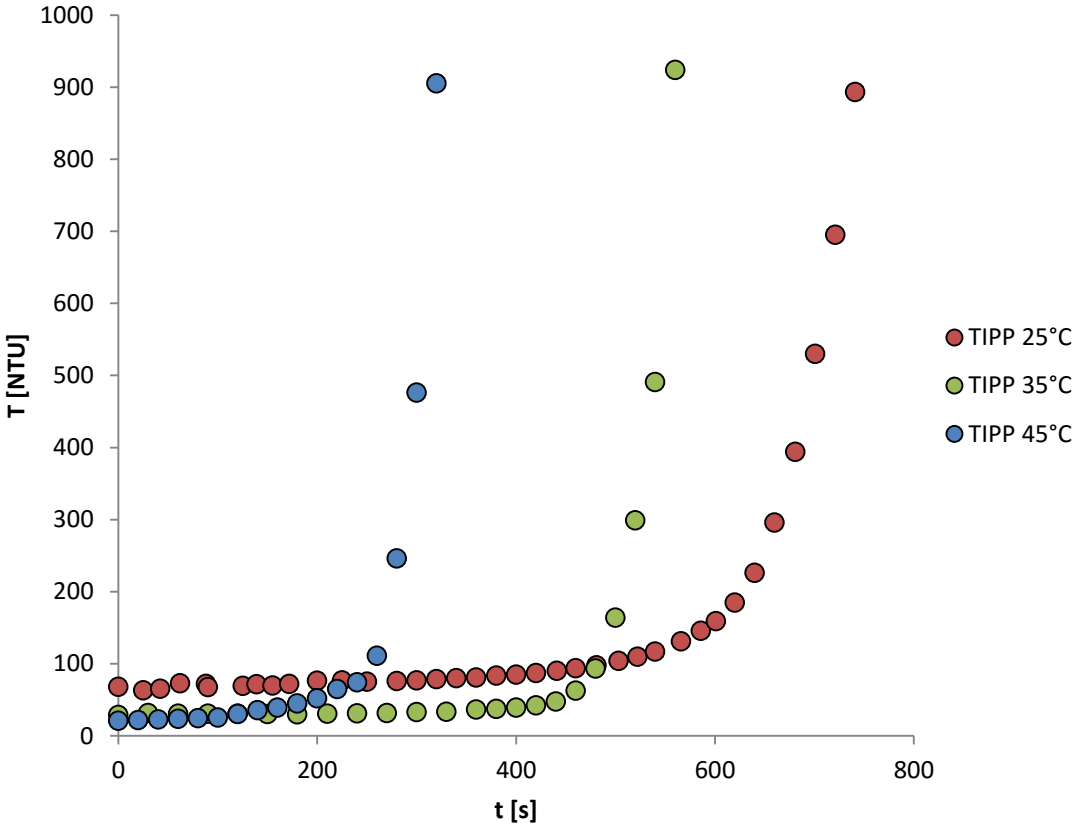

Fig. 22 Hydrolysis at different temperatures turbidity increasement for TIPP $R = 2$

5.1.2 DTA – TGA analysis

As can be seen on figures 23 – 25, the main loss of weight is detectable upon heating until 300°C, after that, only small loss of weight in range of 1 – 2 % is seen. Heatflow from sample is corresponding to the loss of weight mainly in range above 200 °C where upon changing the rate of weight decrease, the heatflow reduces. For the evaluation of mass loss in this range, the derivation of weight upon temperature was used. This procedure was done for all analysed samples. Steep crystallization peak can be furthermore observed, when heatflow from sample arrises quickly for a while with negligible change in weight of sample.

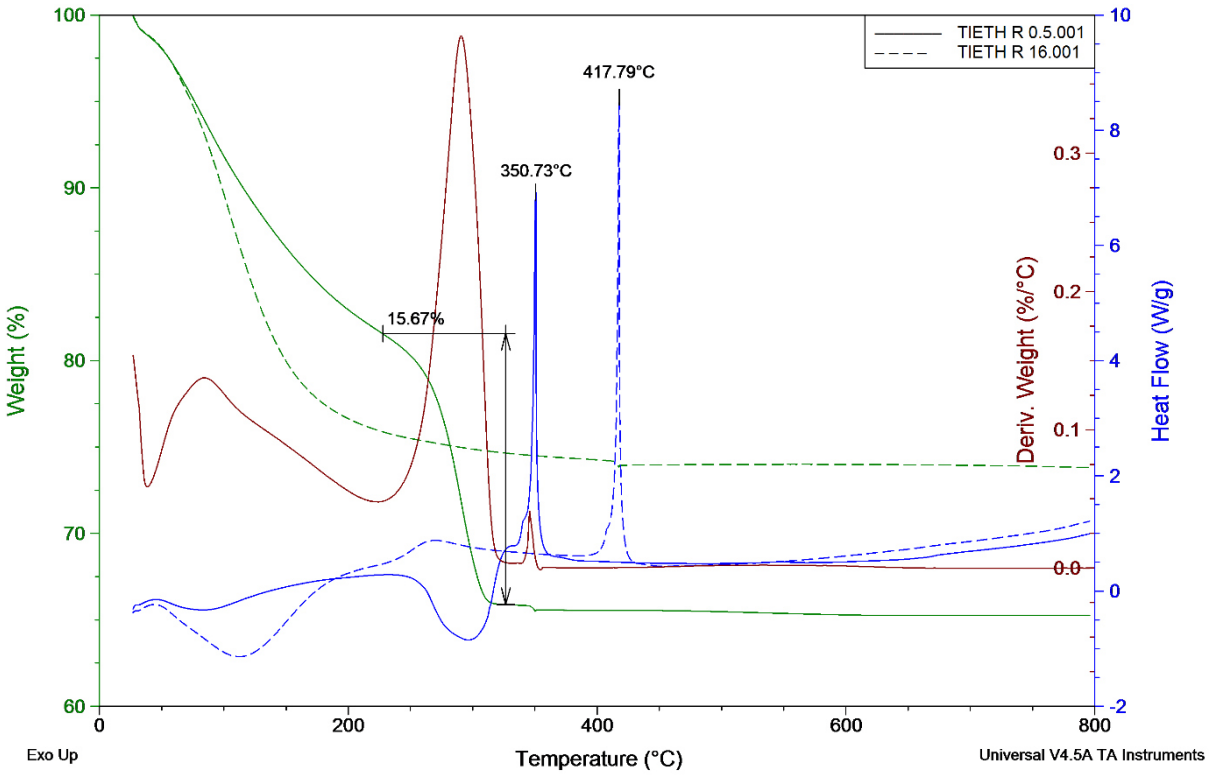

Fig. 23 DTA – TGA analysis of TIETH with different *R*

Derivation of temperature is presented for Ti-alkoxide hydrolysate samples with lowest *R* to maintain the figures comprehensible.

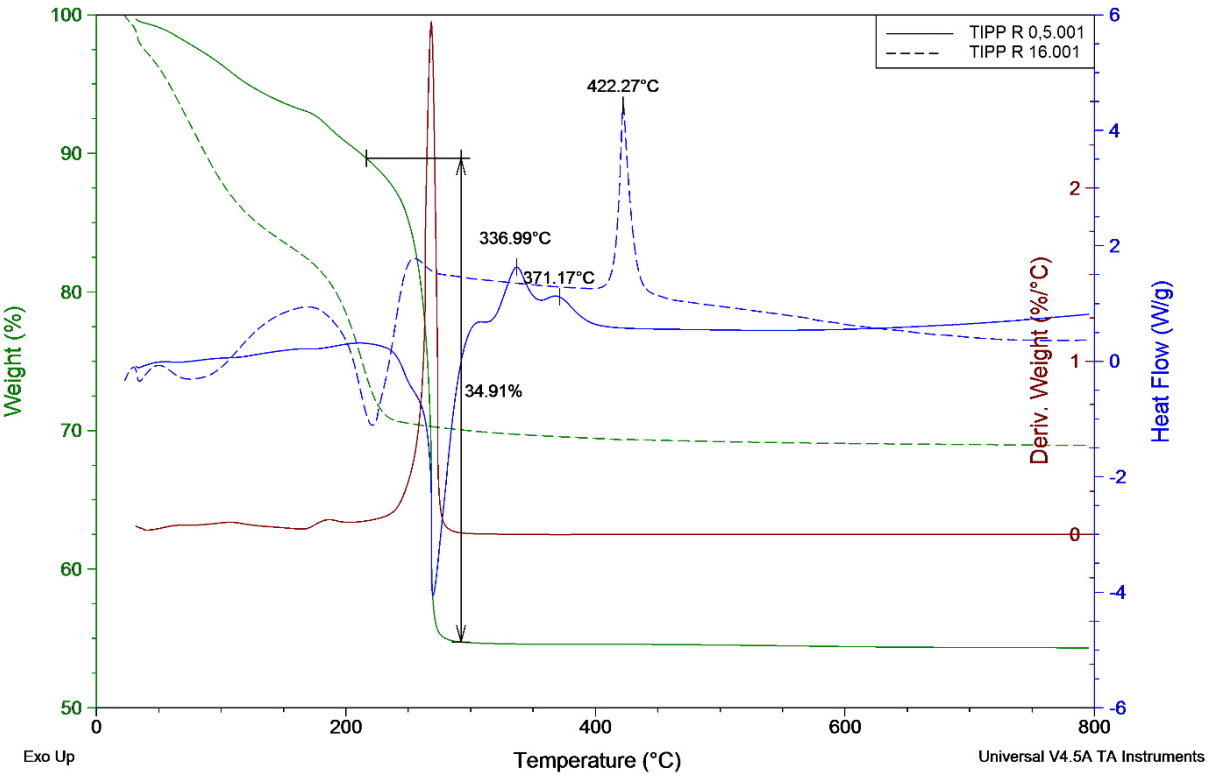

Fig. 24 DTA – TGA analysis of TIPP with different *R*

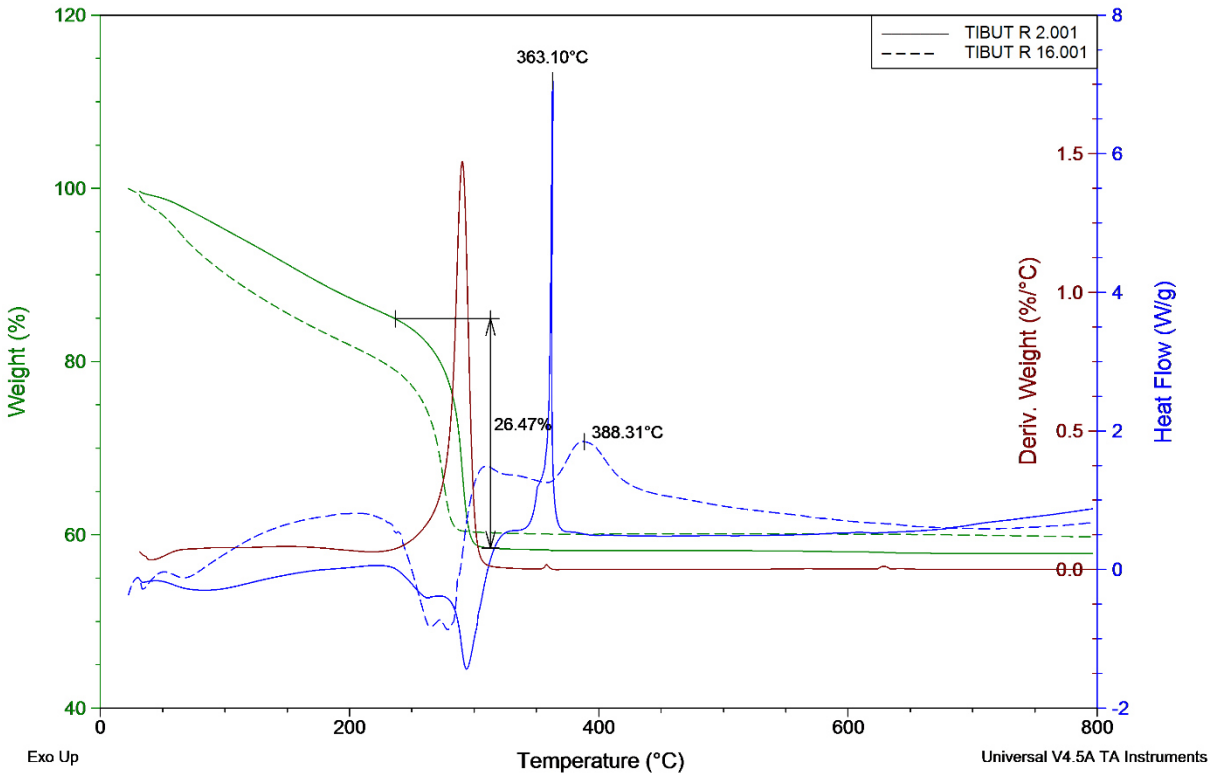

Fig. 25 DTA – TGA analysis of TIBUT with different *R*

Table 9 concludes the obtained data. For TIPP samples with *R* = 0.5 and 1.0 the two possible crystallization peaks were identified, in TIBUT samples X represents no recorded value as no particle formation happened in 12 hours range.

Tab. 9. Crystallization temperatures and weight loss in temperature range 220 – 320 °C for different *R* of hydrolysed Ti-alkoxides

Molar Ratio (R)		0.5	1	2	4	8	16
ETOH	Weight loss (%)	15.7	10.3	9.8	9.2	5.9	1.0
	T_{cryst}(°C)	350.7	355.0	357.9	365.0	396.8	417.8
TIPP	Weight loss (%)	34.9	19.5	14.3	25.01	23.2	13.0
	T_{cryst}(°C)	337.0 371.2	329.7 374.5	377	368.8	368.3	422.3
TIBUT	Weight loss (%)	X	X	26.5	23.4	18.4	20.7
	T_{cryst}(°C)	X	X	363.1	365.57	382.6	388.3

EGA analysis spectras of evolved gas are projected as example for ETOH sample with $R = 4$. Figure 26 shows the comparison of spectras collected during the analysis in 2D diagram emphasizing the development of peaks with color scale change.

The overall intensity of IR absorbtion spectra in range 4000 – 400 cm^{-1} with increasing time is plotted in Gram-Schmidt figure 27. As can be seen from Gram-Schmidt spectra, two peaks of overall absorbtion intensity are seen with intensity at time 14.4 and 31.5 minutes, these time values are representing temperatures of 160 and 330 °C respectively.

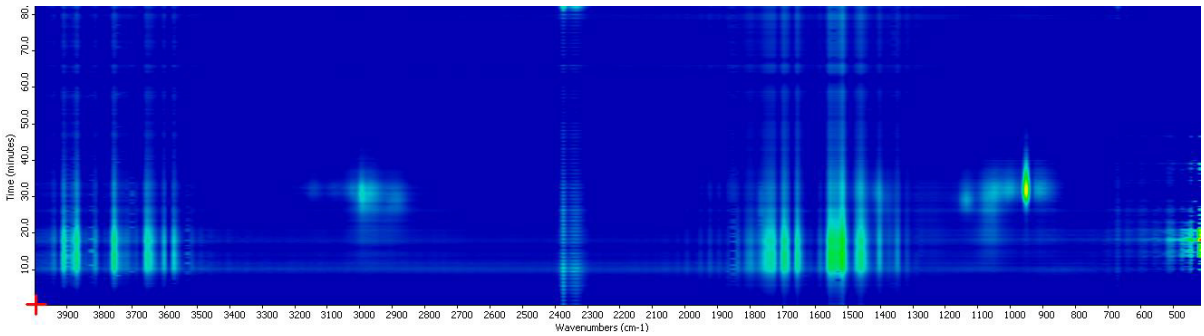

Fig. 26 2D graph of EGA sampling during DTA – TGA analysis.

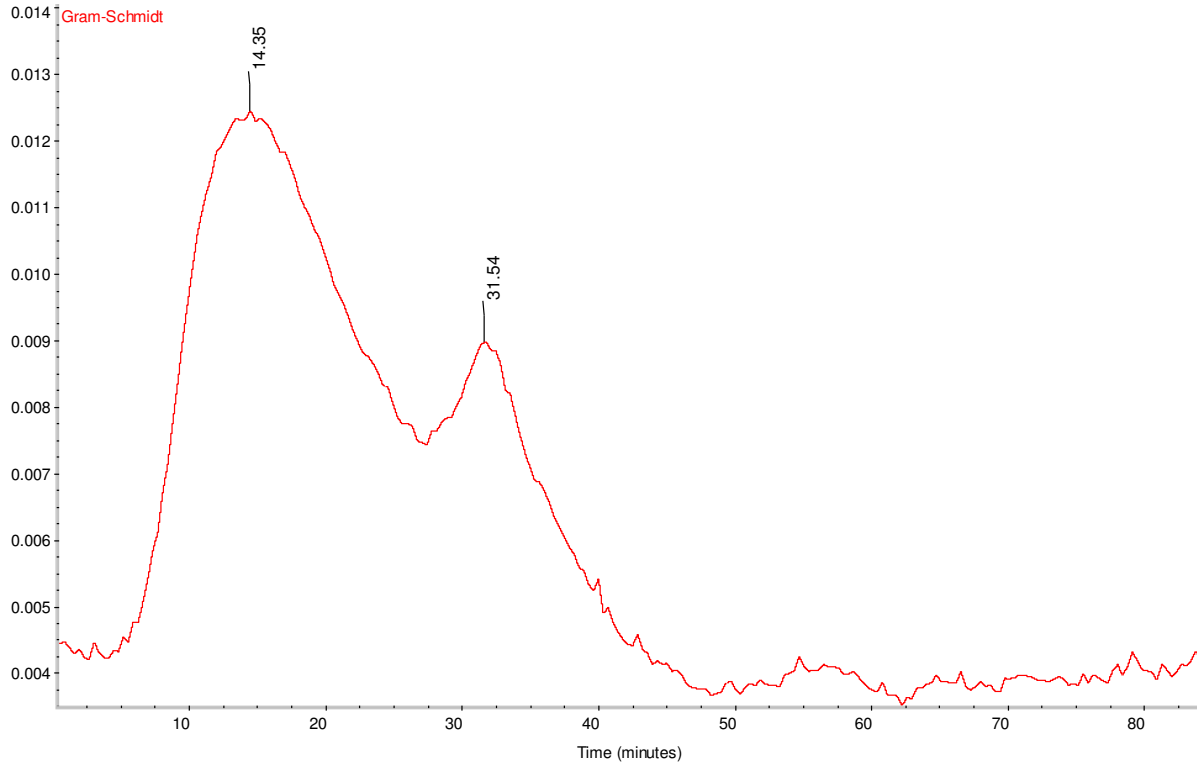

Fig. 27 Gram-Schmidtt analysis of hydrolysed TIETH $R = 4$

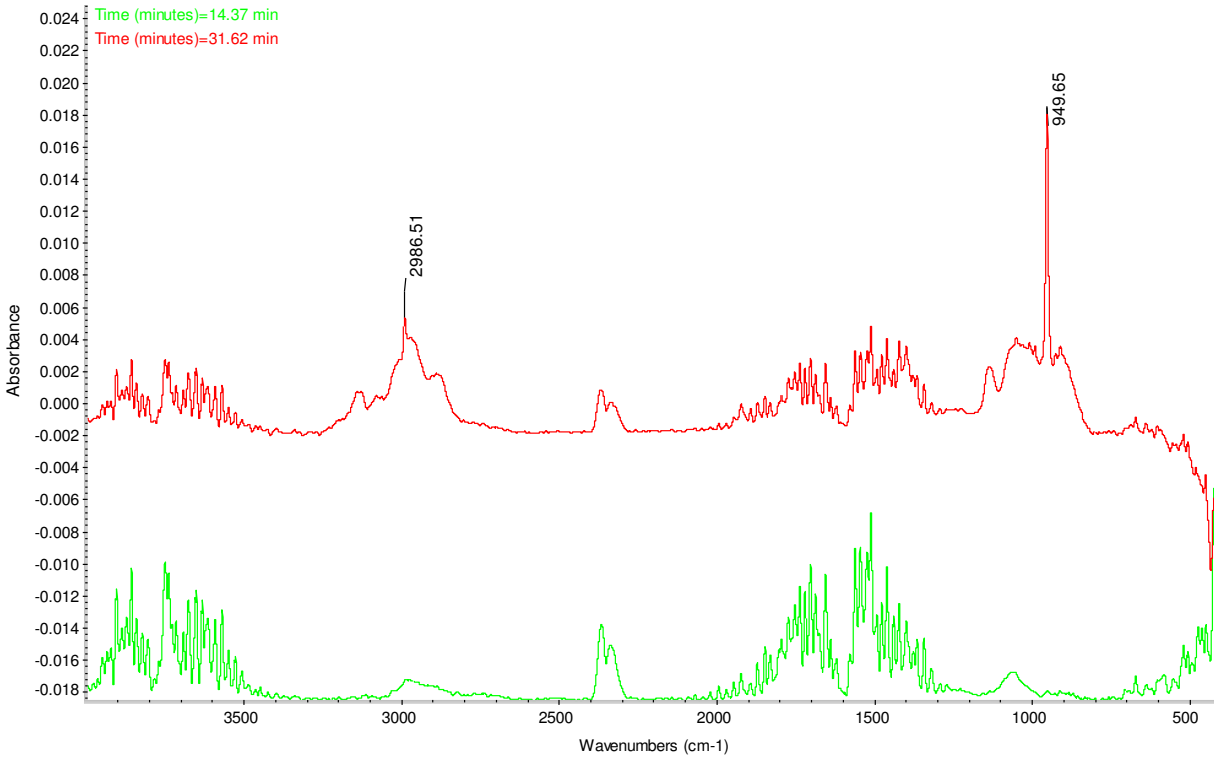

Fig. 28 FTIR spectra recorded in Gram-Schmidt intensity peaks for gas evolution when analysing the TIETH hydrolysate with $R = 4$

Figure 28 is showing the difference of IR spectra recorded for absorbtion intensities from Gram-Schmidt diagram at time 14.4 and 31.5 min. Some positions of peaks in spectra are shown for later evaluation of characteristic vibrational spectra.

5.1.3 BET analysis

In table 9 the obtained data from analysis of specific surface by multipoint adsorption analysis of nitrogen are presented.

Tab. 9 Specific surface determination with different *R* of Ti-alkoxides

Ti-alkoxide	Molar ratio (*R*)		
	0.5	2	16
TIETH S_{BET} ($m^2 \cdot g^{-1}$)	8.64	X	51.4
TIPP S_{BET} ($m^2 \cdot g^{-1}$)	4.166	X	118.8
TIBUT S_{BET} ($m^2 \cdot g^{-1}$)	X	8.64	83.58

As can be observed, the specific surface changes with applied molar ratio. The observed differences were also reported when sintering the hydrolysed samples as when the Ti-alkoxides hydrolysates with lowest *R* were sintered, the formation of grey to black powders was observed with bulky structure, whereas all Ti- alkoxides samples with $R = 16$ exhibited white colour after sintering.

5.1.4 XRD analysis

XRD analysis was performed on the heat treated samples before and after heat treatment. Samples of prepare hydrolysates were in most cases amorphous, showing no diffraction. However in case of TIPP samples with molar ratio R = 0.5 – 1 the possible formation of uncommon crystalic structure was recorded after the evaporation of solvent and analysis of hydrolysate as it was also noticed during hydrolysis of Ti-isopropoxide. Its diffraction pattern is shown in following figure.

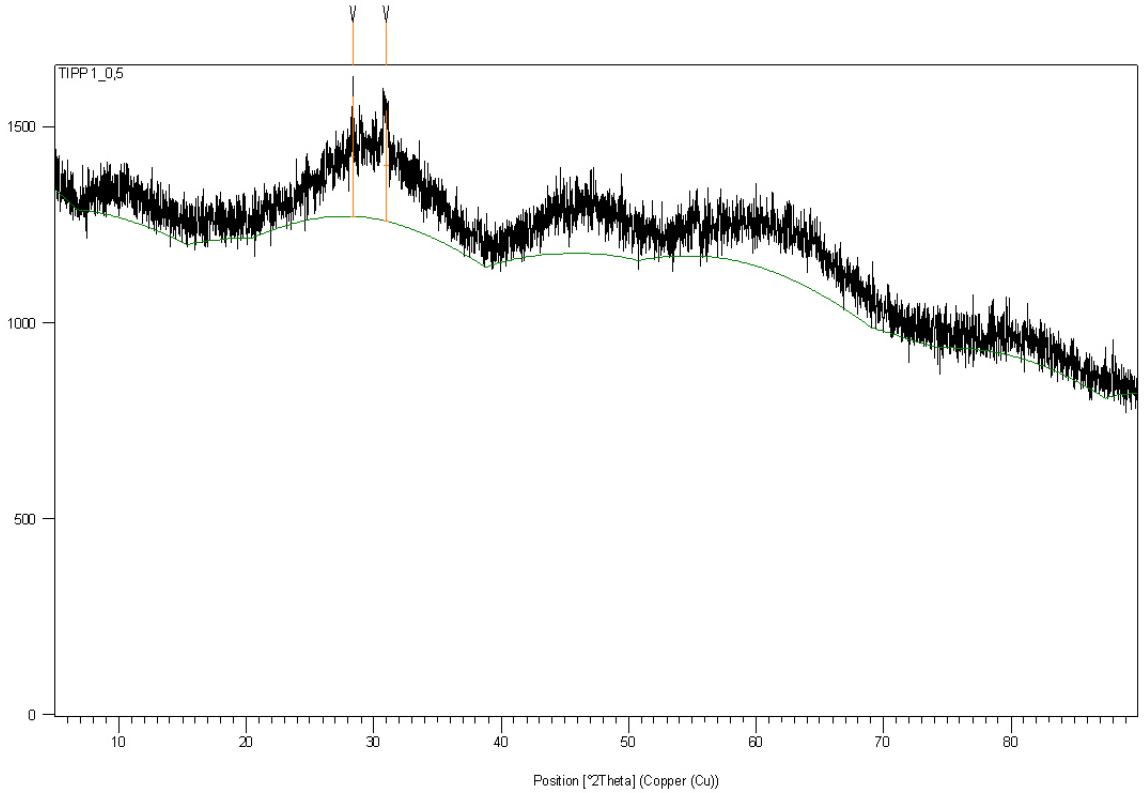

Fig. 29 Diffraction patern of unknown phase for sample TIPP R = 0.5

It was noticed, that this crystalic structured compound is exhibiting observable growth when the hydrolysed solution of TIPP with R = 0.5 is heated in order to evaporate the solvent at given concentrations of Ti-isopropoxide to the TIPP. When this solution was left unatanded in laboratory conditions in test tube with septa, only few crystals growed in 12 hours range. Heating such aged solution leaded to formation of big crystalic particles, whereas when directly applying evaporation of solvent to the just hydrolysed solution after addition of isopropanol with certain amount of water, much smaller particles appeared.

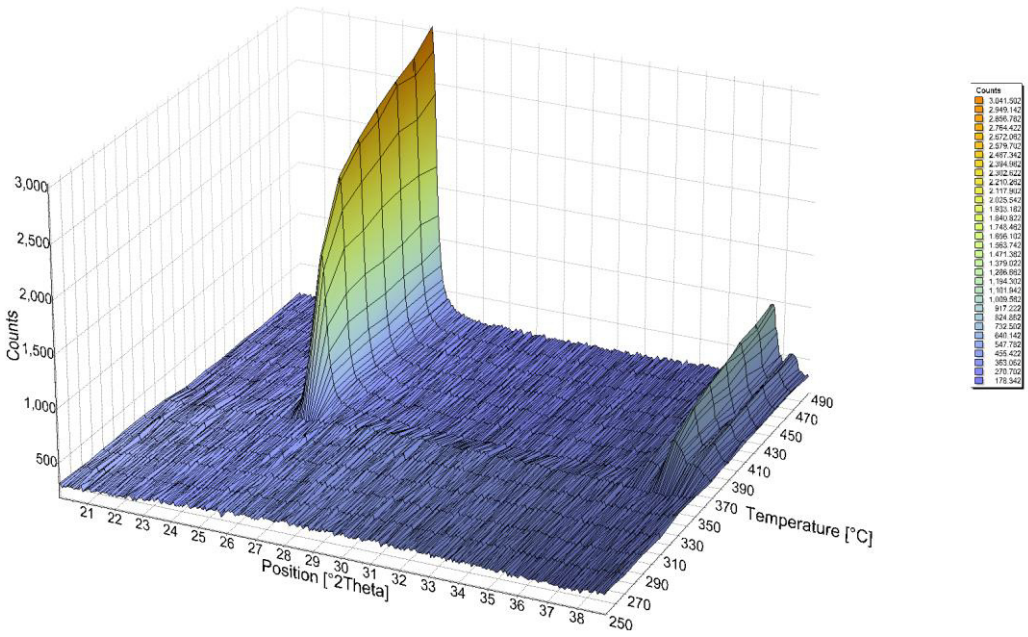

Fig. 30 3D XRD series graph formation of anatase for TIBUT $R = 2$

As can be seen the figure 30 is showing the 3D XRD spectra in small range of °2 Theta (°20 – 40). Full-range spectra is recorded for sample TIBUT $R = 2$ in figure 31 after cooling the sample in XRD furnace down to the 25°C. Also the evaluation of recorded peaks is given in figure 31. Pt XRD diffraction peaks are recorded as it is the material of the sample holder in heating cell.

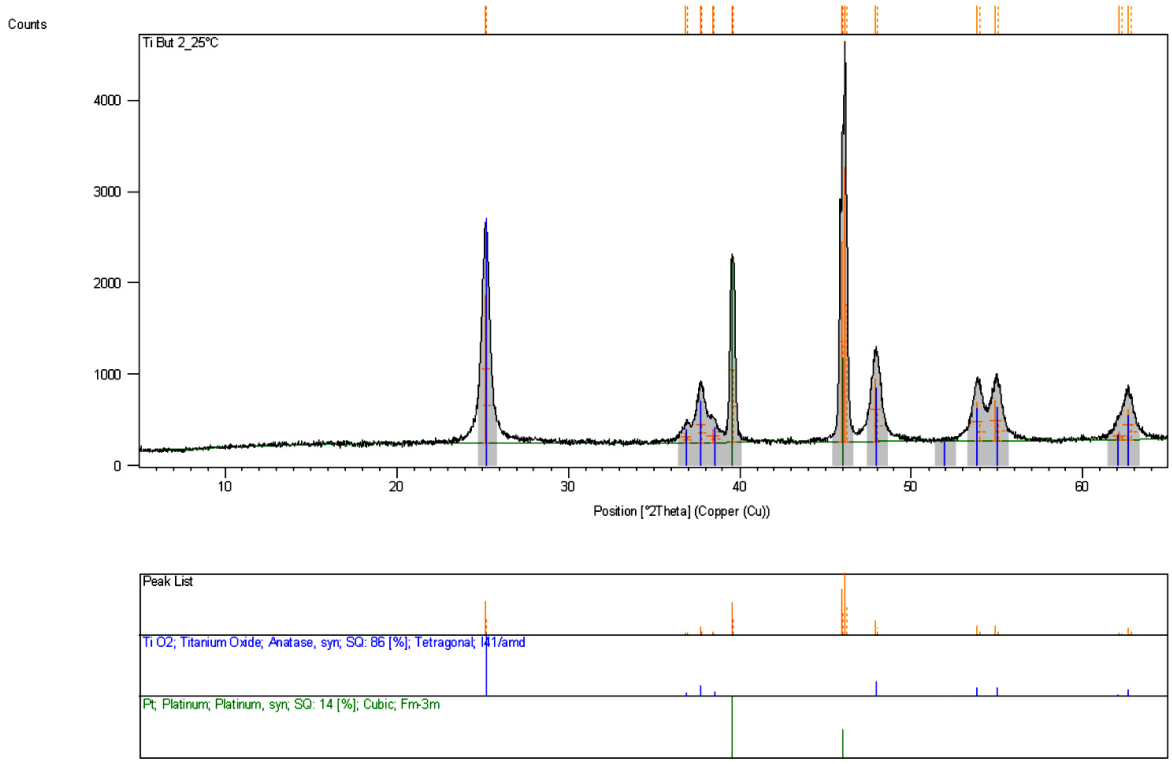

Fig. 31 Full Range XRD spectra for sample TIBUT $R = 2$

Results of Scherer´s equation (58) calculated crystallite size of anatase phase for molar ratio of Ti-alkoxides are demonstrated in table 10.

Tab. 10 Size of anatase crystallites with temperature treatment

TIETH ($R = 2$)		TIPP ($R = 2$)		TIBUT ($R = 2$)	
T (°C)	Size (nm)	T (°C)	Size (nm)	T (°C)	Size (nm)
370	34.4	390	16.4	370	9.0
390	35.5	410	17.7	390	9.3
410	34.2	430	19.2	410	10.1
430	34.7	450	19.1	430	11.0
450	34.2	470	20.0	450	11.4
470	33.8	490	20.3	470	12.0
490	34.4	25	20.3	490	12.8
25	34.1	-	-	25	13.4

The growth of crystallite size was observed with increasing temperature except the TIETH sample.

5.1.5 SEM analysis

SEM analysis of sample of hydrolysed TIPP with R = 2 before (A) and after the sintering process at 450 °C for two hours in oxygen athmosphere furnace is shown in figure 32 followed with the EDS analysis of samples in table 11.

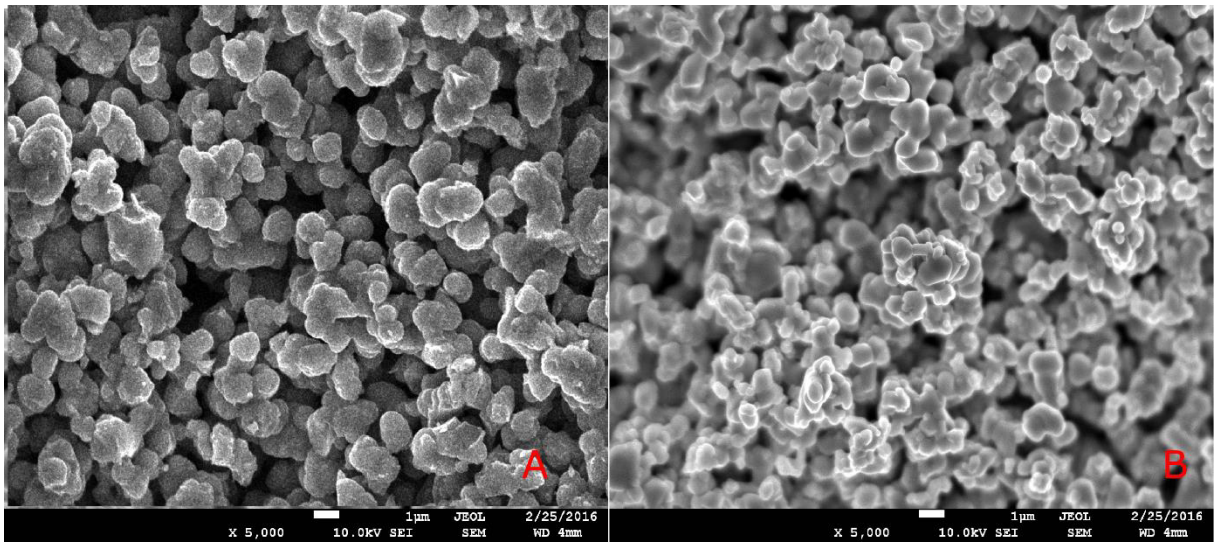

Fig. 32 SEM analysis of TIPP $R = 2$ sample after hydrolysis (A) and after TGA – DTA analysis (B)

Tab. 11 Composition of particles according to the EDS measurement

Sample	Ti (% weight)	O (% weight)	C (% weight)
Hydrolysed TIETH R = 2	57.73	41.26	1.01
Sintered TIETH R = 2	59.95	40.05	0

For EDS measurement, the scanning mode of surface was done. As can be seen on SEM analysis shrinkage of particles can be observed upon the crystallization in temperature of 450 °C for two hours. The surface morphology of heat-treated particles remains nearly same, althought some flattening of surface of hydrolysates can be observed upon heat treatment.

5.1.6 PCCS analysis

Table 12 concludes the results of particle size measured by NANOPHOX (Sympatec) PCCS instrument. Particle size is decreasing with increasing *R* during hydrolysis.

Tab. 12 Results of PCCS analysis

	R = 1	*R* = 4	*R* = 16
TIETH	1 474 nm	865 nm	160 nm
TIPP	1 530 nm	1 193 nm	519 nm
TIBUT	-	1 250 nm	877 nm

5.1.7 Conclusion of chapter

In selected concentration of alkoxides, the hydrolysis reaction is influenced by molar ratio of water to hydroxide and the temperature during the hydrolysis. With increasing *R* the hydrolysis rate is so high, that the turbidity measurement can´t be used for kinetic measurement. The selected alkoxide with increasing molar weight is resulting in the slower rate of hydrolysis reaction for same *R*. For reaction to proceed, the molar ratio needs to be increased for higher molar weight of alkoxide and for the higher molar weight of solvent.

DTA – TGA analysis of hydrolysed samples shows the crystallization process with high precission in heated samples. During heating of samples in Ar atmosphere the weight loss is observed until reaching 320 °C in all hydrolysates from various Ti-alkoxides with different *R* ratios. Weight loss rate is in temperature range until 320°C varying with distinguishable changes of rate in range from 200°C till 320°C creating the highest peak of derivative weight in this region for samples with different molar ratio of TIPP and TIBUT and samples of TIETH excluding the TIETH samples with *R* = 8 and *R* = 16. In general, the position of crystallization exothermic peak in DTA – TGA analysis spectra is increasing with *R* during hydrolysis. Analyzing the samples of TIPP with *R* = 0.5 and *R* = 1 two different crystallization peaks can be observed. Furthermore with increasing *R* the decrease of weight loss of hydrolysed

samples is observed in temperature range from 200°C till 320°C. In this temperature range, the weight loss is increasing with higher molar mass of solvent and with decreasing *R* during hydrolysis.

Gram-Schmidt analysis connected with EGA measurement revealed the possible origin of weight losses in hydrolysates during DTA – TGA measurement. The analysis performed on TIETH sample wit $R = 4$ showed the loss of water and adsorbed OH groups happens mainly in temperature range untill 200°C followed with the decomposition and loss of rests of solvents which are chemisorbed on the surface of hydrolysates. As can be seen in 2D graph of EGA peaks evolution in IR sampling spectra this desorption and probably also burning of solvents was observed only in small range of temperatures (typically less than 50°C range). One must also notice the EGA analysis instrumentation suffers from the need of preheated tube transfer of evolved gases into the IR spectrophotometer, therefore the dilution of evolved gas with carrier gas and delay of receiving the spectral changes is unavoidable.

Decomposition of presented solvent in hydrolysates with lower $R = 0.5 – 1$ was confirmed after the heat treatment at 450 °C as the color change of samples happened, resulting in dark grey samples of crystalic anatase with higher contents of carbon. This change can be also observed when performing the SEM analysis with EDS, where the cautios decrease of C peak in EDS spectra was observed analyzing samples with higher *R*. Lower the *R* is, higher content of solvent can be observed in produced hydrolysates. Considering the sample of TIETH with $R = 16$, nearly no solvent is presented, as there is no endothermic effect in heatflow observed at the relevant temperature range mentioned earlier.

Considering the rate of hydrolysis, of TIPP, TIBUT and TIETH as shown in table 7, the TIETH sample hydrolysis with $R = 2$ took only less than 5 s time to reach maximal turbidity, whereas very slow hydrolysis products increasement could be observed by turbidimetric measurement for TIBUT sample with same *R* in 15 000 s time range.

EGA IR spectra obtained from the analysis of TIETH sample with $R = 4$ contained sharp absorbtion peaks in range of 3 580 – 3 650 cm^{-1} representing the free O-H groups accompanied with another stretching vibration in range of 970 – 1 250 cm^{-1} representing the C-O bonding together with absorbtion in range 2 850 – 3 100 cm^{-1} where stretching vibrations of C-H group appear. In analysed spectra also the increasement of CO_2 peak at 2 364 cm^{-1} can be observed nearly at the end of the DTA analysis, where its sudden increasement happens at temperature above 700°C confirming the final decomposition of organic matter in hydrolysates. Moreover it can be assumed, that with different alkoxide used with increasing *R* the smaller content of solvents binded in hydrolysates was observed.

Measurement of XRD of hydrolyzed alkoxides showed no crystallinity except the formed phase in TIPP samples with $R = 0.5$ and $R = 1$ where crystalline phase was formed. This phase suffered from the low crystallinity and was probably responsible for two different crystallization peaks appearance measurement formation in DTA – TGA analysis, where probably one exothermic peak with no weight loss can be attributed to the recrystallization of this phase into anatase. This phase was undeconvulated as low quality XRD spectra was obtained only.

XRD was performed in heat chamber in athmospheric conditions on selected hydrolysed samples to observe the formation of anatase in temperature range 350 – 490 °C. Sampled spectras proved formation of anatase in good accordance with observed DTA – TGA crystalline phase transitions temperatures correcting to highest heat flow in analysed hydrolysates.

For the measurement of crystallite size, the Scherer´s equation was used for same *R* value and different Ti-alkoxides. Using the higher molar mass solvent and alkoxide resulted in lower crystallite size. Considering the rate of turbidity evolution and therefore the rate of hydrolysis as shown in table 7, with increasing rate of reaction, the bigger crystallites were obtained. When increasing temperature, no change of crystallite size was observed for TIETH sample, but for TIPP and TIBUT with $R = 2$ quite certainly the crystallite size growed. In general, the observed growth of peaks in 3D XRD figure 30 can be attributed to better crystallinity of sample, which is connected with decrease of defects in crystalic structure and crystallites domains growth. No change in crystalline growth for TIETH sample can be attributed to the fact, that rate of hydrolysis was so high that easier to crystallize hydrolysates were formed with less solvent adsorbed according to results from table 10: 10, 14 and 27 weight % of solvents were chemisorbed in hydrolysed TIETH, TIPP and TIBUT samples with $R = 2$ respectively. If chemisorption happened at these samples the defects should be taken into account with possibility that the observed growth of crystallites according to the Scherer´s formulation rather corresponds to the amount of chemisorbed solvents and therefore shows the improvement in crystallinity of anatase phase.

As discussed in work of Meilang Wang and co-workers [152] where the hydrolysis of Ti- butoxide was holded in n-octanol, the adsorbed solvent molecules in the surface of hydrolysed intermediates contribute to the slow growth rate of nanoparticles (NCS) as althought the hydrolysed intermediate is full of hydroxyl molecules which was shown quite well in presented results during EGA analysis coupled with DTA – TGA analysis. Existence of dissolved water molecules in solvent is crucial for the completion of the cross-linking reaction in the intermediate, resulting in the final anatase structure. Capping effect of adsorbed solvent molecules on the surface of hydrolyzates is also responsible for the slower rate of hydrolysis as well as the increasing viscosity of used solvent. Mitigation of this effect can be seen as with higher temperatures of hydrolysis, the induction time reduced significantly and growth rate of white precipitates observed by turbidity measurement was higher using the same *R* ratio.

SEM – EDS analysis showed same round shape morphology for prepared samples of hydrolysed Ti-alkoxides with $R > 2$. Presence of some amount of carbon was detected in hydrolysed samples of Ti-alkoxides with $R \leq 2$ using the area analysis scanning mode of EDS. After heat treatment, the peak of carbon in EDS was significantly reduced. This fact further confirms the decomposition of chemisorbed solvents presented in hydrolysates and was in accordance with previously reported EGA and DTA results.

Measuring of the particle size by PCCS NANOPHOX Sympatec´s measurement showed the decrease of particle sizes with lower molar weight of Ti-alkoxide used and with higher *R* used during hydrolysis. No dispergation support was used for the measurement, 5 min of ultrasonification was run for each sample before PCCS

measurement. The measured size is corresponding to the size of particles observed by SEM analysis and as it was observed at high resolution measurement, particles were agglomerated.

5.2 Synthesis of magnetic nanoparticles

5.2.1.1 Temperature impact on precipitation

Table 13 concludes the reaction rates comparison with changing temperature for precipitation with sodium hydroxide. Surprisingly the formation of magnetic particles was observed much earlier than first detectable phase formation by XRD. This fact can be attributed to the lower resolution of XRD as the scans had to be done in short time and the formed particles were actually dispersed in water.

Tab. 13 Precipitation time of magnetite for different temperature

Temperature (°C)	0	22	60	95 – 100
Appearance of green rusts	t < 5 s	t < 5 s	t < 5 s	t < 5 s
Presence of magnetic properties	-	50 min	15 min	3 min
Precipitation time	-	180 min	35 min	t < 10 min

For precipitation at 0°C even after 24 hours there was no visible observation of black magnetic precipitates, nor any response to the external magnetic force. Dark green precipitates were formed without any change of color during reaction.

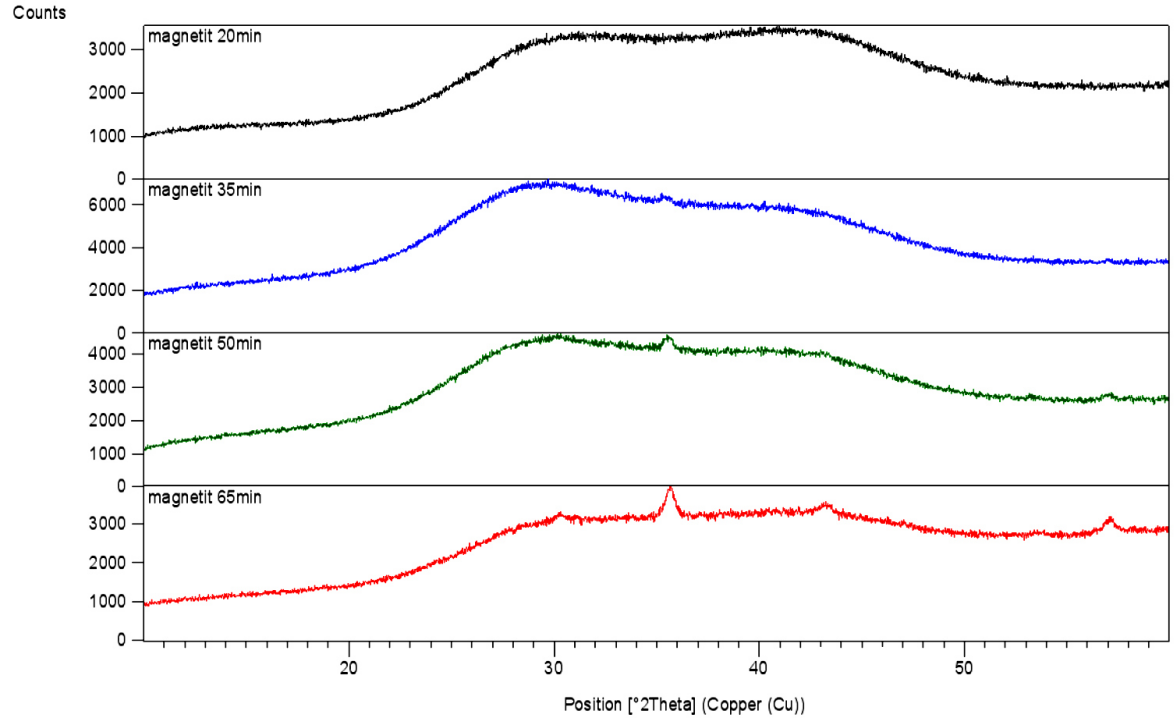

Fig. 33 The precipitation of magnetite from solution of Mohr´s salt at 22°C

In figures 33 and 34 the development of diffraction patterns with time at given temperature is shown together with identification of phases for two different temperatures.

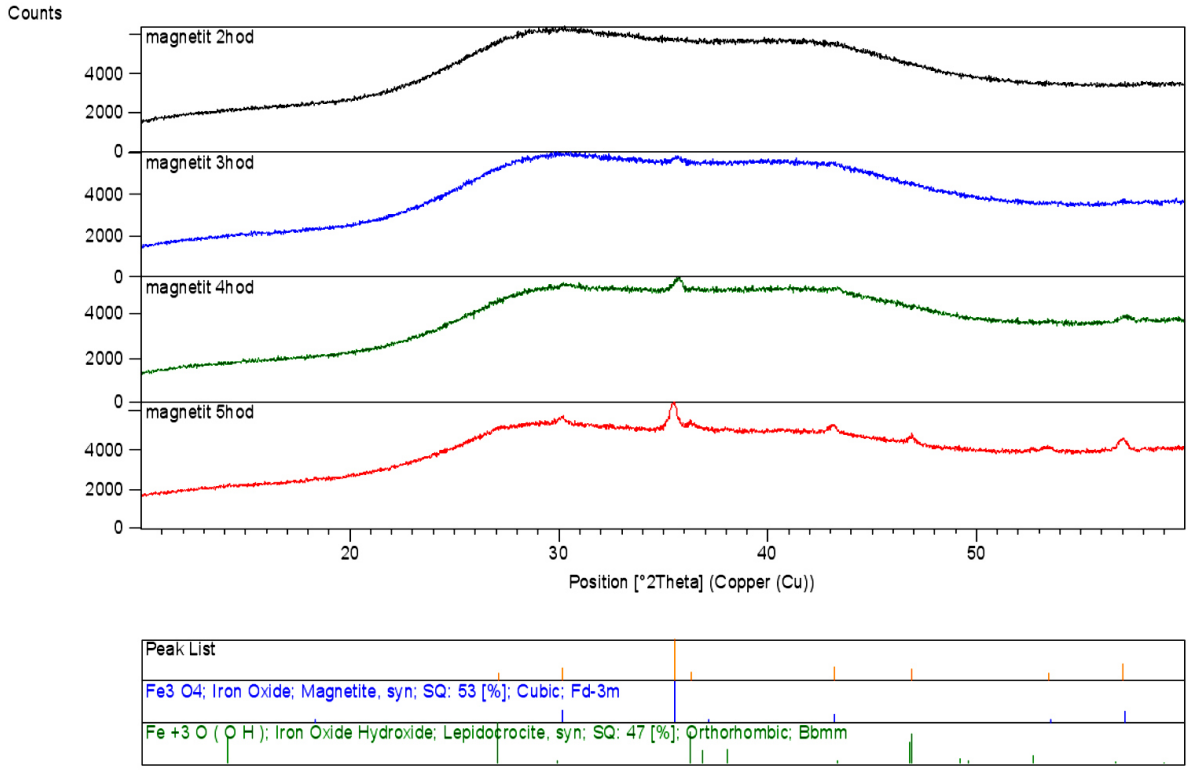

Fig. 34 The precipitation of magnetite from solution of Mohr´s salt at 60°C

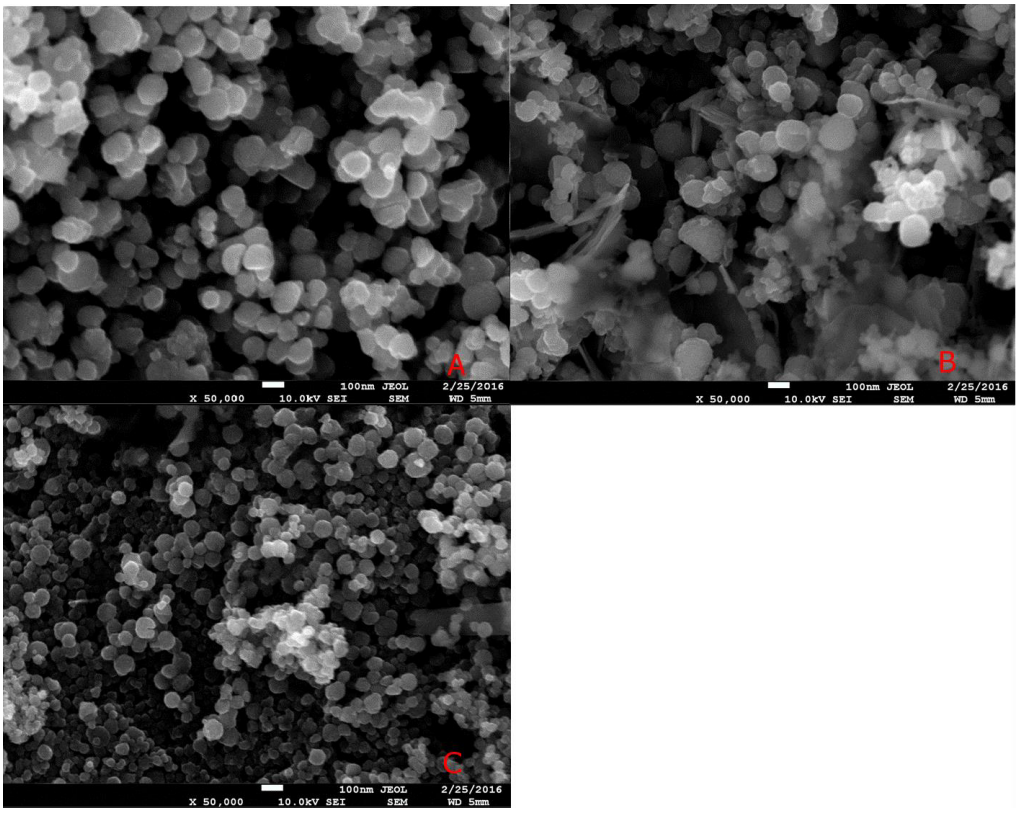

Fig. 35 Temperature impact on magnetite particles: A (22°C), B (60°C), C (100°C)

Formation of magnetite was observed for shown temperatures with later appearance of Lepidocrocite γ-FeO(OH) in laboratory temperature with prolonged period of reaction (5h) Also the increasement in the size and quality of crystallites was observed for both temperatures with increasing time of precipitation. In order to evaluate the changes in particle morphology with temperature conditions, the SEM analysis was done. Figure 35 is showing the SEM analysis of particles prepared with different temperatures.

Morphology of particles is changing with reaction conditions, considering the temperature of reaction. It can be observed that in temperature range of 60°C the formation of anisotropic shaped 2D structures occurred. Particle size difference can be tracked considering the laboratory temperature of synthesis and temperature of synthesis in boiling solution. Reduction of particle size can be observed using 100°C boiling solutions for precipitation of magnetic particles.

5.2.2 Measurement of pH and conductivity

In table 14 the pH of collected magnetic samples, these are also emphesized on the figures 36 and 37 showing the development of pH and conductivity during precipitation reaction. In order to prevent withdrawal impact of samples during synthesis, the relative volume of base is used as a value for axis x where $V_r = V/ V_t$. The V stands for actual volume of base after addition in the reaction mixture and V_t is total volume of base added during precipitation.

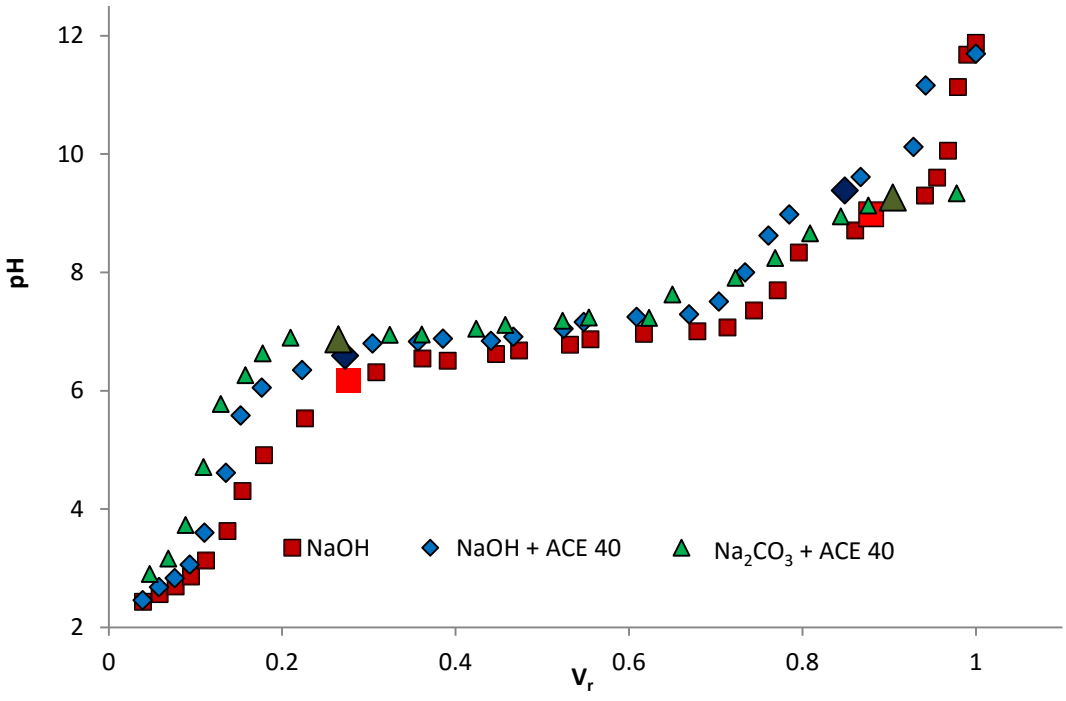

Fig. 36 Changes of pH of Mohr´s salt solution with added volume of base

Tab. 14 Collected samples of magnetic precipitates

Synthesis and parameters	Synthesis 1 NaOH		Synthesis 2 NaOH + 2 ml ACE40		Synthesis 3 Na_2CO_3 + 2ml ACE40	
Sample	1	2	3	4	5	6
pH	6.1	10.0	6.6	9.3	6.9	9.3

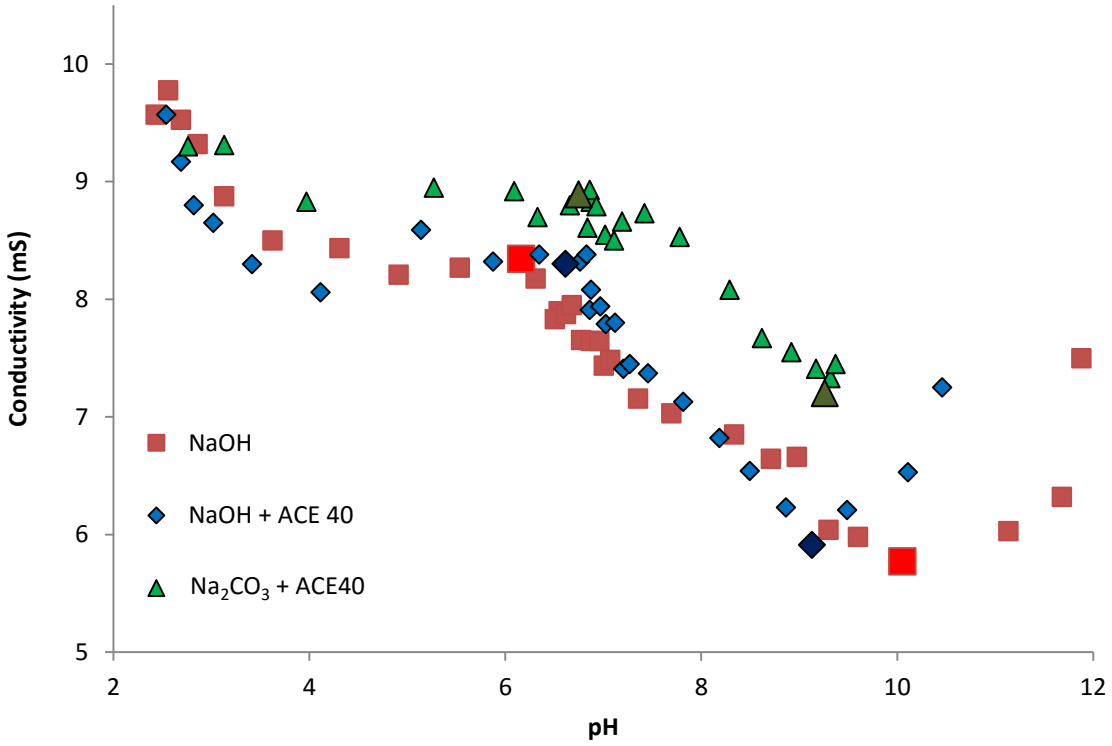

Fig. 37 Conductivity changes with increasing pH

During the precipitation the very first observed change of colorless solution was the appearance of turbidity with significantly orange color formation, which changed with time into the bright green and then turning into the dark green and dark blue resulting in brown to black color at higher pH > 9.

At this pH also the characteristic smell of solution leaving ammonia was detected. Assuming that if the ammonia is released, it should be presented in condensed vapors and therefore it should change the pH of these vapors, the measurement of pH of condensates from cooler during synthesis was done. It was observed that at pH > 7.5, the significant increase of pH of condensed vapors is detected, showing values pH ≈ 9 for condensate.

Agglomeration of precipitates at high pH was observed as the black precipitates were sedimenting and clear solution over them was formed when finishing the synthesis.

This behaviour was affected by ACE 40 application as at the pH range above 9 the highly turbid black solution was formed with no observed sedimentation for further 5 hours after finishing synthesis.

5.2.3 DTA – TGA analysis of magnetite nanoparticles

In order to verify the presence of superplasticizer on surface of magnetic particles, the DTA – TGA analysis was performed in oxygen athmosphere for samples of NaOH base and NaOH base with ACE 40 presence. Analyzed samples were 2 and 4 according to the table 14. Results are presented in figures 38, 39.

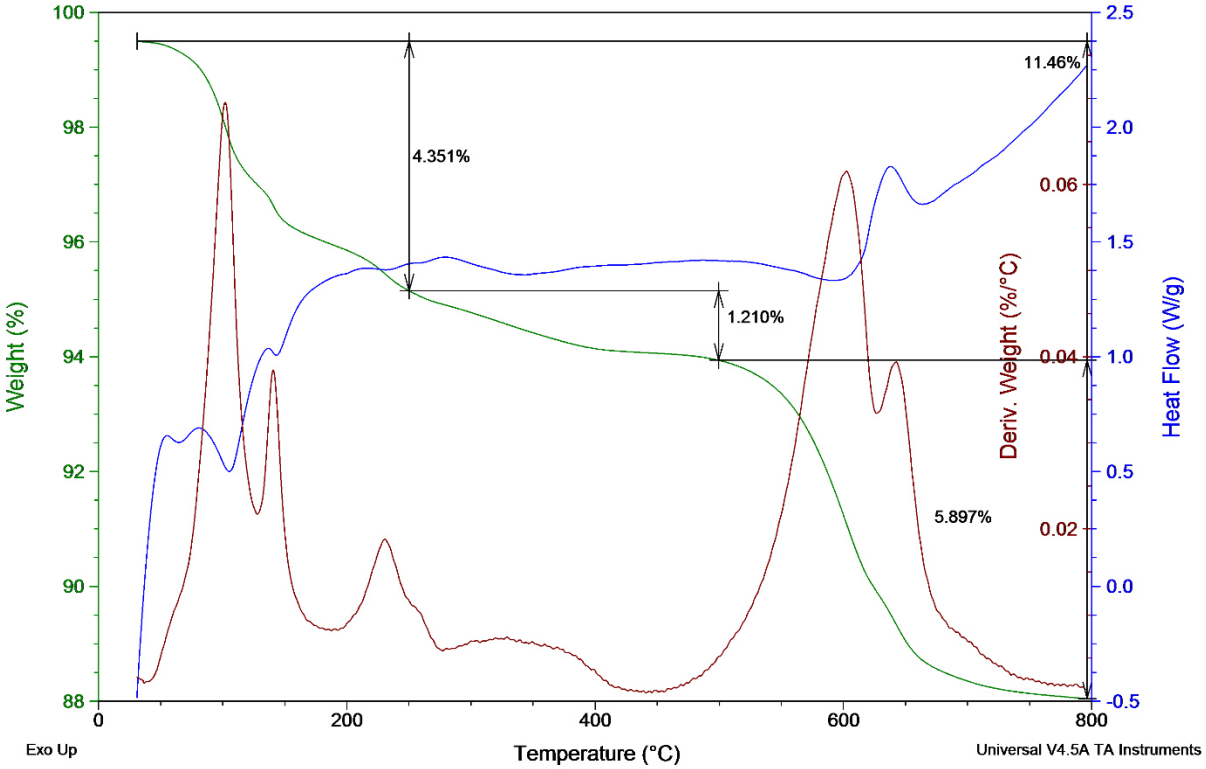

Fig. 38 DTA – TGA analysis of prepared magnetite particles (sample 2)

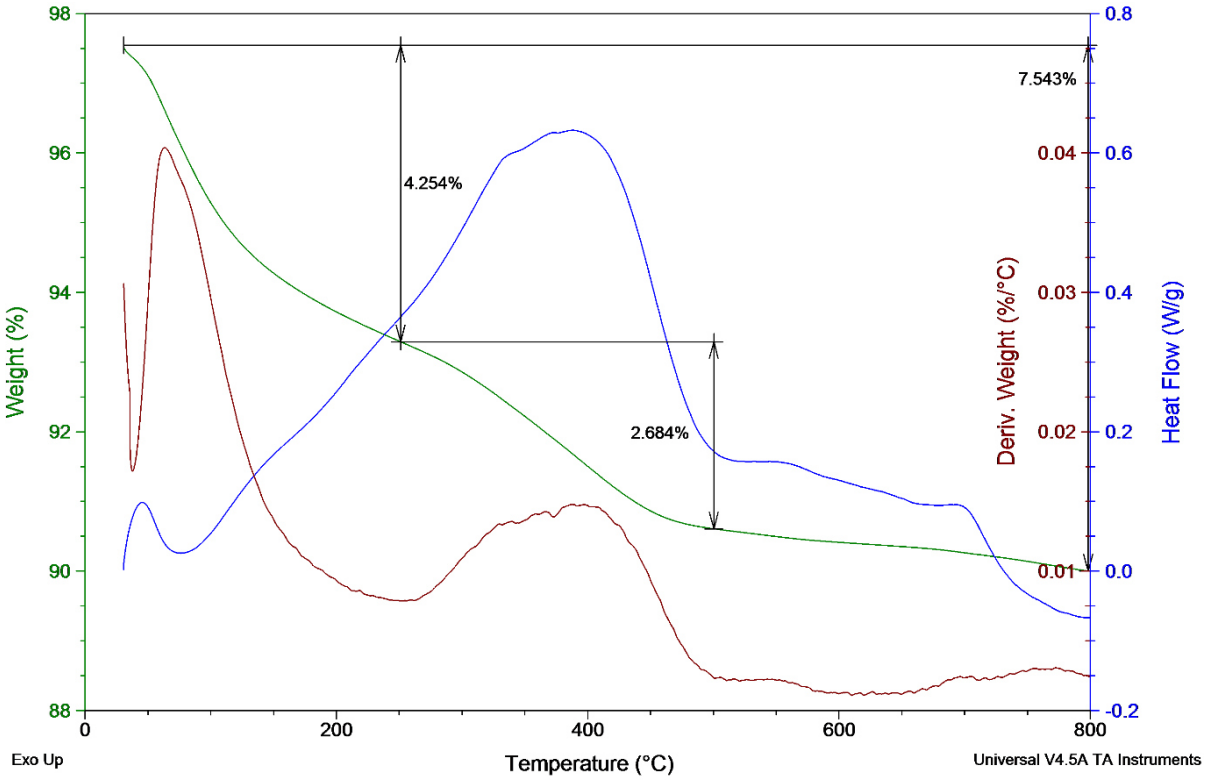

Fig. 39. DTA – TGA analysis of prepared magnetite particles with ACE 40 (sample 4)

Both samples were exhibiting the same rate of initial loss of weight until 250°C. Then analyzing the differences between prepared magnetite samples, it is observed that the sample 4 including the treatment with the superplasticizer compared to sample 2 with no surface treatment shows in temperature range of 250 – 500°C a loss of 2.7 % weight whereas only 1.21 % of mass loss for sample 2 is observed. The main difference is observed in temperature range above 500°C, where the magnetite sample with no surface treatment is exhibiting loss of 5.9 % of weight, whereas the surface treated magnetite is showing only 0.5 % loss of weight. Differences of heatflows of measured samples are observed too.

5.2.4 Magnetization measurements of magnetite nanoparticles

Magnetization was proceeded on the selected magnetization measurement was done using the LAKE SHORE 74707 VSM equipement. Figure 40 shows the magnetization curve obtained for NaOH and NaOH with ACE 40 and Na_2CO_3 with ACE 40. Obtained values of saturation magnetization and measured coercivity are shown in table 15.

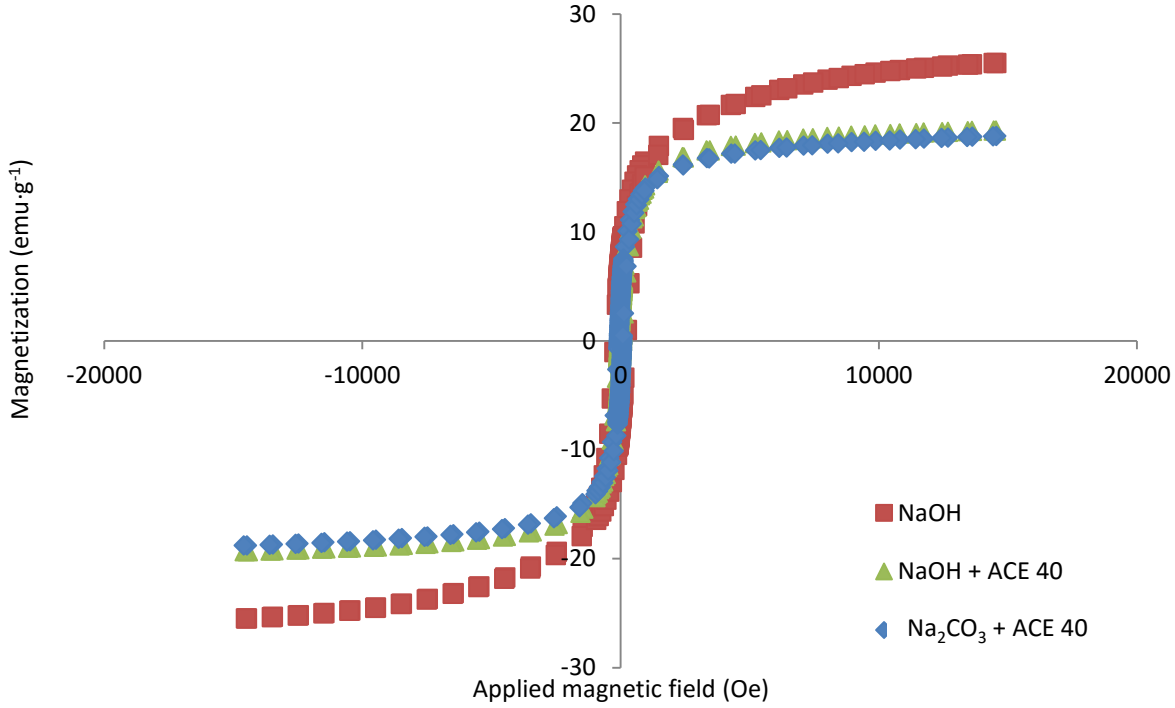

Fig. 40 Magnetization measurement of magnetite nanoparticles

Tab. 15. Obtained data from magnetization measurement

	Synthesis 1 NaOH	Synthesis 2 NaOH + 2 ml ACE 40	Synthesis 3 Na_2CO_3 + 2ml ACE 40
Saturation magnetization (emu·g^{-1})	25.5	19.3	18.8
Coercivity (Oe)	218.1	53.7	72.4

As can be observed, the particles coated with ACE 40 superplasticizer exhibited lower coercivity and lower magnetization than particles syntethized with NaOH used as base for precipitation of magnetite from solution of Mohr´s salt.

5.2.5 XRD analysis of magnetite nanoparticles

XRD analysis using the XRD D8 DISCOVER was done on samples showed in table 14. Figures 41 and 42 show the diffraction patterns with identification of crystalline phases for very first magnetic samples withdrawal and for samples with lowest conductivity recorded.

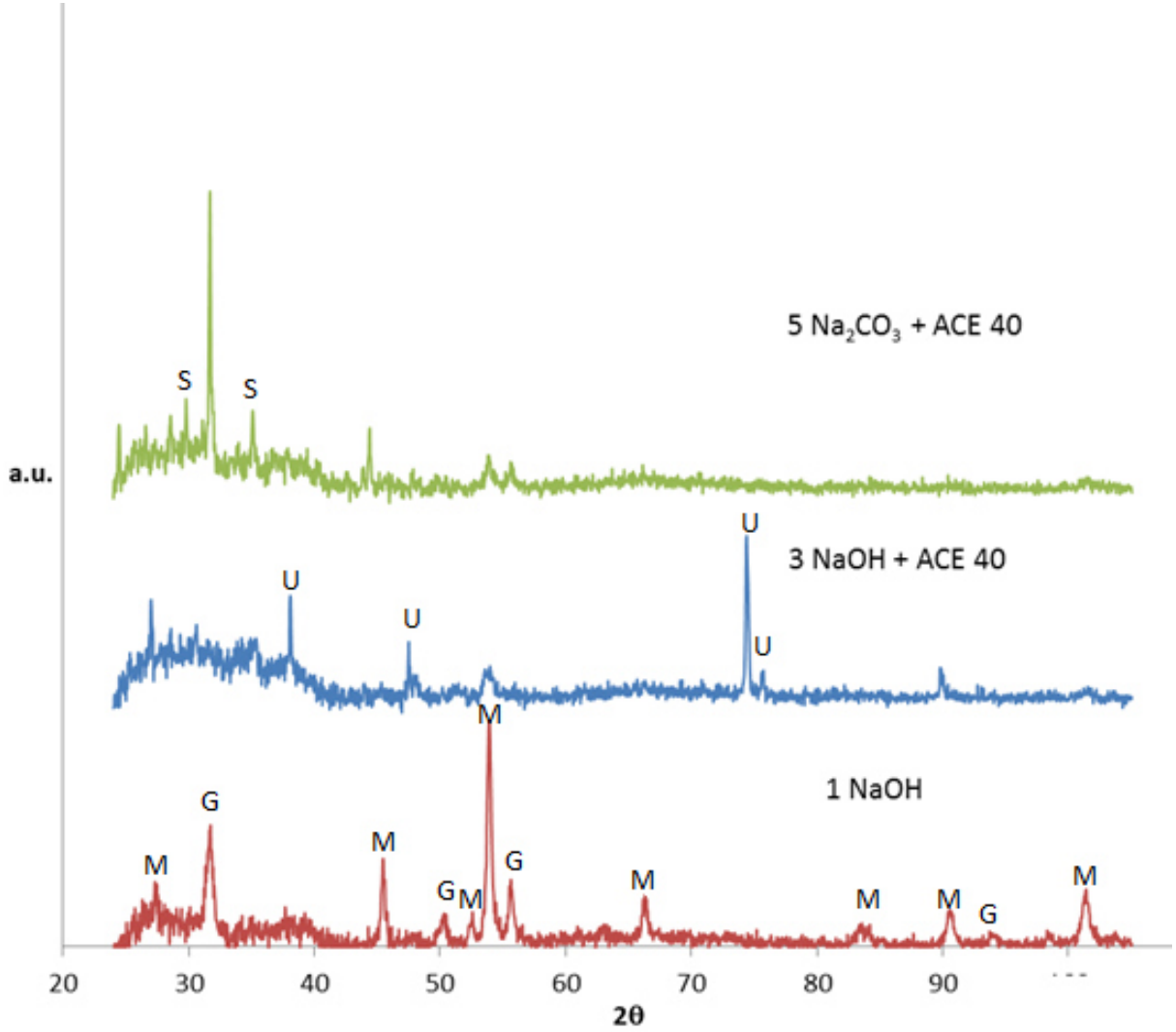

Fig. 41 XRD of first magnetically active particles during nanoparticles precipitation

In figure above, the M stands for magnetite diffraction line, G stands for the goethite diffraction peak and U stands for the unknown diffraction pattern, which was formed and S was identified as a possible traces of sodium sulfate appearing as probably impurity which remained when washing particles with distilled water.

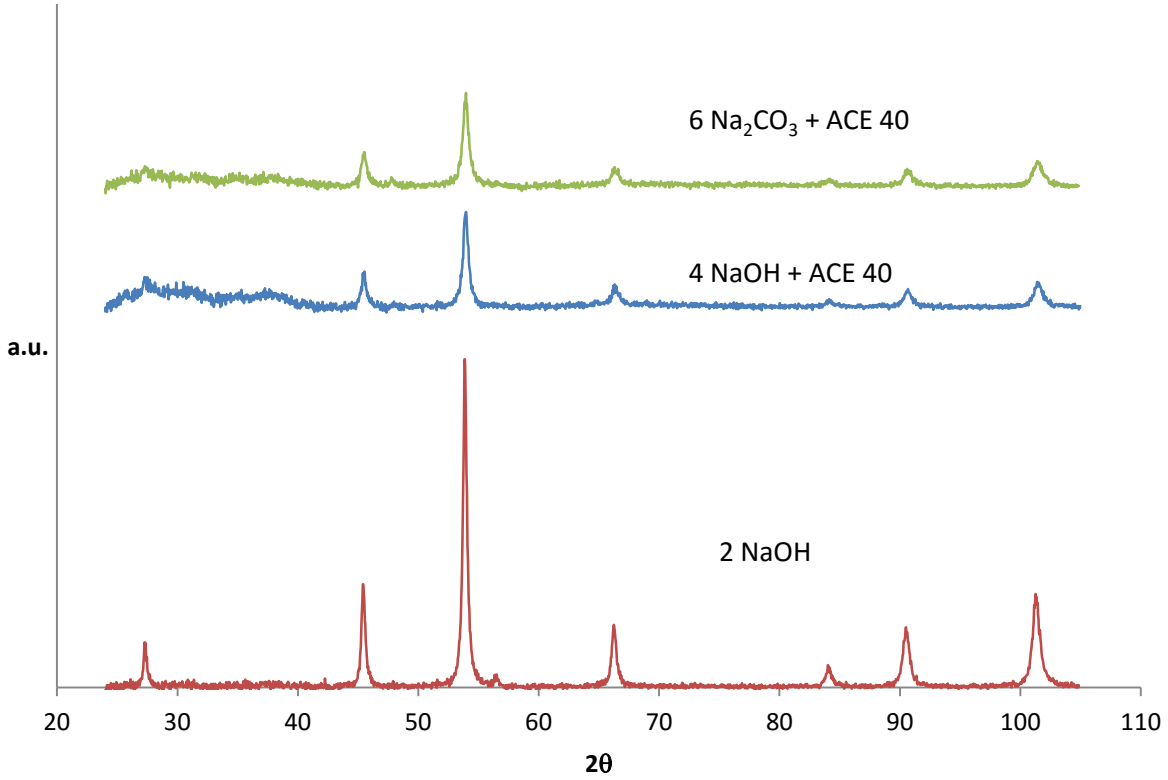

Fig. 42 XRD of magnetic samples during lowest conductivity measured

Analyzing the XRD patterns in figure 42, only magnetite phase appeared. According to obtained XRD spectra, the best crystallinity is obtained for the particles synthetized with the use of sodium hydroxide base. With applying the ACE 40 superplasticizer the broader peaks of formed particles were recorded. Appeared phases in the lower pH range (pH ≈ 6) were identified as goethite and magnetite.

5.2.6 SEM - EDS analysis of magnetite nanoparticles

Analyzing the particle morphology and size and composition of found samples was done by SEM – EDS analysis using SEM QUANTA 200 F with measuring of EDS spectra of sample 3 containing the unknown phase. Its analysis is shown in figure 43.

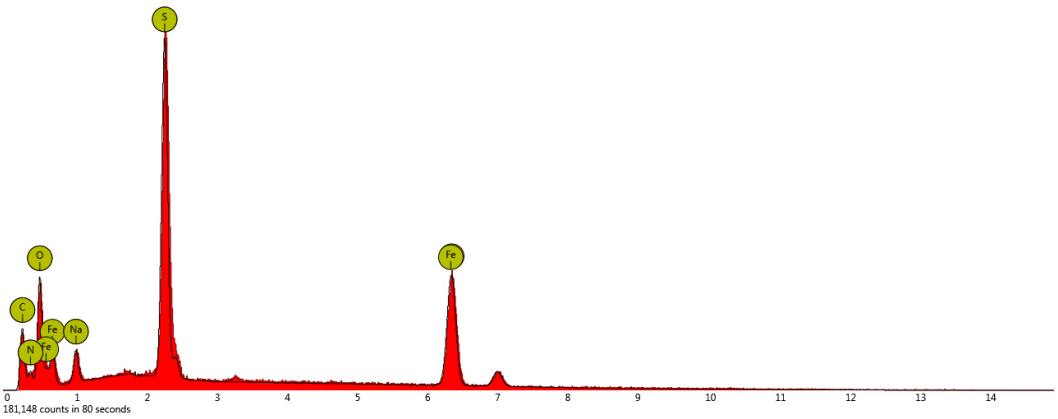

Fig. 43 EDS analysis of the sample 3 with unknown diffraction pattern

Figure 44 shows the prepared and collected nanoparticles according to the table 14. For all samples except sample 3 the same resolution was used.

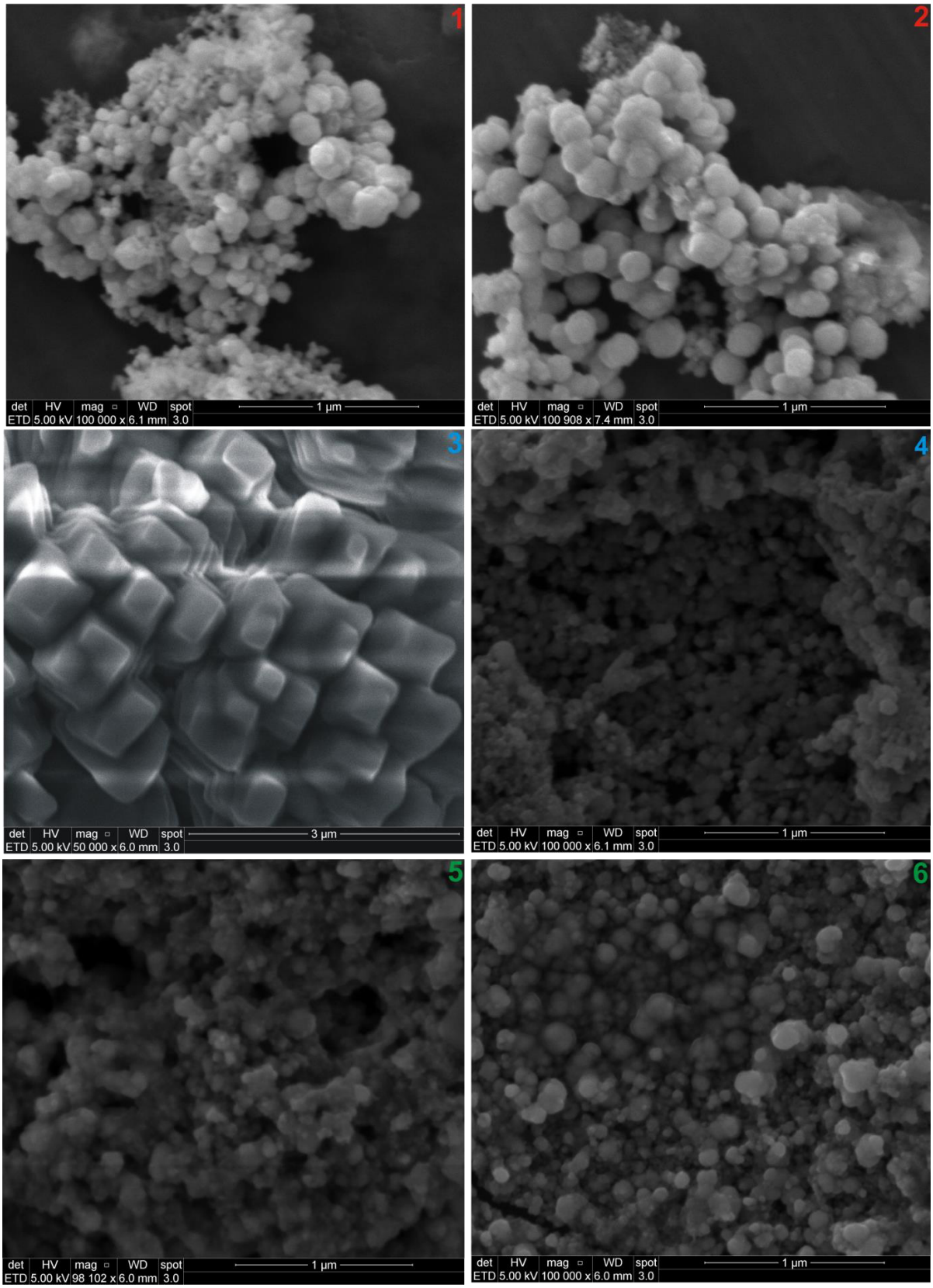

Fig. 44 SEM analysis of prepared magnetic particles

Morphology of samples is changing with the pH during precipitation and is dependent on usage of ACE 40 superplasticizer. With its use the particle size compared to the first synthesis with NaOH usage is significantly lower. Remarkable difference can be observed in particles morphology for sample 3. Agglomeration of particles was observed.

5.2.7 PCCS study

Particle size was estimated using Sympatec´s NANOPHOX PCCS spectrometer. Same procedure was done as mentioned in chapter 4.2.6. In table 16 results of measured particle sizes are demonstrated for samples collected at lowest conductivity: 2, 4 and 6. Better dispergation was observed for particles with ACE 40 surface treatment.

Tab. 16 Size distribution of prepared magnetite particles

Sample	2	4	6
D_{50} (nm)	2 350	232	684

5.2.8 Conclusion of the chapter

Precipitation of magnetic particles can be accomplished using the Mohr´s salt solution and strong and weak base (NaOH, Na_2CO_3) for precipitation.

Precipitation rate of particles is dependent on the temperature of reaction. When the precipitation was done in Dewar container with ice cold water (0°C) no precipitation was observed even after 24 hours of reaction. Still, the appearance of the green rusts coloring the solution into the greenish colours was observed within a few seconds after mixing base solution with Mohr´s salt solution. With increasing temperature, the appearance of the magnetic behavior of precipitates and detection of diffraction patterns of magnetite is observed resulting into the detection of magnetic particles in less than 10 minutes time for precipitation of magnetic particles from boiling solution of Mohr´s salt.

Whereas at temperature of 25 and 100 °C the round shaped particles were observed, when precipitation of magnetic nanoparticles from Mohr´s salt solution was done at temperature of 60°C, the appearance of significant amount of anisotropic shaped 2D structures between typically round shaped particles was observed. Formation of 2D structures in similar temperature was reported also in work of Šutka and co-authors [139] where precipitation from $FeCl_2 \cdot 4H_2O$ solutions was done. Smaller particles were obtained for precipitation at 100 °C. For synthesis with temperature 25°C it was found that the lepidocrocite phase appeared with longer time of synthesis (5 h).

For measurement of pH and conductivity, the synthesis conditions were selected to be boiling solution of Mohr´s salt in apparatus with 100 °C temperature precipitated by the adition of strong and weak base. As could be observed from titration curves, almost no impact on reaction could be attributed to the use of ACE 40 superplasticizer, according to obtained curves.

Appearance of precipitates started when pH of solution was higher than 5 with turning the colour of solution from bright orange through greenish dark into the brown and black color with increasing pH. The formation of magnetite particles was recorded from pH > 6 with increasing amount observed in range of pH 6 – 9 . Quite interesting is the comparison of the measurement of conductivity with pH measurement during precipitation as in the range of pH 4 – 7 the conductivity of samples was nearly same, starting to decrease significantly with linearic slope after appearance of the first magnetically active particles formed at pH ≈ 6. Considering reaction scheme of possible formation of magnetite nanoparticles it can be concluded that the range of pH for the formation of magnetite is 6 – 10.

For a significant amount of the base added into the solution (V_r = 0.2 – 0.7) no pH change is shown. This is in correspondence with the consumption of hydroxylic groups for the reactions of magnetite formation mentioned in chapter 4.3.1. After that, with increasing V_r > 0.7, change in pH increase rate can be observed until lowest conductivity measured. Then the pH is increasing steeply as on the beginning of synthesis. Steep increasement can be attributed to no further consumption of hydroxylic groups and therefore also to increase of conductivity by their presence.

DTA – TGA analysis after several washes of particles with distilled water revealed, that the superplasticizer was chemisorbed on the surface of particles as can be observed that different weight loss and heat flow are presented at temperature range 250 – 500 °C during DTA – TGA analysis of ACE 40 coated and uncoated samples. The deposited carbon is preventing the weight losses in higher temperature range above 500 °C as the uncoated particles exhibited weight 5.9 % weight loss until 800°C and coated particles showed just 0.7 % change.

Magnetization measurement showed that particles were exhibiting relatively low magnetization of 26 $emu \cdot g^{-1}$ which was further reduced when using ACE 40 during synthesis. The reported value of magnetization for bulk magnetite is around 92 $emu \cdot g^{-1}$. The significant change can be attributed to the nanoparticle dimensions as well as to the oxygen chemisorption where the each oxygen atom introduced onto an oxygen site will create iron cation vacancies in the inverse spinel structure of magnetite. The change in the coercivity was observed as the magnetite nanoparticles with ACE 40 had very low coercivity of 57 – 76 Oe, whereas sample prepared by the precipitation with only NaOH showed coercivity of 218.1 Oe. Using the superplasticizer it was observed that the saturation magnetization decreased as confirnment of certain amount of binded superplasticizer.

According to XRD analysis during the synthesis mainly presence of magnetite and goethite diffraction patterns was detected whereas in sample 3 the unknown diffraction pattern was identified together with the presence of the magnetite phase.

As can be seen on SEM agglomerated particles were prepared with size smaller than 150 nm. During first synthesis the goethite phase needle shaped particles can be observed earlier determined by XRD. EDS of unknown particles presented on sample 3 was done in order to obtain the chemical composition of compound. Even when the great effort was done to deconvulate the XRD spectra pattern considering obtained EDS spectra, no possible match was found, therefore it is possible that uncommon

novel magnetically active crystalic phase was prepared. Particles were partially decomposed under X-Ray irradiation with 5 kV as explained in attachements. Size reduction of nanoparticles was observed using the ACE 40 superplasticizer.

5.3 TiO_2 application on magnetic particles and photocatalytic studies

Samples of prepared magnetite in pH range above 9 as mentioned in table 15 were coated with anatase large scale produced TiO_2 particles and selected synthetized amorphous TiO_2 (EXP TiO_2) particles prepared according to the work of Cihlar and co-workers [151] by hydrolysis of TIPP with $R = 100$ with basic properties as shown in following table:

Tab. 17 Properties of used TiO_2 particles

TiO_2 particles	Size (nm)	Specific surface area ($m^2 \cdot g^{-1}$)
PK 20 TiO_2	15 – 35	70 - 110
KRONOS TiO_2	15	> 225
EXP TiO_2	4.4	354

For coating of magnetite, samples 2 and 4 from table 16 chapter 5.2 were selected to perform the TiO_2 coatings without and with surface treatment by hydrolysis of TIPP with $R = 2$.

5.3.1 Turbidity measurement of TiO_2 coated nanoparticles

Table 18 shows the turbidity of core-shell particles prepared from nanosized magnetif particles according to the chapter 4.4.1. Particles were dispersed for 30 min by sonification and then attracted by magnetic force with neodymium magnet in order to sample remanence turbidity, which could be attributed to the TiO_2 released from the surface of nanoparticles. Marked samples (A, B, C, D) are studied by further analysis.

Tab. 18 Turbidity measurement of prepared particles

Particle coating	TiO_2(NTU)	TiO_2 + TIPP hydrolysis (NTU)
PK 20 TiO_2 + NaOH	65.3	5.95
PK 20 TiO_2 + NaOH + ACE 40	11.2	6.71
KRONOS TiO_2 + NaOH	74.1	5.21
KRONOS TiO_2 + NaOH + ACE 40	15.1	2.4
EXP TiO_2 + NaOH	61.4 (A)	7.5 (C)
EXP TiO_2 + NaOH + ACE 40	13.3 (B)	2.9 (D)

The presence of superplasticizer on the surface of the nanoparticles of magnetite has big influence on the remanence turbidity measured after 30 min of ultrasonification of prepared particles. In general, the TIPP coating procedure helps to the decrease of the remanence turbidity.

5.3.2 SEM – EDS measurement of TiO_2 coated nanoparticles

SEM measurement revealed the differences of particles morphology with preparation method used. Feg SEM quanta 200 F and JEOL JSM-7600F were employed for the analysis. The samples for EXP TiO_2 from table 18 are shown in figure 45.

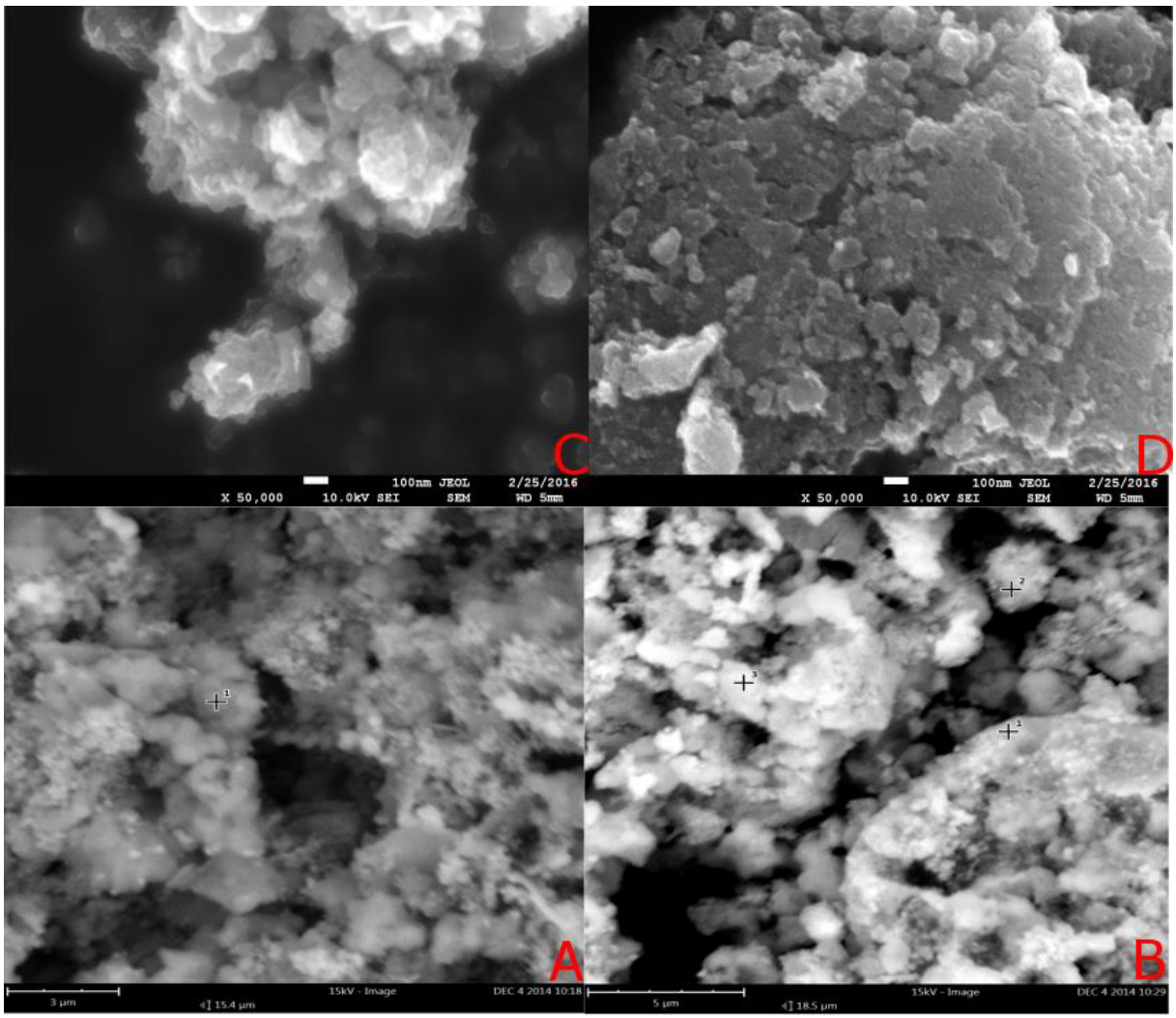

Fig. 45 TiO_2 coated particles of EXP TiO_2 samples as marked in tab.18

EDS measurement results are demonstrated in table 19. As can be observed at samples A, B, the marked positions of EDS analysis are shown as trying to observe surface of just a magnetite. In sample B the dot 2 is reported as representative of the element composition. For samples C and D analysed with JEOL JSM-7600F the map scanning was performed. As observed from SEM – EDS analysis, the aggregated particles were prepared with quite small size in case of using TIPP coating over the nanoparticles with superplasticizer use. For further analysis, the samples with low remanence turbidity (B, C, D) in aquatic environment were selected, treated without and with TIPP.

Tab. 19 Composition of analysed TiO_2 coated samples

Element (% weight)	A	B	C	D
Ti	2.9	21.2	46	24.2
Fe	62.5	10.9	17.7	38.0
O	34.7	65.1	36.2	34.9
C	0	2.8	0.2	2.9

5.3.3 XRD analysis of TiO_2 coated nanoparticles

XRD with Rietveld´s analysis was done. Results of appeared phases and their quantification for samples A – D EXP TiO_2 are given in following table:

Tab. 20 Rietveld´s analysis of phases formed.

Phase (% weight)	A	B	C	D
Anatase	26	30	74.6	84.3
Magnetite	72	70	19.9	15.7
Hematite	2		3.1	
Rutile			2.4	

With application of hydrolysed TIPP the content of TiO_2 increased significantly. When applying the ACE 40 superplasticizer the surface of particles remained consisted and formed from anatase and magnetite phases whereas the hematite and rutile appeared at surface treated with TIPP and small amount of hematite appeared when only nanomagnetite particles were coated.

5.3.4 Magnetization measurement of TiO_2 coated nanoparticles

Figure 46 shows the magnetization curve obtained for NaOH + ACE 40 synthesis as mentioned earlier in figure 40 and magnetization curve of samples C, D according to table 19. Table 21 shows obtained data from measurement.

Tab. 21 Analysis of magnetization of TiO_2 coated particles

	Synthesis 2 NaOH + 2 ml ACE 40	C	D
Saturation magnetization ($emu \cdot g^{-1}$)	19.3	11.6	10.2
Coercivity (Oe)	53.7	132.56	42.4

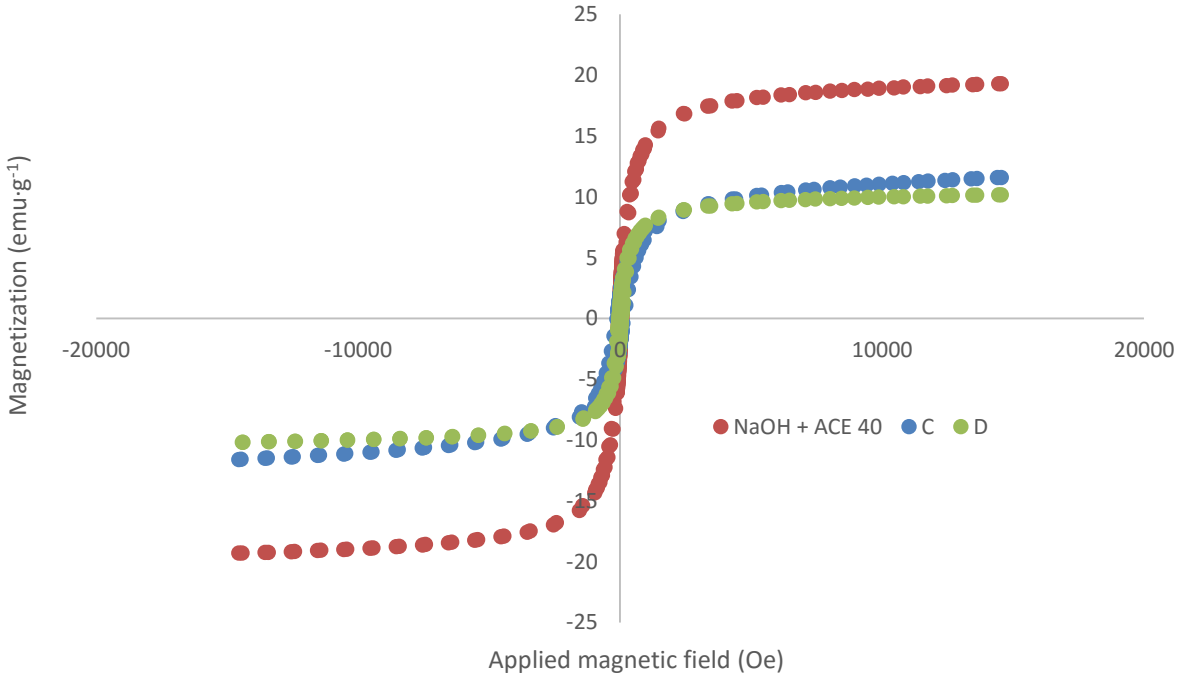

Fig. 46 Magnetization measurement of samples C, D compared to NaOH + ACE 40 magnetite nanoparticles magnetization measurement

Saturation magnetization decreased significantly when applying the TiO_2 as a result of the presence of non-magnetically active TiO_2 on the surface. The coercivity of sample C was higher than others which could be caused probably by the fact, that according to the EDS analysis, hematite phase was presented in the sample.

5.3.5 BET measurement of TiO_2 coated nanoparticles

For measurement of the specific surface by BET the particles analysed with magnetization measurement were selected. Original surface of the EXP TiO_2 together with the obtained values after the TiO_2 particles mixed with TIPP with $R = 2$ is shown in following table:

Tab. 22 Measurement of specific surface of core-shell particles

TiO_2 particles	EXP TiO_2	C	D
Specific surface area ($m^2 \cdot g^{-1}$)	354	149.9	136.8

5.3.6 DTA – TGA analysis of TiO_2 coated nanoparticles

DTA – TGA analysis was performed until 1000 °C for both samples C, D. Results are shown in figures 47 and 48.

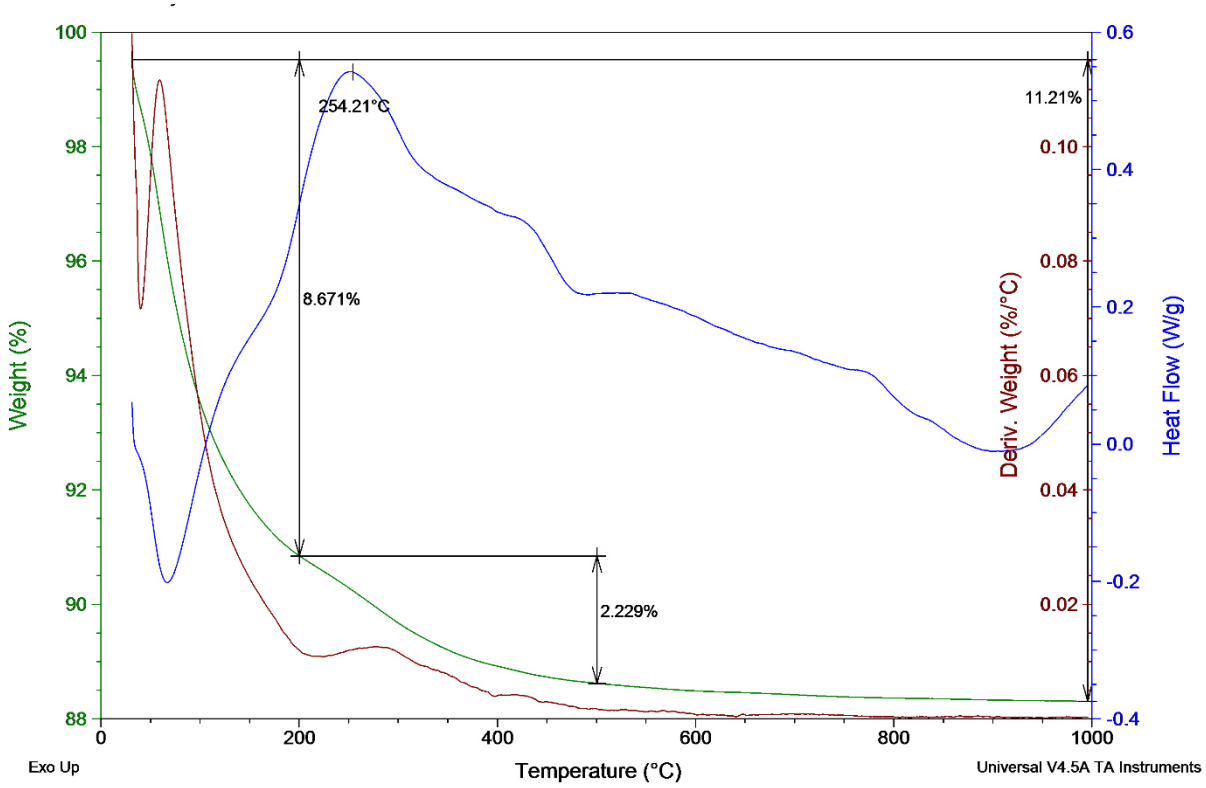

Fig. 47 DTA – TGA analysis of sample C

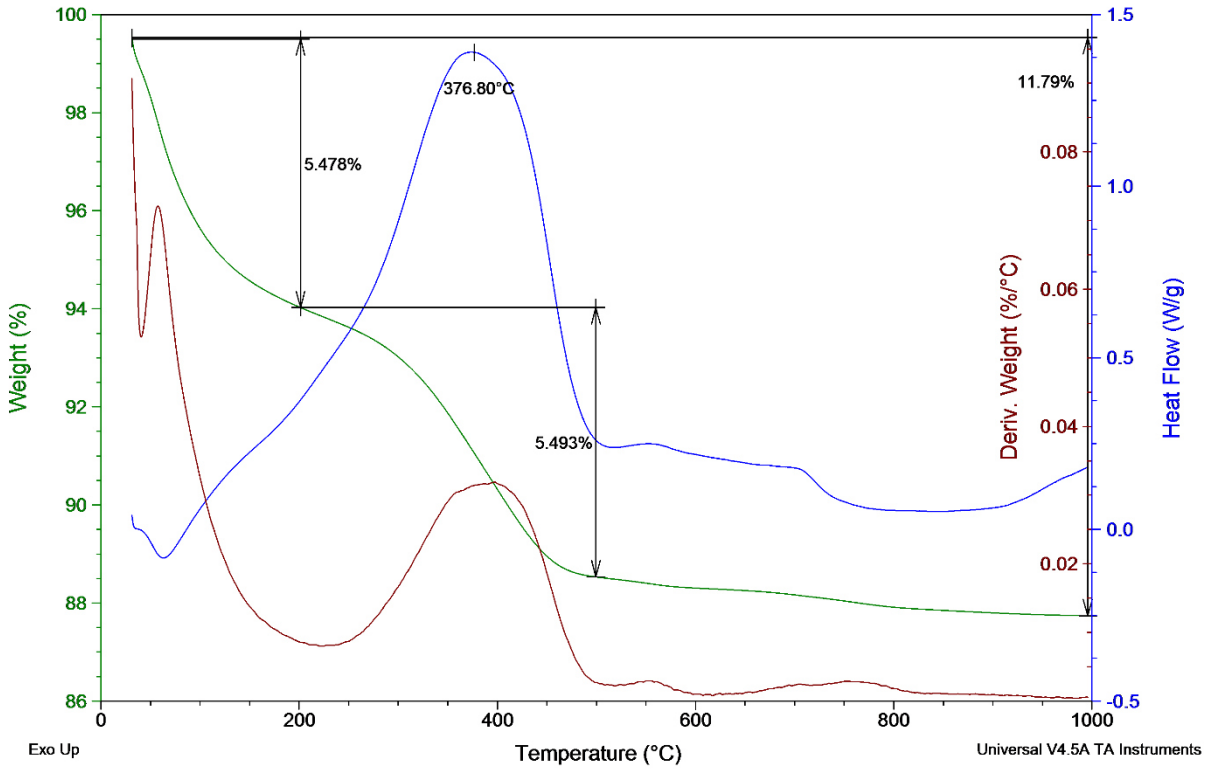

Fig. 48 DTA – TGA analysis of sample D

Carboxyl superplasticizer treated sample shows the similar behaviour as magnetite with carboxyl superplasticizer. It can be observed that in range of 200 – 500°C, the loss of 5.5 % of weight is presented together with exothermic peak of heat flow with position in 376 °C. ACE 40 untreated sample is showing much steeper loss of weight

until 200 °C (8.7%) compared to treated sample (5.5 %) followed in range 200 – 500°C with 2.2 % loss. The total loss of weight is similar for both samples (11.4%, 11.2%).

5.3.7 Band gap measurement of TiO_2 coated nanoparticles

Results of band gap measurement are demonstrated as example for the NaOH + ACE 40 + EXP TIO_2 + TIPP sample in figure 49. From linear regressions equations the band gap measurement was calculated. Table 23 contains the values of band gap width for studied core-shell materials.

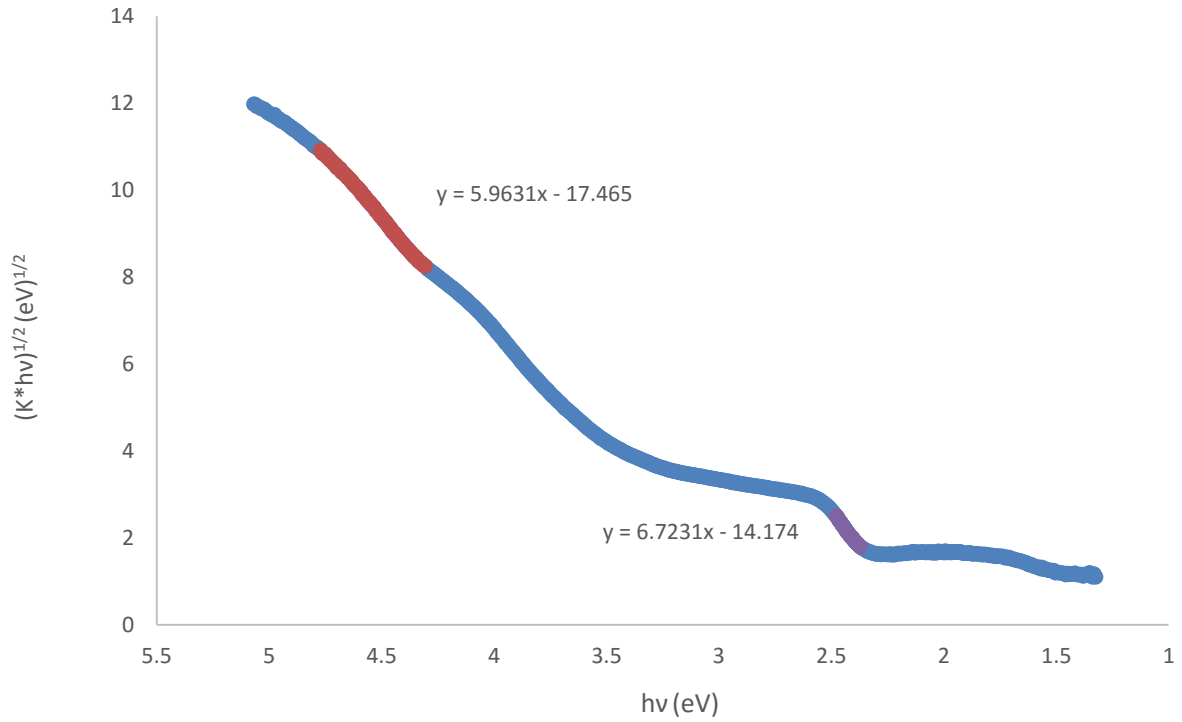

Fig. 49 The band gap estimation for the NaOH + ACE 40 + EXP TIO_2 + TIPP sample

Tab. 23 Band gap values of core-shell particles

TiO_2 particles	EXP TiO_2	C	D
Band Gap (eV)	3.2	2.3 – 3.2	2.3 – 3.2

Broad Band Gap value materials were prepared and due to the shift of the band gap into lower values, these could be attributed to the impact of Fe_3O_4 nanoparticles.

5.3.8 XPS analysis of TiO_2 coated nanoparticles

The XPS measurement of surfaces of prepared core-shell particles in order to observe what is the presence and chemical state of Fe, Ti and C on the surface of studied core-shell catalyst. Table 24 and 25 compare the data obtained, example of recorded figures by XPS measurements are shown in attachements.

Tab. 24. XPS analysis of sample C

Element / chemical state	Position (eV)	Peak area (%)
Ti 2p 3/2 TiO_2	458.4	100
C 1s C-H	284.80	66.9
C 1s C-OH	286.17	18.8
C 1s O-C=O	288.65	14.3

Tab. 25. XPS analysis of sample D

Element / chemical state	Position (eV)	Peak area (%)
Ti 2p 3/2 Ti(4)	458.57	73.9
Ti 2p 3/2 Ti(3)	457.70	26.2
C 1s C-H	284.80	66.0
C 1s C-OH	286.21	21.0
C 1s O-C=O	288.75	13.0
Fe 2p 3/2 Fe_2O_3 – 1	709.6	100

For ACE 40 coated magnetite core-shell photocatalysator, the observed presence of Fe_2O_3 on the surface was confirmed, also the appearance of non-stoichiometric TiO_2 on the surface can be observed, where mix of Ti^{3+} and Ti^{4+} is observed. Pure TiO_2 presence is observed in the sample without plasticizer treatment where also no Fe state was recorded. Little difference is observed in C species, where the C-H and C-C bindings are major and C – OH and etheric bond O-C=O are minor (together 43 – 44% area).

5.3.9 Deposition of TiO_2 on the surface of Mn-Zn ferrite

5.3.10 SEM – EDS analysis of TiO_2 coated Mn-Zn ferrite

Figure 50 is assuming the SEM analysis of pure ferrite, ferrite coated with TIPP, and mesoporous structure of PK 20 with TIPP mixture with same resolution.

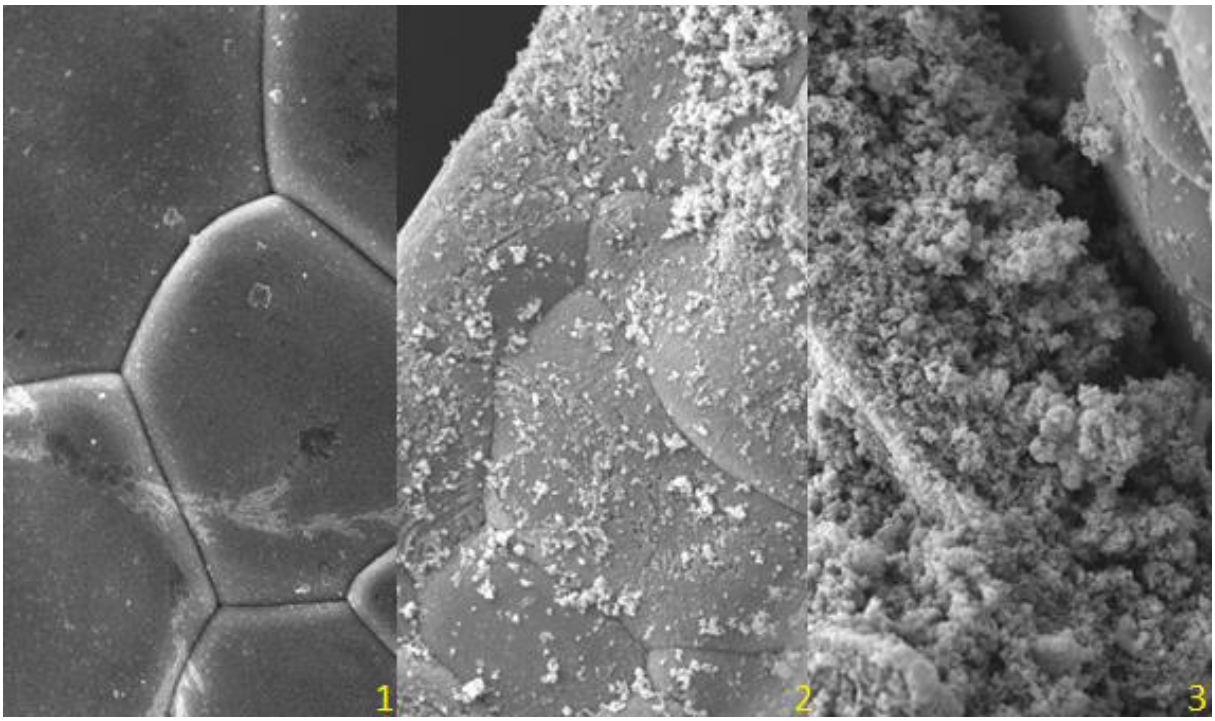

Fig. 50 Coating of ferrite, resolution 5000x (1- pure ferrite, 2- ferrite coated by TIPP hydrolysis, 3- ferrite coated with combined TIPP and PK 20 TiO_2 deposition)

As can be seen on picture, the coating of ferrite is not producing sufficient film on the surface, only some particles remained deposited. This observation was later confirmed by EDS and XRD analysis. Using PK 20 leaded to formation of thick mesoporous structure over the particles. This spongy coating was holded more firmly to the Mn- Zn ferrite structure but suffered also from the earlier mentioned releasement of TiO_2 particles into the environment. EDS analysis was performed on sample 2 in following figure:

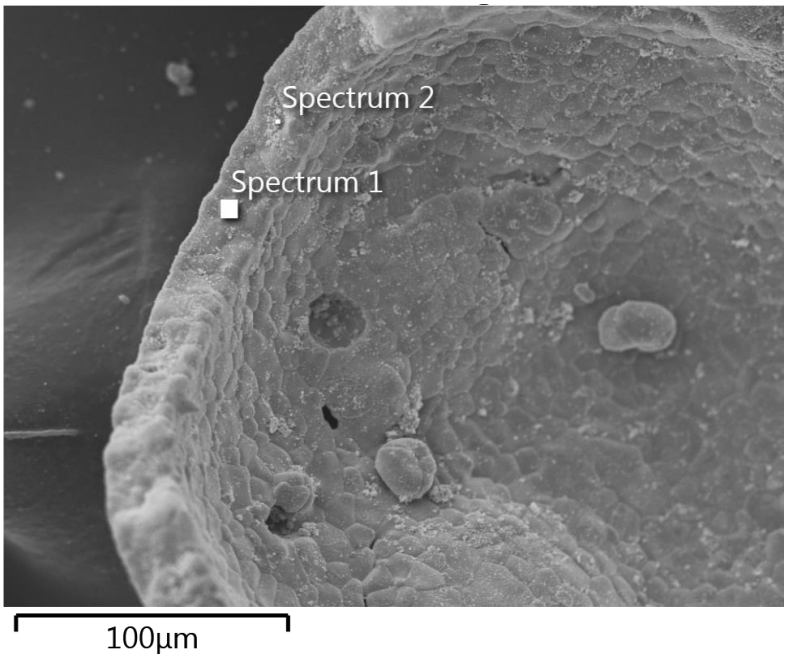

Fig. 51 SEM – EDS analysis of Mn-Zn ferrite for sample 2

Spectrum 1 of figure 51 showed 2.61 weight % of Ti and spectrum 2 performed on little adherent lumps of possible TiO_2 contained 29.9 weight % of Ti.

For better formation of desired surfaces of TiO_2 the C and Au coating was introduced on the surface of ferrite prior to coat it by TiO_2 with TIPP coating process to see, if the binding of TiO_2 on the surface improves. In following figure, the surface of Au and C sputtered ferrite (Au and C) are shown together with TiO_2 deposited on the C and Au coated surfaces of ferrite.

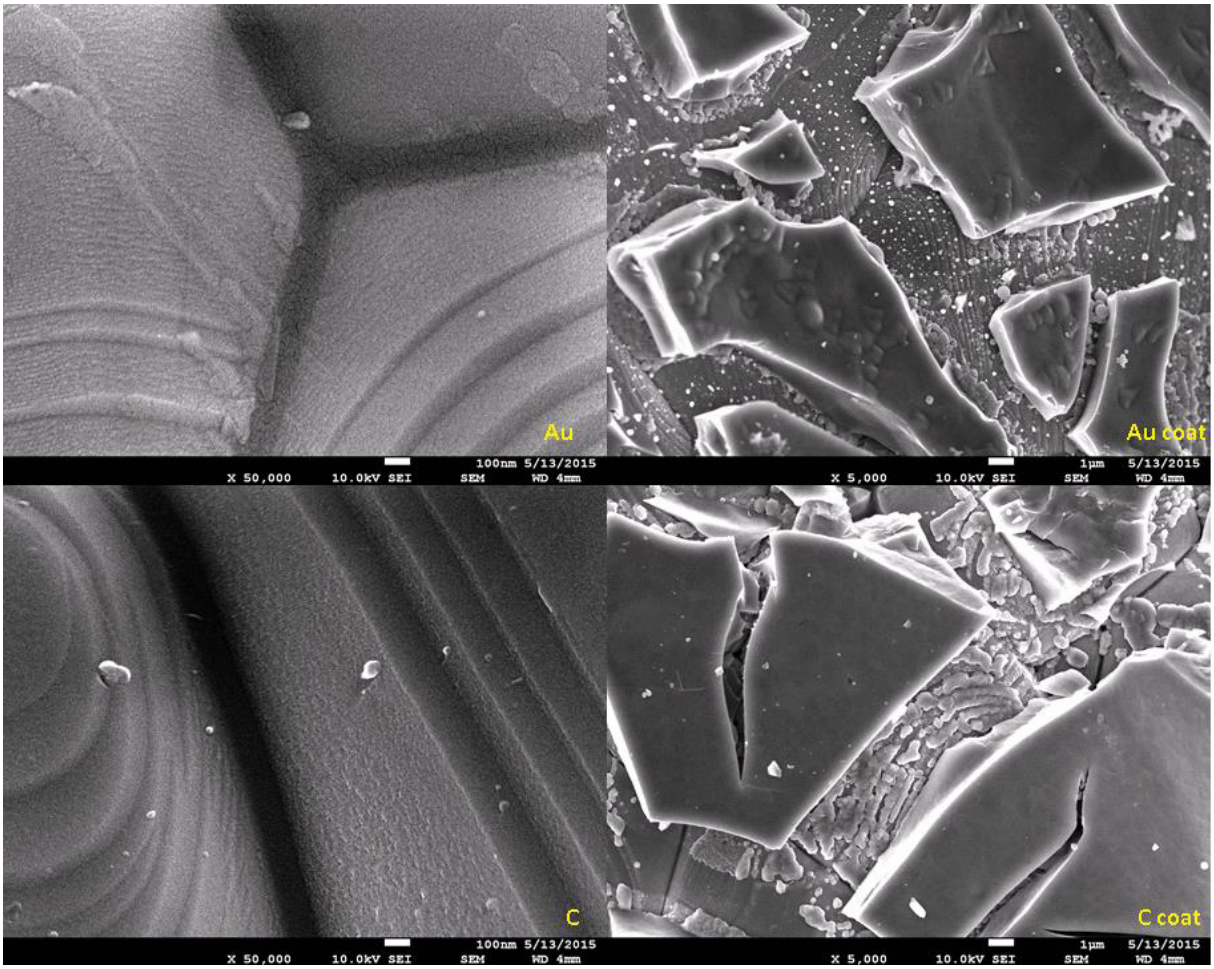

Fig. 52 TiO_2 coating of Au and C sputtered Mn-Zn ferrite surfaces

Coated particles by sputtering of C and Au showed formation of lumps of TiO_2, which was confirmed by EDS analysis. It was also observed, that after 10 sputtering sequences the formation of homogenous thin layer over the surface of Mn-Zn ferrite appeared.

5.3.11 XRD measurement of TiO_2 coated Mn-Zn Ferrite

Figure 53 shows the diffraction pattern of all TiO_2 treated Mn-Zn ferrite samples. Presented TiO_2 coatings and particles were in the form of anatase. The evaluation of crystallite size was done according to Scherrer´s formula (equation 63) and it is shown in table 26.

Tab. 26 Scherrer´s equation calculated size of crystallites for Mn-Zn ferrite TiO_2 covered samples.

Sample	2	3	Au sputtering	C sputtering
Scherrer´s formula size (nm)	60.0	13.9	68.7	63.7

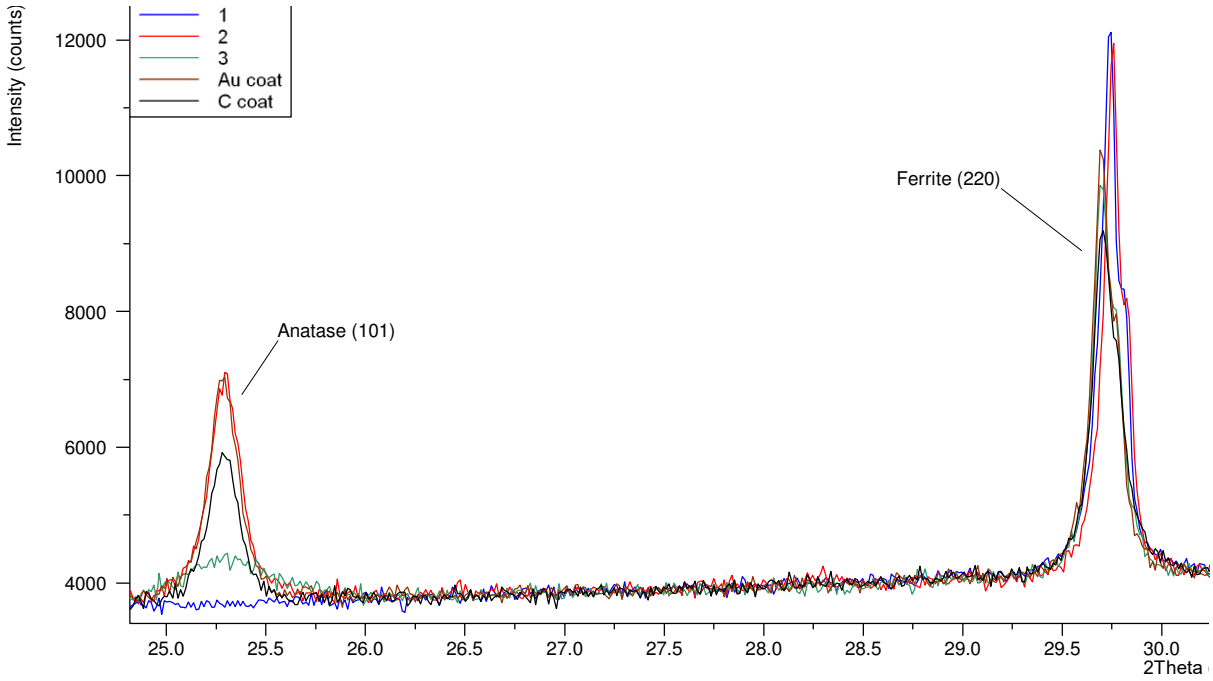

Fig. 53 XRD of produced TiO_2 covered Mn-Zn ferrite samples

Size of crystallites prepared by deposition of TiO_2 by TIPP hydrolysis on surface of ferrite is slightly varying due to the surface coated (60.0 - 68.7 nm). When using Pk 20 TiO_2 anatase particles for mesoporous structure formation, significantly lower crystallite size (13.9 nm) is obtained as the diffraction of these particles is primary obtained. EDS analysis proved the surface after applying TiO_2 directly by TIPP hydrolysis is containing significantly higher amount of Mn in % weight content than the original surface of Mn-Zn ferrite.

5.3.1 Photocatalytic decomposition of methylene blue

Testing the photocatalytic decomposition of methylene blue, it was found, that a big adsorption properties can be denoted to the use of superplasticizer for the synthesis of nanoparticles. Therefore, the photocatalytic activity was estimated for samples of nanoparticles prepared according to chapter 5.2 by synthesis 1 using the NaOH as base for precipitation, which were coated with TiO_2 anatase particles as mentioned in

chapter 5.3 with two different coating methods as described in chapter 4.4.1. In table 27 for better explanation, the methodology of samples which appear in this chapter is given with used methods of preparation.

Tab. 27 Methodology of photocatalytically tested core-shell samples

Sample	Magnetite preparation	TiO_2 application	Heat treatment
Calibration	Average values of C / C_0 obtained from all samples for photocatalytic tests during measurement in dark		
NaOH + Kronos TiO_2 + TIPP	Synthesis 1	Kronos TiO_2 dispergated in hydrolysed TIPP	370 °C in N_2 atmosphere
NaOH + Kronos TiO_2	Synthesis 1	Kronos TiO_2 dispergated in isopropanol	150 °C in oxygen atmosphere
NaOH + EXP TiO_2 + TIPP	Synthesis 1	EXP TiO_2 dispergated in hydrolysed TIPP	370 °C in N_2 atmosphere
NaOH + PK 20 TiO_2 + TIPP	Synthesis 1	PK 20 TiO_2 dispergated in hydrolysed TIPP	370 °C in N_2 atmosphere
NaOH + ACE 40 + EXP TiO_2 + TIPP	Synthesis 2	EXP TiO_2 dispergated in hydrolysed TIPP	370 °C in N_2 atmosphere

Figure 54 shows the decomposition rate as the decrease of concentration (C) of methylene blue with irradiation time compared to the initial concentration (C_0) as measured for the absorption of light at λ = 664 nm. The typical absorbance in UV spectra range of 550 – 750 nm is shown for sample NaOH + PK20 TiO_2 + TIPP in figure 55. Table 28 assumes the decomposition rate of used samples in $mol \cdot h^{-1} \cdot g^{-1}$. The highest degradation rate is observed for sample NaOH + EXP TiO_2 + TIPP.

Tab. 28 Decomposition rate of photocatalytic samples

Sample	Decomposition of MB 180 min (%)	Decomposition rate ($mol \cdot h^{-1} \cdot g^{-1}$)
NaOH + Kronos TiO_2 + TIPP	21	$3.5 \cdot 10^{-5}$
NaOH + Kronos TiO_2	33	$5.5 \cdot 10^{-5}$
NaOH + EXP TiO_2 + TIPP	40	$6.7 \cdot 10^{-5}$
NaOH + PK 20 TiO_2 + TIPP	34	$5.7 \cdot 10^{-5}$

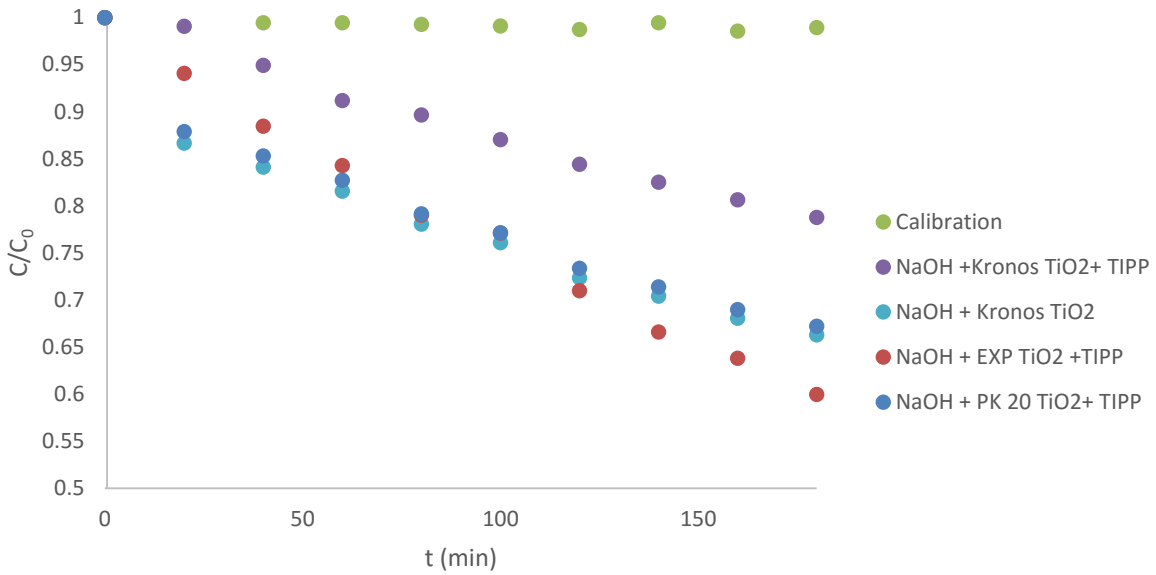

Fig. 54 The decomposition of methylene blue with core-shell magnetite samples

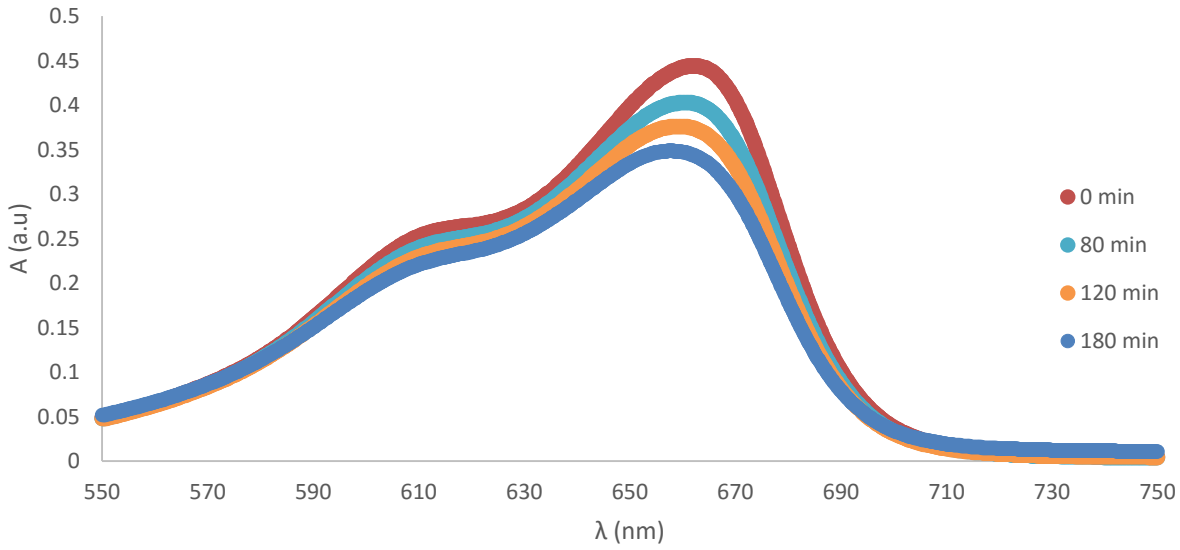

Fig. 55 Absorption spectra of core-shell powder photocatalyst with increasing time of UV irradiation (NaOH + PK 20 TiO_2 + TIPP)

The enhanced adsorption properties of selected NaOH + ACE 40 + EXP TiO_2 + TIPP sample are shown in the figure 56, for comparison the measured data for 180 min UV decomposition of the sample NaOH EXP TiO_2 + TIPP are included in figure. It can be observed, that adsorption of methylene blue is significantly increased with the use of the ACE 40 superplasticizer during precipitation of nanoparticles from the Mohr´s salt solution.

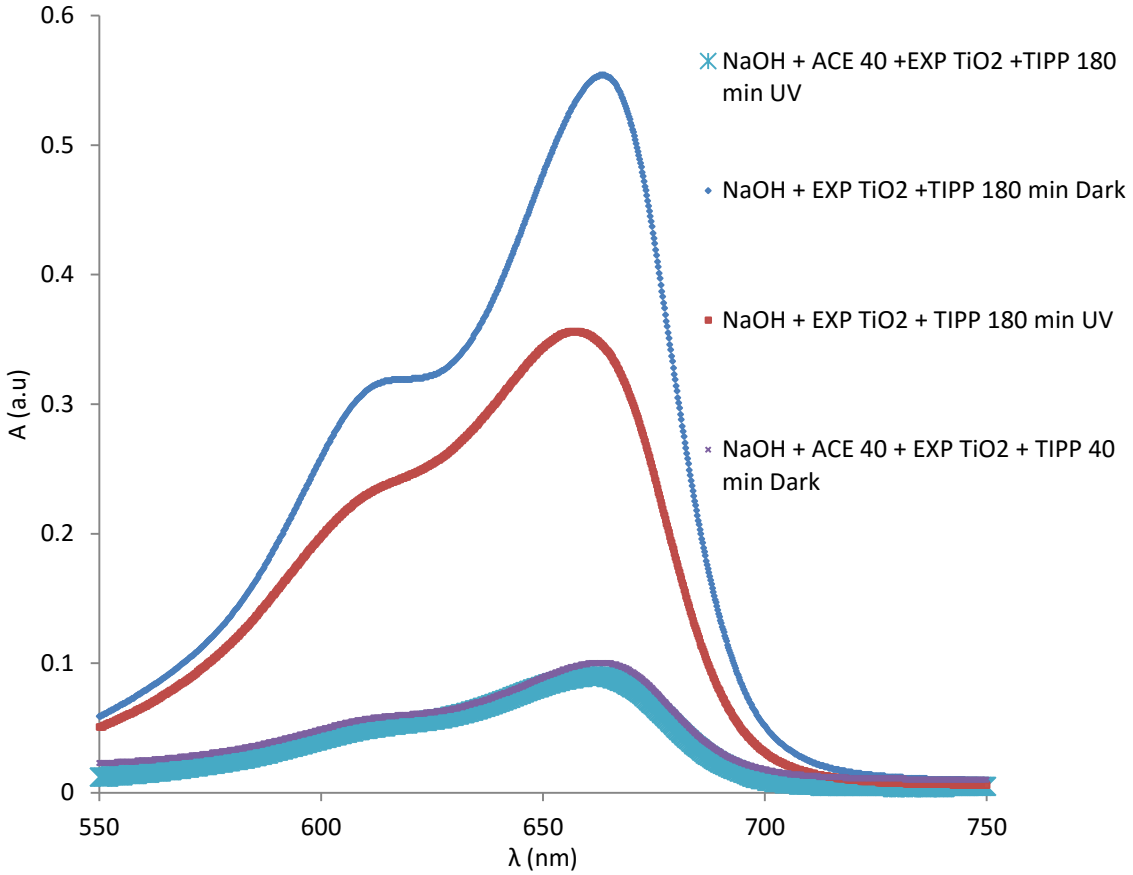

Fig. 56 Adsorption properties of EXP TiO_2 samples with use of ACE 40

Little difference of absorption spectra maxima for irradiation decomposition and for the adsorption can be observed. When only adsorption is presented (typically for the dark measured sample for 180 min of mixing) the adsorption maxima spectra remains same (664 nm). If irradiated and photocatalytic decomposition is happening, then the change in overall spectra is observed and the maxima of absorption of light changes (655 – 657 nm). Decrease of absorbance of methylene blue upon photocatalytic decomposition can be observed in absorbance wavelength range 570 – 720 nm.

5.3.2 Photocatalytic decomposition of ethanolic and isopropanolic vapors

For measurement in the experimental reactor, 3 samples of ferrites were selected as mentioned in the chapter 5.3.9 samples 1, 2, 3. These were holded in reactor by magnetic force and the photocatalytic decomposition of the ethanolic and isopropanolic vapors were evaluated by collecting the FTIR spectra of the circulating vapors. In figures 57 – 59 the typical observed spectra changes are evaluated in 2D FTIR figures with showing intensity of recorded spectra by color change with the same color range. The red cross marks the position of the CO_2 IR absorbance peak.

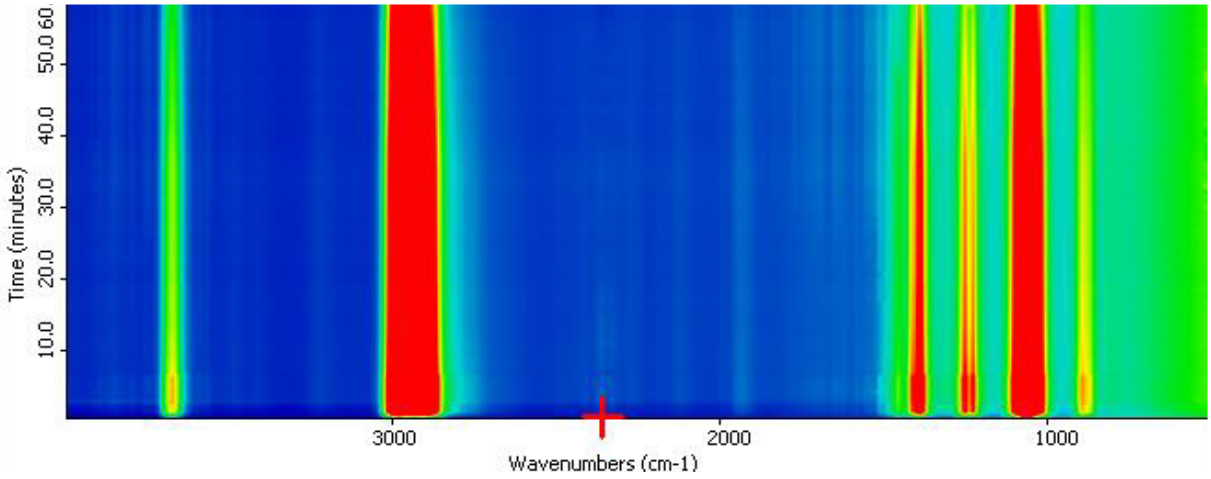

Fig. 57. Ferrite decomposition of ethanolic vapors in UV

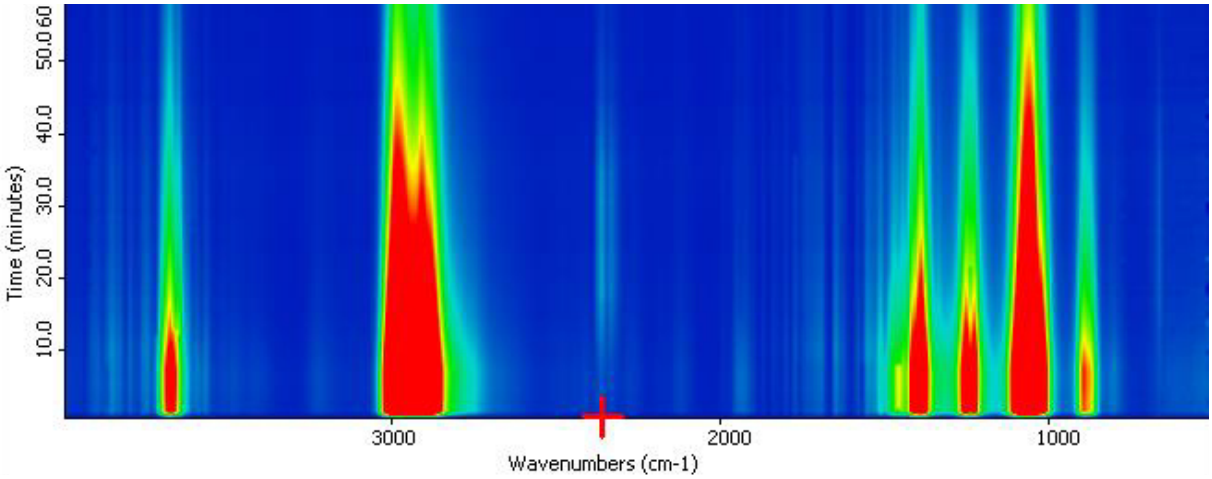

Fig. 58. Ferrite coated by TIPP hydrolysis decomposition of ethanolic vapors

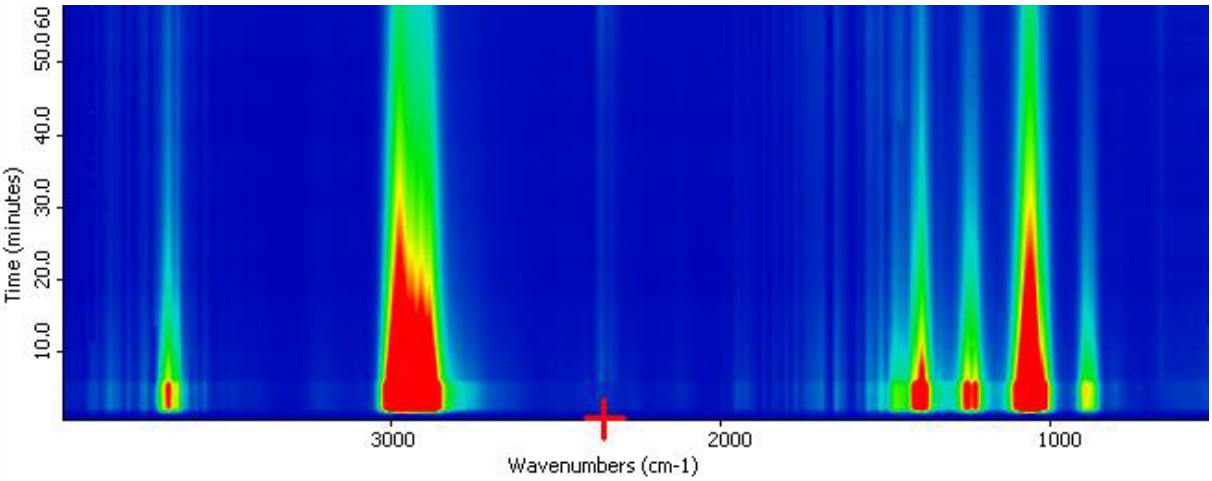

Fig. 59 Ferrite coated with PK 20 TiO_2 + TIPP hydrolysis decomposition of ethanolic vapors

For further comparative analysis of the photocatalytic efficiency of TiO_2 ferrite coated particles the maximum absorbance in IR spectra was selected, plotting the recorded FTIR spectra of ethanolic and isopropanolic vapors in following figure:

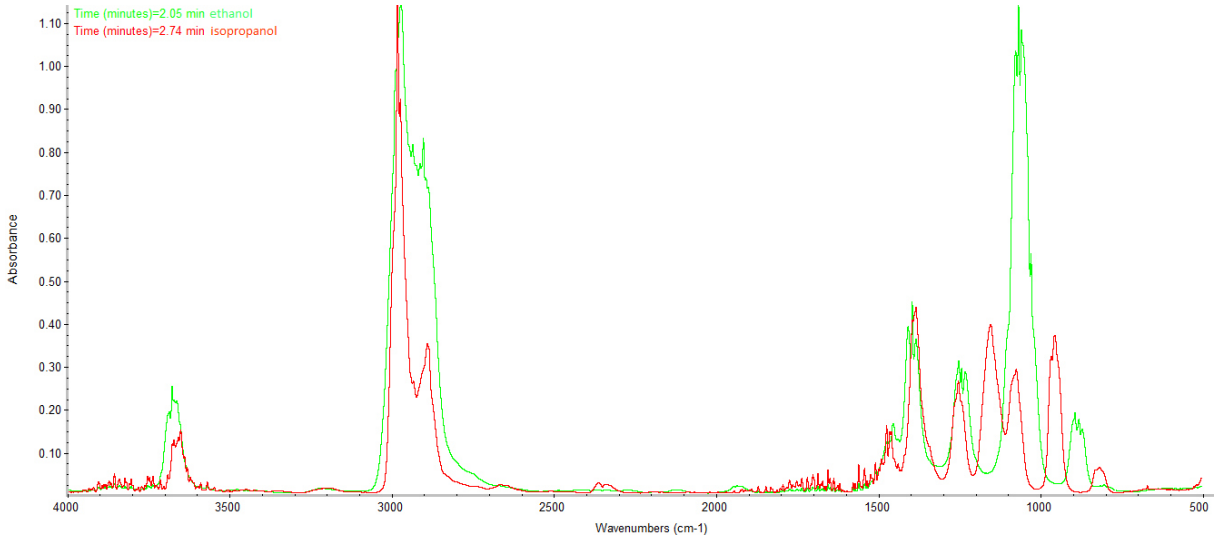

Fig. 60 FTIR spectra of isopropanolic and ethanolic vapors

FTIR spectra shows same intensity for absorbance peak at 2 974 cm^{-1}. The decrease of absorbance to 50% of original size after UV lamp was turned on was recorded as relative half time of decomposition ($t_{1/2}$) which is shown in the following table:

Tab. 29 Estimation of relative half time of decomposition $t_{1/2}$

Sample	Pure ferrite	Ferrite coated by TIPP	Ferrite coated with PK 20 TIPP
$t_{1/2}$ ethanol (min)	$t_{1/2}$ >60.0	10.5	10.0
$t_{1/2}$ isopropanol (min)	$t_{1/2}$ >60.0	37.5	22.9

In figure 61 the absorbance with time for decomposition of isopropanolic vapors for ferrite with PK 20 TiO_2 + TIPP hydrolysis is shown together with data for $t_{1/2}$ estimation.

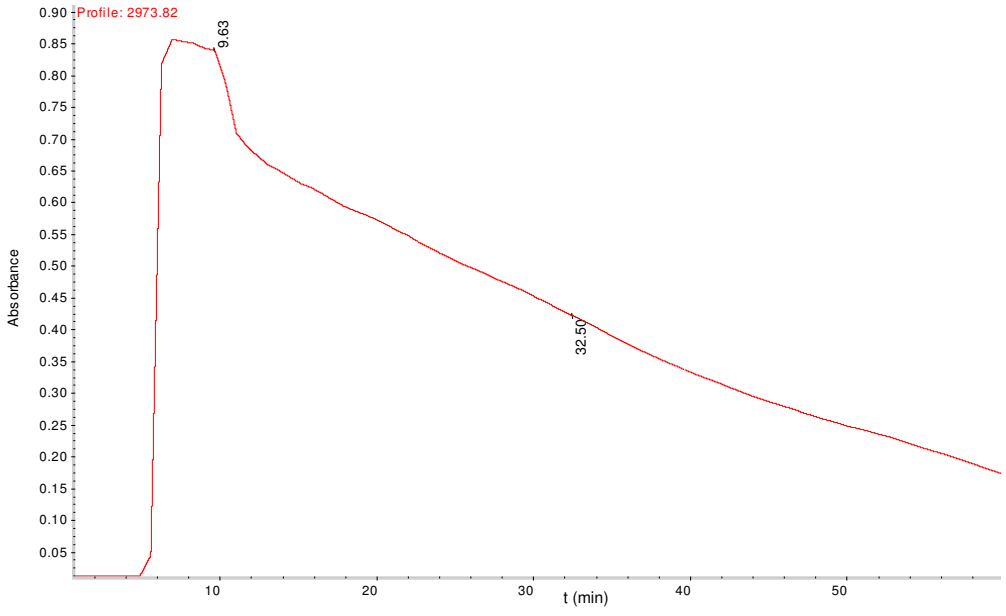

Fig. 61 Evaluation of $t_{1/2}$ for sample PK 20 TiO_2 + TIPP hydrolysis coating

Concluding the obtained data, it is possible to observe the enhancement in decomposition of the ethanolic vapor as the function of absorbance decrease in time. The development of small amount of CO_2 can be observed for TiO_2 coated ferrite particles.

As can be seen the combined PK 20 TiO_2 + TIPP hydrolysis coated ferrite exhibits the relatively highest photocatalytic decomposition as the recorded $t_{1/2}$ values are smallest. In case of ferrite without any surface treatment, the $t_{1/2}$ values couldn´t be obtained as the halftime of decomposition was not reached in 60 min when measurement proceeded.

5.3.3 Conclusion of the chapter

For deposition of photocatalytic active TiO_2 in form of anatase, the selected prepared magnetite nanoparticles were used with and without treatment of the surface by polycarboxylic superplasticizer. It was found, that the remanence turbidity is significantly reduced, using the nanoparticles of magnetite treated with superplasticizer or coated by TiO_2 with hydrolysis of TIPP with $R = 2$. The method using the dispersed nanoparticles in hydrolysed Ti-alkoxide mixture is most suitable for preparing the core-shell particles starting with the nanoparticles of magnetite. Particles with highest content of TiO_2 on the surface (% weight) according to performed Rietveld´s analysis were selected for further testing. These particles had been treated by combined method of hydrolysis of Ti-alkoxides with dispersed nanoparticles of TiO_2.

Magnetization measurement performed on particles with high content of TiO_2 and low remanence turbidity, showed decrease of saturation magnetization. Specific surface area measurement showed similar results for particles treated with polycarboxylic superplasticizer coated nanoparticles of magnetite prior to deposition of either only TiO_2 anatase nanoparticles or TiO_2 anatase nanoparticles dispersed in hydrolysed TIPP with $R = 2$.

DTA – TGA performed on prepared core-shell nanoparticles showed the differences among prepared particles as contributing to the earlier measurement in chapter 5.2.3. The superplasticizer remained during the deposition of TiO_2 by different techniques as mentioned in chapter 4.4.1 chemisorbed on the surface of magnetite particles which leaded to weight loss in same temperature range as in case of magnetite synthetized with presence of plasticizer

Measurement of band gap showed that a broad band gap core-shell powder photocatalysts were prepared with band gap range 2.3 – 3.2. This advantageous feature can contribute to their photocatalytic performance. Broadening of band gap was caused by the nanoparticles of magnetite. XPS analysis of prepared samples as identified in chapter 5.3.8 was done in order to estimate the surface states of elements. It was found that with presence of the superplasticizer in synthesis, the TiO_2 is affected and can be devided into Ti^{3+} and Ti^{4+} states. Fe was found in case of the superplasticizer synthesis performed coating procedure and its state was fully oxidized to Fe_2O_3 on the surface.

Deposition of TiO_2 on the Mn-Zn ferrite macroscopic particles was done by methods mentioned in chapter 4.4.2. It was observed that for both methods the spongy coating

of the ferrites with lumps was received. Even though the TIPP hydrolysis with TiO_2 nanoparticles coating was adhering better, still the ossibility of release of the TiO_2 nanoparticles into the environment was high. Carbon and Au sputtering coating was evidenced to be suitable treatment of ferrite surface prior to TiO_2 deposition by Ti-alkoxide hydrolysis as the surface was homogenously coated with C and Au after 10 sputtering sequences and EDS analysis on deposited TiO_2 by formentioned method showed just crackings in the surface of TiO_2 coating due to the contraction during heat – treatement of ferrite in order to receive crystallic anatase phase. XRD analysis revealed the anatase deposited on ferrite and when using the TiO_2 nanoparticles in hydrolysed TIPP mixture, the very small size of crystallites measured by Scherrer´s formula was observed contributing to the used dimensions of TiO_2 nanoparticles. With narrow distribution of particle size and due to some other advantages as for example possibility of high treatment temperature, the deposition of mesoporous highly active TiO_2 surface on ferrite surface could pose the broad spectrum of uses of such compounds.

Photocatalytic activity of prepared TiO_2 core-shell coated magnetic nanoparticles was estimated by decomposition of methylene blue dye coloring. The decomposition was done using mixing photocatalytic decomposition method according to DIN 5298: Photocatalytic activity of surfaces - Determination of photocatalytic activity by degradation of methylene blue [149], which was adapted for the powder photocatalytic activity estimation as defined in thesis of Svava Daviðsdóttir [148]. According to obtained results of photocatalytic activity measurement all prepared particles were photocatalytically active and decomposed the methylene blue with highest photocatalytic activity received for nanoparticles of magnetite coated with modified deposition method of TiO_2 nanoparticles with hydrolysed TIPP mixture as described in chapter 4.4.1. When using nanoparticles synthetized with the polycarboxylic superplasticizer and EXP TiO_2 nanoparticles together with hydrolysed TIPP deposition, the enhanced adsorption was observed. Especially for sample NaOH + ACE 40 + EXP TiO_2 + TIPP the adsorptive behaviour was enormous as 1 mg of this powdered photocatalyst was able to decolorize in 40 minutes the studied solution of methylene blue. Moreover, it was found that even with such amount of methylene blue on its surface, the photocatalytic reaction was running on its surface as the spectral absorption maxima of the irradiated methylene blue solution shifted with UV decomposition. Taking into account such properties, the very promising core-shell magnetically active candidate for future decomposition studies was prepared.

Photocatalytic decomposition of ethanolic and isopropanolic vapors was done in experimental reactor with magnetically holded photocatalytic bed consisted of TiO_2 supported on the Mn-Zn ferrite surface with FTIR evaluation in closed loop system. [150] Due to the fact, that no products of decomposition of vapors were observed, except a bit of the CO_2 evolution, relative comparison of photocatalytic activity was used. Photocatalytic activity was estimated as time needed ($t_{1/2}$) for the reduction of the absorbance in identified maxima absorbance peak positioned at 2 974 cm^{-1} to 50% of starting value. The particles containing higher amount of TiO_2 were relatively more effective against the decomposition of solvent vapors, using forementioned method of photocatalytic evaluation.

6 Conclusion

Evaluation of the impact of conditions of the hydrolysis of Ti-alkoxides on properties of formed hydrolysates was done. The study confirmed that water concentration, especially water to alkoxide ratio *R* and temperature conditions of hydrolysis reactions, affect the kinetics of Ti-alkoxide hydrolysates formation and their properties. By turbidimetric studies of hydrolysis kinetics, the induction time was evaluated for TIETH, TIPP and TIBUT alkoxides dissolved in ethanol, isopropanol and n-butanol. Furthermore, the formation of crystallite phases in hydrolysed Ti-isopropoxide isopropanolic mixtures with low content of water reported as hydrolysis molar ratio ($R = 0.5$) was confirmed. Their formation was supported with the temperature treatment at 50 °C or aging of hydrolysed mixture.

DTA – TGA analysis confirmed the impact of water content during hydrolysis on the crystallization temperatures. Higher crystallization temperature of anatase phase with increasing of *R* during hydrolysis was observed. The study found, that amount of chemisorbed solvent in prepared hydrolysates is *R* dependent. For low values of *R*, the higher amount of solvent is chemisorbed in formed hydrolysates structure. With increasement of solvent chemisorbed, the reduction of solvent presence was obtained.

Calculating the crystallites size of anatase phase formed with use of Scherrer´s equation from the XRD measurements revealed that with higher content of chemisorbed solvents the size of crystallites decreased. This finding can be attributed to large imperfections and defects in the structure of such formed crystallites rather, than to the claim that very small particles were received. The observation of XRD measurement in atmospheric conditions in temperate cell with increasing temperature, showed according to Scherer´s formula size growth of imperfect crystallites with higher amount of chemisorbed solvent happened with increasing temperature treatment whereas crystallites formed from hydrolysates with lover content of chemisorbed solvent preserved their original size or exhibited smaller growth of the size. Moreover, higher specific surface area was obtained for the prepared crystallized anatase nanoparticles by heat treatment of hydrolysates with higher *R* during synthesis and lower amount of chemisorbed solvent.

Synthesis of magnetite nanoparticles by simple precipitation of magnetite nanoparticles from Mohr´s salt solution by strong and moderate bases (NaOH, Na_2CO_3) was done. Conditions of the precipitation considering the temperature and the modification by surface-active compounds were examined. It was found that precipitation reaction is temperature depended, showing no evolution of magnetite nanoparticles at low temperature of 0 °C and performing the highest precipitation rate using boiling solutions. Quite interestingly, the formation of earlier observed 2D shaped particles was observed at temperature range around 60°C. It is possible that needles of presented goethite phase, which presence was confirmed by XRD and SEM analysis, are formed during precipitation reactions converted into the magnetite and are able to drive the magnetite evolution direction.

Conductivity and pH measurements were done in order to estimate range of pH and conductivity in which the precipitation occurs. It was found that application of surface modyfying compound consisted of polycarboxylic ether based superplasticizer ACE 40

had impact on the reaction intermediates formation, but showed negligible impact on the pH and conductivity range during precipitation of magnetite. With usage of ACE 40 formation of unknown magnetically active crystalline phase was discovered, showing no match to any known diffraction pattern respecting its elemental composition determined by EDS analysis. This phase consisted of the very first magnetically active compounds formed during precipitation with NaOH and during further precipitation was later in reaction transformed into the magnetite nanoparticles. Using the ACE 40 during precipitation leaded to lower size of agglomerates of magnetite nanoparticles.

Prepared magnetite nanoparticles were starting material for the deposition of TiO_2 in photocatalytic form of anatase on their surface. Two deposition techniques were examined using either hydrolysis of TIPP with $R = 2$, or combined method with selected TiO_2 anatase nanoparticles dispersed by ultrasonification in hydrolysed TIPP. Core-shell powder photocatalysts with high specific surface area (137 – 150 $m^2 \cdot g^{-1}$) and broader band gap value (2.3 – 3.2 eV) were prepared. Photocatalytic measurement of methylene blue decomposition showed that particles are having both the photocatalytic properties as well as very high adsorptive properties. Taking into account such properties, prepared core-shell nanoparticles are very promising candidates for future decomposition studies work.

Mn-Zn ferrite with macroscopic dimensions with deposited TiO_2 in anatase form was prepared by either coating of its surface by hydrolysed Ti-alkoxide or by dispergating the anatase nanoparticles in hydrolysed Ti-alkoxide. Problems with not adhering lumps of TiO_2 coating were observed, reduced when using the hydrolysed Ti-alkoxide deposition with anatase nanoparticles. Evaluation of impact of sputtering of the Au and C layers onto the ferrite surface prior to coating it by hydrolysed TIPP was done. It was observed, that sputtered coating helped to the adherence of the anatase layer deposited by hydrolysis of TIPP on the modified surface of ferrite showing only crackings of layer due to the heat-treatment. Photocatalytic decomposition of solvents vapors was done on the photochemical reactor.

To conclude, magnetic nanoparticles and microscale compounds with enhanced adsorptive and photocatalytic properties are extensively studied with various methods. Increasing knowledge in this area leads to preparation of novel materials with extraordinary properties. In proposed thesis, the development of novel materials have been done together with the identification of some previously unknown processes.

7 REFERENCES

[1] FUJISHIMA, A., HONDA, K., KIKUCHI, S. Photosensitized electrolytic oxidation on semiconducting n-type TiO_2 electrode. *Kogyo Kagaku Zasshi*, 1969, Vol. 72, p. 108 (in Japanese)

[2] SIMONS, P. Y., DACHILLE, F. The structure of TiO_2 II, a high-pressure phase of TiO_2. *Acta Crystallographica*, 1967, Vol. 23, No. 2, p. 334

[3] SATO, H., ENDO, S., SUGIYAMA, M., KIKEGAWA, T., SHIMOMURA, O., KUSABA, K. Baddeleyite-Type High-Pressure Phase of TiO_2. *Science*, 1991, Vol. 25, p. 786

[4] DUBROVINSKAIA, N. A., DUBROVINSKY, L. S., AHUJA, R., PROKOPENKO, V. B. at all. Experimental and Theoretical Identification of a New High-Pressure TiO_2 Polymorph. *Physical Review Letters*, 2001, Vol. 87, Issue 27

[5] DUBROVINSKY, L. S., DUBROVINSKAIA, N. A., SWAMY, V., MUSCAT, J., HARRISON, N. M. at all. Materials science: The hardest known oxide. *Nature*, 2001, Vol. 410, p. 653

[6] MATTESINI, M., ALMEIDA, J. S., DUBROVINSKY, L. S., DUBROVINSKAIA, N. A., JOHANSSON, B., AHUJA R. High-pressure and high-temperature synthesis of the cubic TiO_2 polymorph. Physical Review B. 2004, Vol. 70, Issue 21, no 212101

[7] MARCHAND, R., BROHAN. L., TOURNOUX. M. A new form of titanium dioxide and the potassium octatitanate $K_2Ti_8O_{17}$. *Materials Research Bulletin*, 1980, Vol. 15, Issue 8, p. 1129

[8] LATROCHE, M., BROHAN, L., MARCHAND, R., TOURNOUX, M. New hollandite oxides: TiO_2 (H) and $K_{0.06}TiO_2$. *Journal of Solid State Chemistry*, 1989, Vol. 1, p. 78

[9] AKIMOTO, J., GOTOH, Y., OOSAWA, Y., NONOSE, N., KUMAGAI, T. at all. Topotactic Oxidation of Ramsdellite-Type $Li_{0.5}TiO_2$, a New Polymorph of Titanium Dioxide: TiO_2(R). *Journal of Solid State Chemistry*, 1994, Vol. 113, Issue 1, p. 27

[10] WALDNER, P. (1999). Modelling of oxygen solubility in titanium. *Scripta Materialia*, 1999, Vol. 40, Issue 8, p. 969

[11] LEE, B. J. Thermodynamic Evaluation of the Ti-O Binary System *Journal of Korean Institute of Metals and Materials*, 1994, Vol. 32, p. 869

[12] CANCAREVIC, M., ZINKEVICH, M., ALDINGER, F. (2007). Thermodynamic description of the Ti-O system using the associate model for the liquid phase. *Calphad: Computer Coupling of Phase Diagrams and Thermochemistry*, 2007, Vol. 31, Issue 3, p. 330

[13] WALDNER, P., ERIKSSON, G. Thermodynamic modelling of the system titanium-oxygen. *Calphad: Computer Coupling of Phase Diagrams and Thermochemistry*, 1999, Vol. 23, Issue 2, p. 189

[14] BY A.H. WILSON. The theory of metals. 2nd ed. Cambridge: Cambridge University Press, 2011. ISBN 0521279003.

[15] FOX, M. A., DULAY, M. T. Heterogeneous Photocatalysis. *Chemical Reviews*, 1993, Vol. 93, Issue 1, p. 341

[16] PARAMASIVAM, I., JHA, H., LIU, N., SCHMUKI, P. A Review of Photocatalysis using Self-organized TiO_2 Nanotubes and Other Ordered Oxide Nanostructures. *Small*, 2012; Vol. 8, Issue 20, p. 3073

[17] LINSEBIGLER, A. L., LU, G. Q., YATES, J. T. Photocatalysis on TiO_2 Surfaces-Principles, Mechanisms, and Selected Results. *Chemical Reviews*, 1995, Vol. 95, Issue 3, p. 735

[18] KRISHNAN RAJESHWAR. Fundamentals of Semiconductor Electrochemistry and Photoelectrochemistry. Encyclopedia of Electrochemistry [online]. Weinheim, Germany: Wiley-VCH Verlag GmbH & Co. KGaA, 2007,ISB N 3527610421.

[19] FINKLEA, Harry O. Semiconductor electrodes. New York: Elsevier, 1988. ISBN 0444429263.

[20] BESSEGATO, Guilherme Garcia, Thaís Tasso GUARALDO a Maria Valnice Boldrin ZANONI. Enhancement of Photoelectrocatalysis Efficiency by Using Nanostructured Electrodes. *Modern Electrochemical Methods in Nano, Surface and Corrosion Science* [online]. InTech, 2014 [cit. 2016-07-26]. ISBN 978-953-51-1586-1. Available from: http://www.intechopen.com/books/modern-electrochemical-methods-in-nano-surface-and-corrosion-science/enhancement-of-photoelectrocatalysis-efficiency-by-using-nanostructured-electrodes

[21] WU, W., JIANG, C., ROY, V. A. L. Recent Progress in Magnetic Iron Oxide Semiconductor Composite Nanomaterials as Promising Photocatalysts. *Nanoscale*, 2014, Vol. 7, Issue 1, p. 38

[22] HENDERSON, M. A. A surface science perspective on TiO_2 photocatalysis, *Surface Science Reports*, 2011, Vol. 66, p. 185

[23] SCHAUB, R., WAHLSTORM, E., RONNAU, A., LAEGSGAARD, E., STENSGAARD, I. at all. Oxygen-mediated diffusion of oxygen vacancies on the TiO_2, (110) surface, *Science*, 2003, Vol. 299, p. 377

[24] XIONG, Liang-Bin, Jia-Lin LI, Bo YANG a Ying YU. Ti 3 + in the Surface of Titanium Dioxide: Generation, Properties and Photocatalytic Application. Journal of Nanomaterials [online]. 2012, 2012, 1-13 [cit. 2016-07-26]. available from: http://www.hindawi.com/journals/jnm/2012/831524/

[25] DIEBOLD, U. The surface science of titanium dioxide. *Surface Science Reports*, 2003, Vol. 48, No. 5-8, p. 53

[26] SHIRAGAMI, T., PAC, C., YANAGIDA, S. Nonmetallised CdS-catalysed photoreduction of aromatic ketones to alcohols and/or pinacols. *Journal of Chemical Society, Chemical Communications,* 1989, Issue 13, p. 831

[27] DUNN, W. W., AIKAWA, Y., BARD, A. J. Characterization of particulate titanium dioxide photocatalysts by photoelectrophoretic and electrochemical measurements. *Journal of the American Chemical Society,* 1981, Vol. 103, p. 3456

[28] SERPONE, Nick. *Photocatalysis: Fundamentals and applications*. New York: John Wiley and Sons, 1989. ISBN 0-471-62603-1

[29] BARTEAU, M. A. Site Requirements of Reactions on Oxide Surfaces. Journal of Vacuum Science & Technology A. 1993, Vol. 11, p. 2162

[30] LIU, G., YU, J. C., Lu, J. C., CHENG, H. M. Crystal facet engineering of semiconductor photocatalysts: motivations, advances and unique properties. *Chemical Communications,* 2011, Vol. 47, p. 6763

[31] OHNO, T., SARUKAWA, K., MATSUMURA, M. Crystal faces of rutile and anatase TiO_2 particles and their roles in photocatalytic reactions. *New Journal of* Chemistry, 2002, Vol 26, p. 1167

[32] LI, R., ZHANG, F., WANG, D., YANG, J., LI, M. at all. Spatial separation of photogenerated electrons and holes among {010} and {110} crystal facetsof $BiVO_4$. *Nature Communications*, 2013, Vol. 4, p. 1432

[33] LITTER, M. I. Heterogeneous photocatalysis: Transition metal ions in photocatalytic systems. *Applied Catalysis B: Environmental*, 1999, Vol. 23, Issue 2-3, p. 89

[34] MATTHEW, R. W. Hydroxylation reactions induced by near-ultraviolet photolysis of aqueous titanium dioxide suspensions. *JJournal of the Chemical Society, Faraday Transactions 1: Physical Chemistry in Condensed Phases*. 1984, Vol. 80, p.457

[35] PICHAT, P., AL-SAYYED, G., DÓLIVIERA, J-C. Semiconductor-sensitized photodegradation of 4-chlorophenol in water. *Journal of Photochemistry and Photobiology A: Chemistry*. 1991, Vol. 58, p.99

[36] SCLAFANI, A., PALMIEANO, L., SCHIAVELLO, M. J. Influence of the preparation methods of titanium dioxide on the photocatalytic degradation of phenol in aqueous dispersion. *Journal of Physical Chemistry*, 1990, Vol. 94, p. 829.

[37] FOX, M. A., ABDEL-WAHAB, A. A. Photocatalytic oxidation of multifunctional organic molecules. The effect of an intramolecular aryl thioether group on the semiconductor-mediated oxidation/dehydrogenation of a primary aliphatic alcohol. *Journal of Catalysis*, 1990, Vol. 126, Issue 2, p. 693

[38] HASHIMOTO, K., IRIE, H., FUJISHIMA, A. TiO_2 Photocatalysis : A Historical Overview and Future Prospects. *Japanese Journal of Applied Physics*, 2006, Vol. 44, Issue 12, p. 8269

[39] WANG, R., HASHIMOTO, K., FUJISHIMA, A., CHIKUNI, M., KOJIMA, E. at all. Light-induced amphiphilic surfaces. *Nature*, 1997, Vol. 388, p. 431

[40] WANG, R., HASHIMOTO, K., FUJISHIMA, A., CHIKU-NI, M., KOJIMA, E. at all. Photogeneration of highly amphiphilic TiO_2 surfaces. *Advanced Materials,* 1998, Vol. 10, Issure 2, p. 135

[41] YU, J. G., ZHAO, X. J. Effect of surface microstructure on the super-hydrophilic property of the sol-gel derived porous TiO_2 thin films. *Journal of Materials Science Letters,* 2001, Vol. 20, p. 671

[42] SAKAI, N., FUJISHIMA, A., WATANABE, T., HASHIMOTO, K. Quantitative Evaluation of the Photoinduced Hydrophilic Conversion Properties of TiO2 Thin Film Surfaces by the Reciprocal of Contact Angle. *Journal of Physical Chemistry* B, 2003, Vol. 107, Issue 4, p. 895

[43] SAKAI, N., WANG, R., FUJISHIMA, A., WATANABE, T., HASHIMOTO, K. Effect of Ultrasonic Treatment on Highly Hydrophilic TiO_2 Surfaces. *Langmuir*, 1998, Vol. 14, p. 5918.

[44] KAMEI, M., MITSUHASHI, T. Hydrophobic drawings on hydrophilic surfaces of single crystalline titanium dioxide: surface wettability control by mechanochemical treatment. *Surface Science*, 2000, Vol. 463, Issue 1, p. L609

[45] WHITE, J. M., SZANYI, J., HENDERSON, M. A. The Photon-Driven Hydrophilicity of Titania: A Model Study Using TiO_2 (110) and Adsorbed Trimethyl Acetate. *Journal of Physical Chemistry* B, 2003, Vol. 107, Issue 34, p. 9029

[46] WANG, C., HROENZIN, H., SHULTZ, M. J. Molecular Species on Nanoparticulate Anatase TiO_2 Film Detected by Sum Frequency Generation: Trace Hydrocarbons and Hydroxyl Groups, *Langmuir*, 2003, Vol. 19, p. 7330

[47]ZUBKOV, T., STAHL, D., THOMPSON, T. L., PANAYOTOV, D., DIWALD, O., YATES, J. T. Jr. Ultraviolet light-induced hydrophilicity effect on TiO_2(110)(1 x 1). Dominant role of the photooxidation of adsorbed hydrocarbons causing wetting by water droplets. *Journal of Physical Chemistry* B, 2005, Vol. 109, Issue 32, p. 15 454

[48] GJEROVI, M. *Phase Formation of Photoactive TiO_2 Thin Films by Metal Plasma Immersion Ion Implantation.* (online), cited 12. 5. 2016, available from: http://www.iom-leipzig.de/download/publikationen/59_P.pdf

[49] CARP, O., HUISMAN, C. L. Photoinduced reactivity of titanium dioxide, *Progress in Solid state Chemistry*, 2004, Vol. 32, Issue 1-2, p. 33

[50] HERRMANN, J. M. Heterogeneous photocatalysis: state of the art and present applications. *Topics in Catalysis*. 2005, Vol. 34, Issue 1-4, p. 49

[51] ZBOŘILOVÁ, Z. *Photocatalytical activity of hybrid layers of TiO2 and SiO2*. Brno, University of Technology, Faculty of Chemistry, 2013, (Diploma Thesis), Supervisor: Ing. Petr Dzik, Ph.D., 56 pages

[52] WANG, M. Y., LIU, W. S., XIU, Z., LIAO, B. X., CUI, P. X., PAN, J. Preparation and photocatalytic properties of silica gel-supported TiO_2. *Materials Letters*, 2006, Vol. 60, p. 974.

[53] CUNNINGHAM, J., AL-SAYYED, C. Factors influencing efficiencies of TiO2-sensitised photodegradation. Part 1 – Substituted benzoic acids: discrepancies with dark-adsorption parameters. *Journal of Chemical Society, Faraday Transactions,* 1990, Vol. 86, Issue 23, p. 3935

[54] Turchi, C. S.; Ollie, D. F. Photocatalytic degradation of organic water contaminants: Mechanisms involving hydroxyl radical attack. *Journal of Catalysis*, 1990, Vol. 122, Issue 1, p. 178

[55] KUMAR, M., KUMAR, M., KUMAR, D. The deposition of nanocrystalline TiO_2 thin film on silicon using Sol–Gel technique and its characterization, *Microelectronic Engineering,* 2010, vol. 87, Issue 3, p. 447

[56] SONAWANE, R. S., HEGDE, S. G., DONGARE, M. K. Preparation of titanium (IV) oxide thin film photocatalyst by sol-gel dip coating, *Materials Chemistry and Physics,* 2002, Vol. 77, p. 744–750.

[57] SHAN, A. Y., GHAZI, T. I. M., RASHID, S. A. Immobilisation of titanium dioxide onto supporting materials in heterogeneous photocatalysis: A review. *Applied Catalysis A: General*, 2010, Vol. 389, Issue 1-2, p. 1

[58] HUANG, W., LEI, M., HUANG, H., CHEN, J., CHEN, H. Effect of polyethylene glycol on hydrophilic TiO_2 films: Porosity-driven superhydrophilicity. *Surface and Coatings Technology*, 2010, Vol. 204, Issue 24, p. 3 954

[59] YOKO, T., HU, L., KOZUKA, H., SAKKA, S. Photoelectrochemical properties of TiO_2 coating films prepared using different solvents by the sol-gel method, *Thin Solid Films*, 1996, Vol. 283, Issue 1-2, p. 188

[60] YOLDAS, E. B. Formation of titania-silica glasses by low temperature chemical polymerization, *Journal of Non-Crystalline Solids,* 1980, Vol. 38-39, p. 81

[61] YOLDAS, E. B. Hydrolysis of titanium alkoxide and effects of hydrolytic polycondensation parameters*, Journal of Materials Science,* 1986, Vol. 21, p. 1087

[62] LIVAGE, J., HENRY, M., SANCHEZ, C. Sol-gel chemistry of transition metal oxides. *Progress in Solid State Chemistry*, 1988, Vol. 18, Issue 4, p. 259

[63] KEPERT D.L. *The early transition metals*, dissertation thesis, 1976, Academic Press Inc., London (1972)

[64] BRINKER, C. J., SCHERER, G. W., *Sol-gel science, The physics and Chemistry of sol-gel processing*, Academic Press Inc., London 1990, 908 pages, ISBN: 0121349705.

[65] BARRINGER, E. A., BOWEN, H. K. Formation, Packing, and Sintering of Monodisperse TiO2 Powders. *Journal of American Ceramic Society*, 1982, Vol. 65, Issue 12, p. C-199

[66] HENCH, Larry L. a Donald R. ULRICH. *Ultrastructure processing of ceramics, glasses, and composites.* New York: Wiley, c1984. ISBN: 0471896691

[67] SAKKA, S., KAMIYA, K.Glasses from metal alcoholates. *Journal of Non-Crystalline Solids*, 1980, Vol. 42, Issue 1–3, p. 403

[68] KAMIYA, K., TANIMOTO, K., YOKO, T. Preparation of TiO2 fibres by hydrolysis and polycondensation of $Ti(O\text{-}i\text{-}C_3H_7)4$. *Journal of Materials Science* Letters, 1986, Vol. 5, Issue 4, p. 402

[69] LAMER, V. K., DINEGAR R. H., Theory, production and mechanism of formation of monodispersed hydrosols, *Journal of American Chemical Society,* 1950, Vol. 72, p. 4847

[70] RING, Terry A. *Fundamentals of ceramic powder processing and synthesis*. San Diego: Academic Press, c1996. ISBN: 0125889305.

[71] DIRKSEN, J. A., RING, T. A. Fundamentals of crystallization: Kinetic effects on particle size distributions and morphology, *Chemical Engineering Scienece,* 1991, Vol. 46, Issue 10, p. 2389

[72] ZETTLEMOYER, A. C. *(ed.). Nucleation*. New York: Marcel Dekker, Inc., 1969.

[73] SOLVOVIEV, A., JENSEN, H., SØGAARD, E. G., KANAEV, A. V. Aggregation kinetics of sol-gel process based on titanium tetraisopropoxide. *Journal of Materials Science,* 2003, Vol. 38, Issue 15, p. 3315

[74] HARRIS, M. T., BYERS, C. H. Effect of solvent on the homogeneous precipitation of titania by titanium ethoxide hydrolysis. *Non-Crystalline Solids,* 1988, Vol. 103, p.49

[75] BERLUNG, K. A., TALLANT D. R., DOSCH R. G. *Science of Ceramic Processing*, edited by D. R. Ulman and D. R. Ulrich. Wiley, New York, 1991 p. 95.

[76] HU, M. Z.-C., ZIELKE, J. T., BYERS, C. H., LIN, HARRIS, M. T. Probing the early-stage/rapid processes in hydrolysis and condensation of metal alkoxides. *Journal of Materials Science,* 2000, Vol. 35, Issue 8, p. 1957

[77] JULLIEN, R. The application of fractals to investigations of colloidal aggregation and random deposition. *New Journal of Chemistry,* 1990, Vol. 14, p. 239

[78] MALATO, S., P. FERNÁNDEZ-IBAÑEZ, P., MALDONNADO, M. I., BLANCO, J., GERNJAK, W. Decontamination and disinfection of water by solar photocatalysis: Recent overview and trends, *Catalysis today,* 2009, Vol. 147, p. 1

[79] CHEN, X., LI, C. W., WANG, J., LI, J., LUAN, X. Y., LI, Y., XU, R., WANG, B. X. Investigation on solar photocatalytic activity of TiO_2 loaded composite: TiO_2/Eggshell, TiO_2/Clamshell and TiO_2/$CaCO_3$. *Materials Letters,* 2010, Vol. 64, p. 1437

[80] HE, Z., HONG, T., CHEN, J., SONG, S. Preparation and characterization of nanocrystalline titania powders by sonochemical synthesis. *Separation and purification technology,* 2012, Vol. 96, p. 50

[81] HE, Z., HONG, T., CHEN, J., SONG, S. A magnetic TiO_2 photocatalyst doped with iodine for organic pollutant degradation. *Separation and Purification Technology*, 2012, Vol. 96, p. 50

[82] YE, M. M., ZHANG, Q., HU, Y. X., GE, J. P., LU, Z. D., HE, L., CHEN, Z. L., YIN, Y. D. Magnetically recoverable core–shell nanocomposites with enhanced photocatalytic activity, *Chemistry – A European Journal,* 2010, vol. 16, p. 62430

[83] LUO, M. L., BOWDEN, D., BRIMBLECOMBE, P. Preparation of black sand-based magnetic photocatalysts for photocatalytic oxidation of aqueous phenol. *Applied Catalysis B: Environmental,* 2009, Vol. 87, p. 1

[84] RANA, S., SRIVASTAVA, R. S., SORENSSON, M. M., MISRA, R. D. K. Synthesis and characterization of nanoparticles with magnetic core and photocatalytic shell: anatase TiO2–NiFe2O4 system. *Material Science Engineering B.* 2005, Vol. 119, p. 144

[85] ZHANG, K., AMPONSAH, O., ARSLAN, M., HOLLOWAY, T., SINCLAIR, D. at all. Magnetic nanocomposite spinel and FeCo core–shell and mesoporous systems. *Journal of Magnetism and Magnetic Materials,* 2012, Vol. 324. p. 1938

[86] KULKARNI, S. A. Synthesis and Characterization of Fe_3O_4 Nanoparticles for Engineering Applications, ICBEST 2012 Proceedings by International Journal of Computer Applications, (online), cited. 21. 6. 2016, available at: http://research.ijcaonline.org/icbest/number2/icbest1027.pdf

[87] ZHANG, H., ZHU, G. Q. One-step hydrothermal synthesis of magnetic Fe_3O_4 nanoparticles immobilized on polyamide fabric. *Applied Surface Science,* 2012, Vol. 258, p. 4952

[88] WU, W., JIANG, C., ROY, V. A. L. Recent Progress in Magnetic Iron Oxide Semiconductor Composite Nanomaterials as Promising Photocatalysts. *Nanoscale*, 2014, Vol. 7, p. 38

[89] MOHAPATRA, M., ANAND, S. Synthesis and applications of nano-structured iron oxides/hydroxide – a review. *International Journal of Engineering, Science and Technology,* 2010, Vol. 2, No. 8, p. 127

[90] G. ZOU, G., XIONG, JIANG, C., LI, H., LI, T., DU, J., QIAN, Y. Fe_3O_4 Nanocrystals with Novel Fractal. *Journal of Physical Chemistry, B,* 2005, Vol. 109, p. 18 356

[91] GNANAPRAKASH, G., MAHADEVAN, S., JAYAKUMAR, T., KALYANASUNDARAM, P., PHILIP, J., BALDEV, R. Effect of initial pH and temeprature of iron salt solutions on formation of magnetite nanoparticles. *Materials chemistry and Physics*, 2007, Vol. 103, p. 168

[92] CORNELL, R. M., SCHWERTMANN, Udo. *The iron oxides: Structure, properties, reactions, occurrences, and uses*, New York 2003, Wiley, ISBN: 3-527-30274-3

[93] CASILLAS, P. E. G., GONZALES, C. A. R., PÉREZ, C. A. M. *Infrared Spectroscopy of Functionalized Magnetic Nanoparticles, Infrared Spectroscopy - Materials Science, Engineering and Technology*, Prof. Theophanides Theophile (Ed.), 2012, ISBN: 978-953-51-0537-4, InTech (online), cited 24. 5. 2016, available from: http://www.intechopen.com/books/infrared-spectroscopy-materials-science-engineering-andtechnology/infrared-spectroscopy-of-functionalized-magnetic-nanoparticles

[94] TEJA, A. S., KOH, P.-Y. Synthesis, properties, and applications of magnetic iron oxide nanoparticles. *Progress in Crystal Growth and Characterization of Materials*, 2009, Vol. 55, p. 22

[95] BELESSI, V., LAMBROPOULOU, D., KONSTANTINOU, I., ZBORIL, R., TUCEK, J. at all. Structure and photocatalytic performance of magnetically separable titania photocatalysts for the degradation of propachlor, *Applied Catalysis B: Environmental,* 2009, Vol. 87, Issue 3-4, p. 181

[96] D. BEYDOUN, D., AMAL, R., LOW, G., MCEVOY, S. Silver metallisation of titania particles: effects on photoactivity for the oxidation of organics, *Catalysis Today,* 2011 Vol. 175, Issue 1, p. 293

[97] LIU, H., JIA, Z., JI, S., ZHENG, Y., LI, M., YANG, H., Preparation and characterization of magnetically separable photocatalyst ($TiO_2/SiO_2/Fe_3O_4$): Effect of carbon coating and calcination temperature, *Catalysis Today,* 2011, Vol. 175, Issue 1 p. 293

[98] ANDERSON, C., BARD, A. J. An Improved Photocatalyst of TiO_2/SiO_2 Prepared by a Sol-Gel Synthesis. *Journal of Physical Chemistry,* 1995, Vol. 99, p. 9882

[99] YU, X., LIU, S., YU, J. Superparamagnetic γ-Fe_2O_3@SiO_2@TiO_2 composite microspheres with superior photocatalytic properties, *Applied Catalysis B: Environmental*, 2011, Vol. 104, Issues 1–2, p. 12

[100] XU, J., AO, Y., FU, D., YUAN, C. Low-temperature preparation of anatase titania-coated magnetite, *Journal of Physics and Chemistry of Solids*, 2008, Vol. 69, Issue 8, p. 1980

[101] WANG, Z., GUO, H., YU, Y., HE, N. Synthesis and characterization of a novel magnetic carrier with its composition of Fe_3O_4/carbon using hydrothermal reaction. *Journal of Magnetism and Magnetic Materials*, 2006, Vol. 302, no. 2, p. 397

[102] HASANPOUR, A., NIYAIFAR, M., MOHAMMADPOUR, H., AMIGHIAN, J. A novel non-thermal proces of TiO_2-shell coating on Fe_3O_4-core nanoparticles, *Journal of Physics and Chemistry of Solids,* 2012, Vol. 73, p. 1066

[103] SHI, F., LI, Y., ZHANG, Q., WANG, H. Synthesis of $Fe_3O_4/C/TiO_2$ magnetic photocatalyst via vapor phase hydrolysis. *International Journal of Photoenergy*, 2011. Article ID 365401, 8 pages, http://doi.org/10.1155/2012/365401

[104] TAREK, A., ALLAH, G., FUJIMURA, K., KATO, S., SATOKAWA, S., KOJIMA, T. Preparation and characterization of magnetically separable photocatalyst ($TiO_2/SiO_2/Fe_3O_4$): Effect of carbon coating and calcination temperature, *Journal of Hazardous Materials*, 2008, Vol. 154, p. 572

[105] HARIFI, T., MONTAZER, M. A novel magnetic reusable nanocomposite with enhanced photocatalytic activities for dye degradation. *Separation and Purification Technology*, 2014, Vol. 134, p. 210

[106] MATTHEWS, R. W., MCEVOY, S. R. Photocatalytic degradation of phenol in the presence of near-UV illuminated titanium dioxide. *Journal of Photochemistry and Photobiology, A: Chemistry,* 1992, Vol. 64, p. 231

[107] HARADA, K., HISANNGA, T., TANAKA, K. Photocatalytic degradation of organophosphorus conpounds in semiconductor suspension, *New Journal of Chemistry,* 1987, Vol. 11, p. 597

[108] JING, J., LI, J., FENG, J., LI, W., YU, W. W. Photodegradation of quinoline in water over magnetically separable Fe_3O_4/TiO_2 composite photocatalysts. *Chemical Engineering Journal*, 2013, Vol. 219, p. 355

[109] BEYDOUN, D., AMAL, R., LOW, G., MCEVOY, S. Silver metallisation of titania particles: effects on photoactivity for the oxidation of organics. *Catalysis Today,* Vol. 175, Issue 1, p. 293

[110] SABIN, F., TÜRK, T., VOGLER, A. Photo-oxidation of organic compound in the presence of titanium dioxide: determination of the efficiency. *Journal of Photochemistry and Photobiology A: Chemistry,* 1992, Vol. 63, no. 1, p. 99

[111] BELLESI, V., LAMBROPOULOU, D., KONSTANTINOU, I., ZBORIL, R., TUCEK, J. at all. Structure and photocatalytic performance of magnetically separable titania

photocatalysts for the degradation of propachlor, *Applied Catalysis B: Environmental,* 2009, Vol. 87, Issue 3-4, p. 181

[112] ZUO, R., DU, G., ZHANG, W., LIU, L., LIU, Y., MEI, L., LI, Z. Photocatalytic Degradation of Methylene Blue Using TiO_2 Impregnated Diatomite, *Advances in Materials Science and Engineering*, 2014, Article ID 170148, 7 pages

[113] HOUAS, A. Photocatalytic degradation pathway of methylene blue in water. *Applied Catalysis B: Environmental,* 2001, Vol. 31, Issue 2, p. 145

[114] LICHTIN, N. N., AVUDAITHAI, M., BERMAN, E. Photocatalytic Oxidative Degradation of Vapors of Some Organic Compounds Over TiO_2. *Research on Chemical Intermediates*, 1994, Vol. 20, Issue 7, p. 755

[115] SAUER, M. L., OLLIS, D. F. Photocatalyzed Oxidation of Ethanol and Acetaldehyde in Humidified Air*. Journal of Catalysis*, 1996, Vol. 158, Issue 2, p. 570

[116] J. ARAÑA, J., DOÑA-RODRÍGUEZ, J. M., GARRIGA I CABO, C., GONZÁLEZ-DÍAZ, O., J.A. HERRERA-MELIÁN, J. A. PÉREZ-PEÑA, J. FTIR study of gas-phase alcohols photocatalytic degradation with TiO_2 and AC-TiO_2. *Applied Catalysis B: Environmental,* 2004, Vol. 53, Issue 4, p. 221

[117] HE, B. B., PRECKWINKEL, U., SMITH, K. L. Fundamentals of Two-Dimensional X-Ray Diffraction (XRD2). Advances in X-ray Analysis, 2000, Vol. 43, p. 273

[118] SCHERRER, P. Bestimmung der Grösse und der Inneren Struktur Kolloidteilchen Mittels Nachrichten von der Gesellschaft der Wissenschaften, Göttingen, *Mathematisch-Physikalische*, 1918, Vol. 2, p. 98

[119] MISRA, Prabhakar a Mark A. DUBINSKII. *Ultraviolet spectroscopy and UV lasers*. New York: Marcel Dekker, c2002. Practical spectroscopy, v. 30. ISBN 0824706684.

[120] Wikimedia Commons. Schematics of UV – visible spectrophotometer, (online), [cited. 18. 6. 2016], available from: https://upload.wikimedia.org/wikipedia/commons/9/95/Schematic_of_UV-_visible_spectrophotometer.png

[121] HARVEY, D. Instrumentation for Turbidimetry and Nephelometry. (online), 2013, Cited [16. 6. 2016], Available from: http://community.asdlib.org/imageandvideoexchangeforum/2013/07/30/instrumentation-for-turbidimetry-and-nephelometry/

[122] SADAR, M. NV Turbidity instrumentation – an overview of today´s available technology. Turbidity and Other Sediment Surrogates Workshop, April 30 – May 2, 2002, Reno, (online), [cited 16. 6. 2016], available from: http://water.usgs.gov/osw/techniques/TSS/sadar.pdf

[123] SWAPP, S. Scanning electron microscopy, Geochemical instrumentation and analysis, (online), [cited 16. 6. 2016], available from: http://serc.carleton.edu/research_education/geochemsheets/techniques/SEM.html

[124] User ARTE, Schema MEB Schemitics of UV – visible spectrophotometer, Wikimedia Crative Commons. (online), [cited 18. 6. 2016], available from: https://upload.wikimedia.org/wikipedia/commons/0/0d/Schema_MEB_%28en%29.svg

[125] TSCHARNUTER, W. *Photon Correlation Spectroscopy in Particle Sizing*. in Encyclopedia of Analytical Chemistry R.A. Meyers (Ed.) John Wiley & Sons Ltd, Chichester, 2000, p. 5469

[126] BERNE, B. J., PECORA, R. *Dynamic Light Scattering*. Courier Dover Publications, 2000, ISBN: 0486411559

[127] SCHAETZEL, K. Suppression of multiple-scattering by photon cross-correlation technique, *Journal of modern optics,* 1991, Vol. 38, p. 1849

[128] Sympatec. Photon cross-correlation spectrometry, (online), [cited 30. 6. 2016] available from: https://www.sympatec.com/EN/PCCS/PCCS.html, Scheme published with written permission of Sympatec Group.

[129] COATS, A. W., REDFERN, J. P. Thermogravimetric analysis. A review. *Analyst*, 1963, Vol. 88, p. 906

[130] BHADESHIA H.K.D.H. Thermal analyses techniques. Differential thermal analysis. University of Cambridge, Material Science and Metallurgy. (online), [cited 20. 6. 2016], available from: www.msm.cam.ac.uk/phase-trans/2002/Thermal1.pdf

[131] STUART, B. H. *Infrared Spectroscopy: Fundamentals and Applications*. Wiley, New York, 2004, 244 pages, ISBN: 9780470854280.

[132] User DANH, IR_spectroscopy_apparatus. Wikimedia Crative Commons. (online), [cited 18. 6. 2016] Available from: https://en.wikipedia.org/wiki/Infrared_spectroscopy#/media/File:IR_spectroscopy_apparatus.svg

[133] BRUNAUER, S., Emmett, P. H., TELLER, E. Adsorption of Gases in Multimolecular Layers. *Journal of the American Chemical Society*, 1938, Vol. 60, Issue 2, p. 309

[134] HWANG, N., ANDREW, R. BET Surface Area Analysis of Nanoparticles. OpenStax CNX. (online), [cited 18. 6. 2016], available from: http://cnx.org/contents/f5c058e0-41f2-4ef6-878b-2fdc07760129@1

[135] DODRILL, B. C. Magnetic Media Measurements with a VSM. Microsystems Technology Laboratories, Massachusetts institute of technology, (online), [cited 18. 6. 2016], Available from: http://www-mtl.mit.edu/labnetwork/archive/att-0651/02-magnetic_media_application_note.pdf

[136] GRAHAM, C. D. High sensitivity magnetization measurement. *Journal of Science and Technology,* 2000, Vol. 16, p. 100

[137] DOWN, Randy D. a Jay H. LEHR. *Environmental instrumentation and analysis handbook*. Hoboken, N.J.: Wiley-Interscience, c2005. ISBN: 047146354X.

[138] HÜFNER, Stefan. *Photoelectron spectroscopy: principles and applications*. 2nd ed. Berlin: Springer-Verlag, c1996. Springer series in solid-state sciences. ISBN: 3540608753

[139] ŠUTKA, A., LAGZDINA, S., JUHNEVICA, I., JAKOVLEVS, D., MAIOROV, M. Precipitation synthesis of magnetite Fe_3O_4 nanoflakes. *Ceramics International*, 2014, Vol. 40, p. 11437

[140] FERRARI, L., KAUFMANN, J., WINNEFELD, F., PLANK, J. Multi-method approach to study influence of superplasticizers on cement suspensions. *Cement and Concrete Research*, 2011, Vol. 41, p. 1058

[141] ZINGG, A., WINNEFELD, F., HOLZER, L., PAKUSCH, J., BECKER, S., GAUCKLER, L. Adsorption of polyelectrolytes and its influence on the rheology, zeta potential, and microstructure of various cement and hydrate phases. *Journal of Colloid and Interface Science*, 2008, Vol. 323, p. 301

[142] SOLNÝ, T.; PTÁČEK, P.; MÁSILKO, J. Preparation of magnetic nano- sized iron oxide particles. CEITEC PhD Retreat: Book of Abstracts: 23–24 April 2015, Valtice, Czech Republic. 1. Brno: Masaryk University, 2015. p. 118.

[143] JOLIVET, J., CHANÉAC, C., TRONC, E. (2004). Iron oxide chemistry. From molecular clusters to extended solid networks, *Chemical Communications,* 2004, Issue 5, p. 481.

[144] SOLNÝ, T.; BARTONÍČKOVÁ, E.; PTÁČEK, P. Preparation and TiO_2 Coating of nanosized magnetic particles. In Nanocon 2015 Conference Proceedings. 1st Edition 2015. Brno: Tangel Ltd, 2015, p. 282.

[145] KUBELKA, P., MUNK, F. Ein Beitrag zur Optik der Farbanstriche. *Zeit. Für Tekn. Physik*, 1931, Vol. 12, p. 593

[146] CASBEER, E., SHARMA, V. K., LI, X. Z. Synthesis and photocatalytic activity of ferrites under visible light: A review. Separation and Purification Technology, 2012, Vol. 87, p. 1

[147] SOLNÝ, T., PTÁČEK, P., MÁSILKO, J., TKACZ, J., BARTONÍČKOVÁ, E., DAVIDSDÓTTIR, S., AMBAT, R. TiO_2 surface coating of Mn- Zn dopped ferrites study. *Materials Science Forum*, 2016, Vol. 851, p. 153

[148] DAVÍÐSDÓTTIR, Svava. *Investigation of photocatalytic activity of titanium dioxide deposited on metallic substrates prepared by PVD*, (Doctoral Thesis), Department of Mechanical Engineering, Technical University of Denmark (DTU), Supervisor of thesis: Prof. Rajan Ambat, 2014

[149] DIN 5298: *Photocatalytic activity of surfaces - Determination of photocatalytic activity by degradation of methylene blue*. German technical standard, published on 1.10.2008,

[150] PTÁČEK, P.; SOLNÝ, T.; OPRAVIL, T.; ŠOUKAL, F.; YADAV, R.; HAVLICA, J.: Ferrite reor. (Patent claim type) Faculty of Chemistry, Brno University of Technology, 2015

[151] CIHLÁŘ, J., CIHLÁŘ, J., BARTONÍČKOVÁ, E. Low-temperature sol-gel synthesis of anatase nanoparticles modified by Au, Pd and Pt and activity of TiO_2/Au, Pd, Pt photocatalysts in water splitting. *Journal of Sol-Gel Science and Technology*, 2013, Vol. 65, p. 430

[152] WANG, M., HE, T., PAN, Y., LIAO, W., ZHANG, S., DU, W. Water concentration controlled hydrolysis and crystallization in n-octanol to TiO_2 nanocrystals with size below 10 nm. Materials Chemistry and Physics, 2011, Vol. 130, p. 1294

8 LIST OF ABBREVIATIONS

Eg – Band gap energy

k – Boltzman constant

BET – Brunauer – Emmet Teller analysis

CAS – Chemical Abstract Services identifier

CVD – Chemical vapor deposition

C_b – Conduction band

CA – Contact angle

H_c – Coercivity

CFSE – Crystal Field Stabilization Energy

DTA – Differential Thermal Analysis

DLA – Diffusion limited aggregation processes

DLS – Direct light scattering

Emu – Electromagnetic units

eV – Electron volt

ESCA – Electron Spectroscopy for Chemical Analysis

EGA – Evolved Gas Analysis

FTIR – Fourier Transformed Infrared Spectroscopy

t_i – Induction time

M_r – magnetization remanence

MB – Methylene blue

R – Molar ratio of water/ Ti-alkoxide

NHE – Normal hydrogen electrode

Oe – Oersted

δ – Partial Charge

e^-_{cb} – Photogenerated electron

h_{vb}^+ – Photogenerated electrone hole

PCCS – Photon Cross Correlation Spectroscopy

hv – Photon Energy

PCE – Polycarboxylic ether superplasticizer

PVA – Polyvinyl alcohol

RLA – Rate limited aggregation processes

n_D – Refractive index

M_s – saturation magnetization

SEM – Scanning electron Microscopy

K – Scherrer´s constant

SAXS – Small angle X-ray scattering

TIPP – Titanium isopropoxide

TIETH – Titanium tetraethoxide

TIBUT – Titanium tetrabutoxide

TGA – Thermo Gravimetric Analysis

TDS – Total Dissolved Solids

M – Transition metal

V_b – Valence band

VPH – Vapor phase hydrolysis

VSM – Vibrating Sample Magnetometer

η – Viscosity

VOCs – Volatile Organic Compounds

XRD – X-Ray diffraction

XPS – X-Ray Photon Spectroscopy

9 ATTACHEMENTS

SEM analysis of unknown magnetic nanoparticles phase.

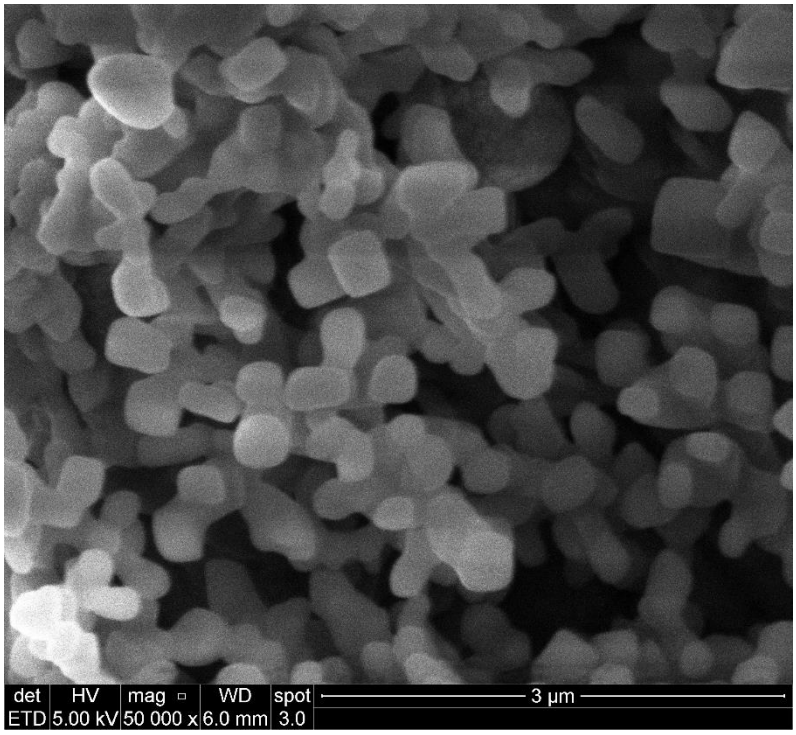

Sample 3. NaOH + ACE 40 (picture taken as soon as possible)

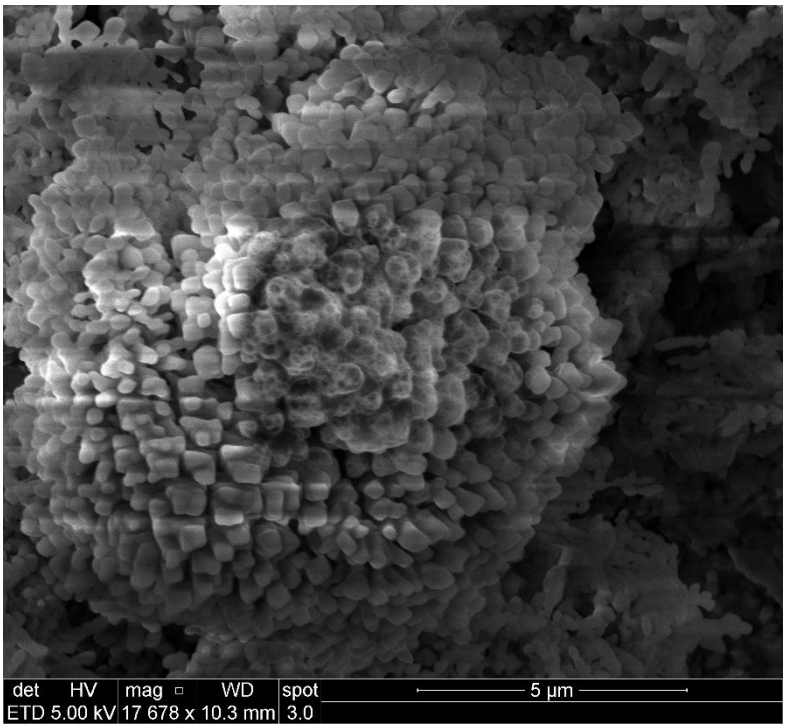

Sample 3. NaOH + ACE 40 (after 10 minutes of irradiation of surface with 5 kV X-Ray)

XPS spectra of core-shell analysed samples

NaOH + EXP TIO_2 + TIPP

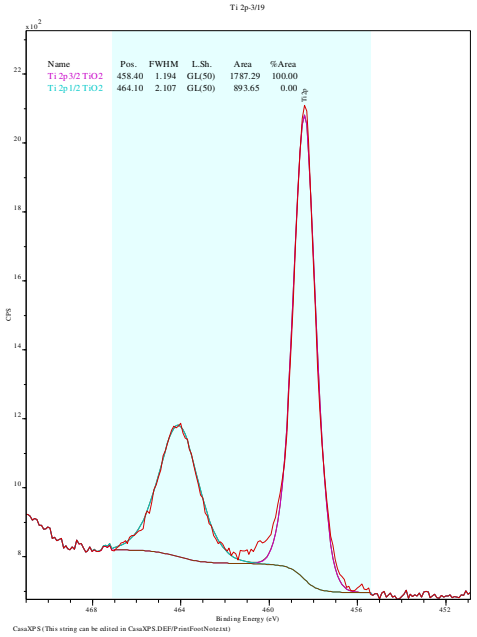

Ti XPS spectra

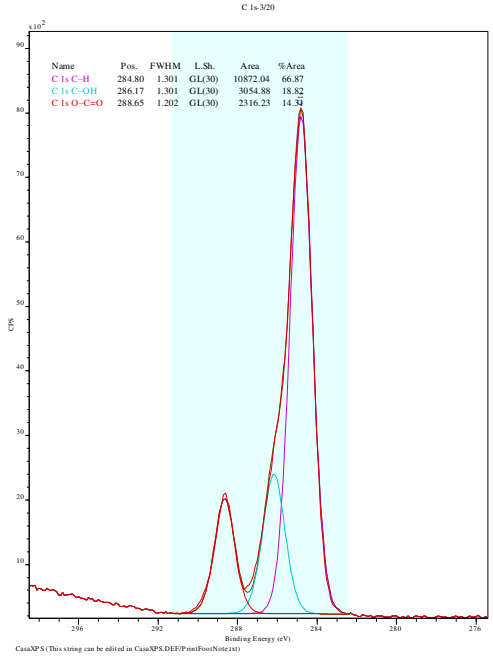

C XPS Spectra

NaOH TI+ ACE 40 + EXP TIO_2 + TIPP

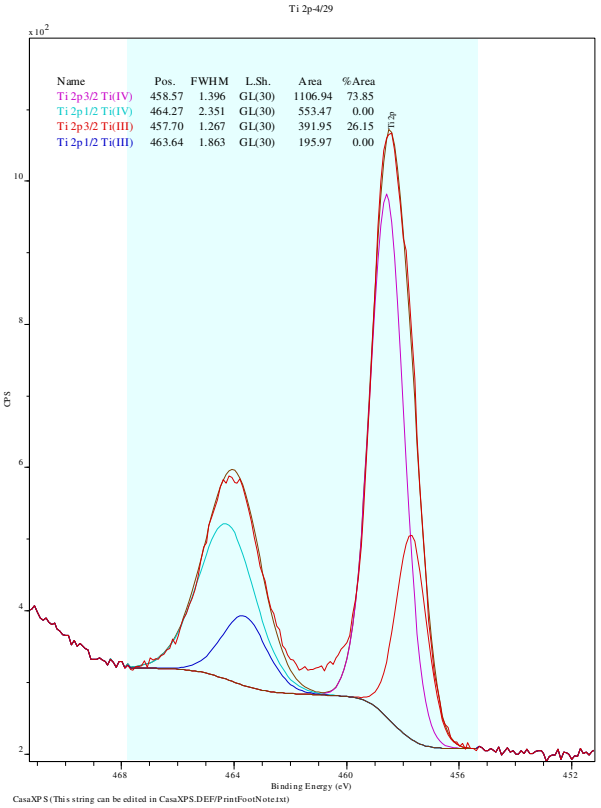

Ti XPS spectra

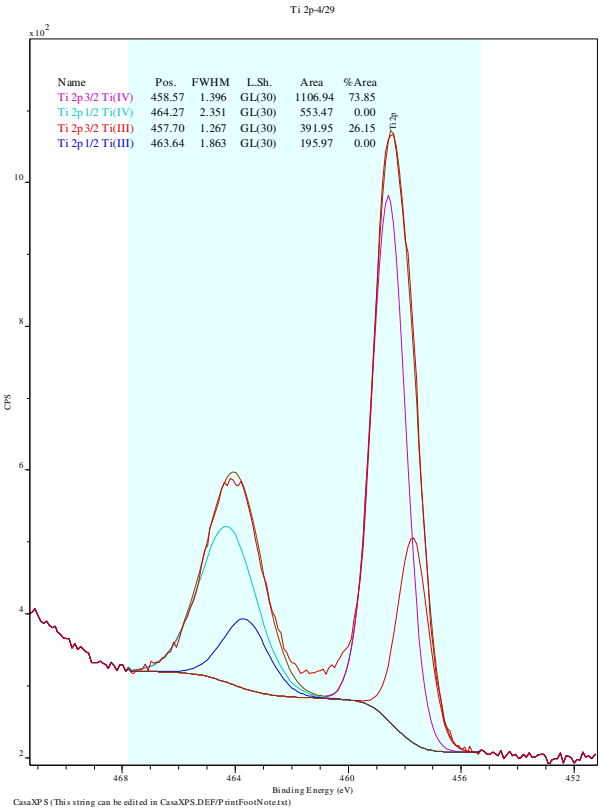

C XPS spectra

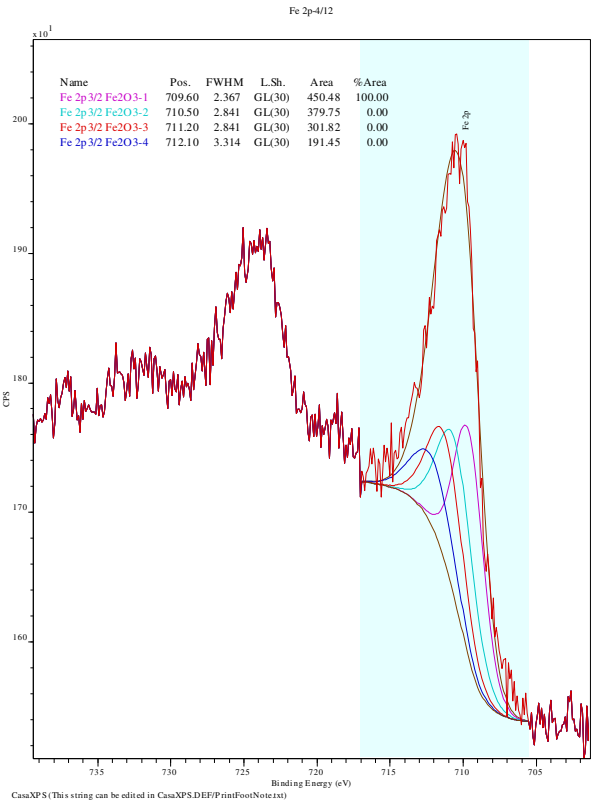

Fe XPS spectra